

DISSERTATION

A METHOD TO COMBINE SPACEBORNE RADAR AND RADIOMETRIC OBSERVATIONS OF
PRECIPITATION

Submitted by

Stephen Joseph Munchak

Department of Atmospheric Science

In partial fulfillment of the requirements

For the Degree of Doctor of Philosophy

Colorado State University

Fort Collins, Colorado

Fall 2010

Doctoral Committee:

Department Head: Richard H. Johnson

Advisor: Christian D. Kummerow

V. Chandrasekhar

Steven A. Rutledge

Graeme L. Stephens

ABSTRACT

A METHOD TO COMBINE SPACEBORNE RADAR AND RADIOMETRIC OBSERVATIONS OF PRECIPITATION

This dissertation describes the development and application of a combined radar-radiometer rainfall retrieval algorithm for the Tropical Rainfall Measuring Mission (TRMM) satellite. A retrieval framework based upon optimal estimation theory is proposed wherein three parameters describing the raindrop size distribution (DSD), ice particle size distribution (PSD), and cloud water path (cLWP) are retrieved for each radar profile. The retrieved rainfall rate is found to be strongly sensitive to the *a priori* constraints in DSD and cLWP; thus, these parameters are tuned to match polarimetric radar estimates of rainfall near Kwajalein, Republic of Marshall Islands. An independent validation against gauge-tuned radar rainfall estimates at Melbourne, FL shows agreement within 2% which exceeds previous algorithms' ability to match rainfall at these two sites.

The algorithm is then applied to two years of TRMM data over oceans to determine the sources of DSD variability. Three correlated sets of variables representing storm dynamics, background environment, and cloud microphysics are found to account for approximately 50% of the variability in the absolute and reflectivity-normalized median drop size. Structures of radar reflectivity are also identified and related to drop size, with these relationships being confirmed by ground-based polarimetric radar data from the North American Monsoon Experiment (NAME). Regional patterns of DSD and the sources of variability identified herein are also shown to be consistent with previous work documenting regional DSD properties. In particular, mid-latitude regions and tropical regions near land tend to have larger drops for a given reflectivity, whereas the smallest drops are found in the eastern Pacific Intertropical Convergence Zone. Due to properties of the DSD and rain water/cloud water partitioning that change with column water vapor, it is shown that increases in water vapor in a global warming scenario could lead to slight (1%) underestimates of a rainfall trends by radar but larger overestimates (5%) by

radiometer algorithms.

Further analyses are performed to compare tropical oceanic mean rainfall rates between the combined algorithm and other sources. The combined algorithm is 15% higher than the version 6 of the 2A25 radar-only algorithm and 6.6% higher than the Global Precipitation Climatology Project (GPCP) estimate for the same time-space domain. Despite being higher than these two sources, the combined total is not inconsistent with estimates of the other components of the energy budget given their uncertainties.

Stephen Joseph Munchak
Department of Atmospheric Science
Colorado State University
Fort Collins, Colorado 80523-1371
Fall 2010

ACKNOWLEDGEMENTS

The work described in this document was supported directly and indirectly by many people too numerous to list here, but what follows is an attempt to give credit to whom it is due.

First and foremost, I am extremely fortunate to have conducted this research under the advising of Professor Chris Kummerow. His abilities to be available without being overbearing, resourceful without encouraging dependence, and supportive of balance between graduate school and other aspects of life are cornerstones of good advising that all educators should strive for.

I also extend gratitude to the other members of my committee for their contributions and suggestions, particularly at the proposal review meeting. These persons include V. Chandrasekhar, Graeme Stephens, and Steven Rutledge.

In addition to my committee members several other Atmospheric Science and Engineering faculty have influenced this research, either through direct suggestions or relevant material or research methods learned in their classes. Some of these include Scott Denning, Bill Cotton, David Thompson, V. N. Bringi, Wayne Schubert, and Tom von der Haar.

The Kummerow research group has also been instrumental in this work. Wes Berg, Tristan L'Ecuyer, Matt Lebsock, Greg Elsaesser, Sarah Ringerud, Anita Rapp, Brian Griffith, Fang Wang, Janice Bytheway, Hiro Masunaga, Katie Boyd, Veljko Petkovic, and Becky Smith all provided useful insights, datasets, snippets (or larger portions) of code, and camaraderie at various stages of this research.

Specific contributions that come from outside the Kummerow group include the Kwajalein radar dataset (David Wolff - NASA/GSFC), disdrometer data from Kwajalein and Melbourne, FL (Ali Tokay - UMBC/JCET), the NAME radar dataset (Timothy Lang - CSU/ATS), and the vertical profiler data from Darwin, Australia (Christopher Williams - NOAA/CIRES). Other members of the NASA PMM DSD Working Group and GPM Combined Algorithm Team, including William Olson (UMBC/JCET), Mircea

Greco (NASA/GSFC), Ziad Haddad (CalTech/JPL) and Benjamin Johnson (UMBC/GEST) provided several ideas as well. Two anonymous reviewers for the portion of this dissertation submitted for publication as [Munchak and Kummerow \(2010\)](#) also provided thoughtful comments which were received in time to be included in this document.

Gratitude is extended to the group and department staff who have made any issues dealing with computer administration, travel planning, and the university in general a pleasant experience during my time as a student. These people include Becky Burke, Mark Ringerud, Matt Kassawara, Amariah Lebsock, Karrie Butler, Heather Packard, Jamie Schmidt, Jen Weingardt, and Shannon Irely.

The L^AT_EX template for this document was provided by Jonathan Vigh.

This work was supported by NASA Headquarters under and AMS Graduate Fellowship during the 2006-2007 academic year and under the NASA Earth and Space Science Fellowship Program from 2007-2010. Any opinions, findings, conclusions, or recommendations expressed in this document do not necessarily reflect the views of NASA.

Last but not least, my family and friends have been an inspiration to pursue this degree and provided emotional support throughout the process. I'd like to particularly thank my parents for encouraging and supporting an interest in science throughout my childhood and beyond. Finally, my wife Leigh has been a tremendous help in too many ways to list here, but I will state those that I believe to be most important. She has made the rest of my life easy during the final preparation of this document and, by virtue of knowing me even better than I know myself, has let me know exactly when I need to take a break before it became all-consuming.

DEDICATION

Non scholae, sed vitae discimus

We do not learn for the school, but for life

CONTENTS

1	Introduction	1
1.1	Opening Remarks and Motivation	1
1.2	Research questions and scope	5
1.3	Outline of dissertation	6
2	A Review of Radar, Radiometer, and Combined Satellite Rainfall Measurement Algorithms	8
2.1	Radar Algorithms	8
2.2	Radiometer Algorithms	15
2.3	Combined Algorithms	19
3	Algorithm Description	23
3.1	Optimal Estimation Theory	23
3.2	Radar Profiling Algorithm	25
3.3	Combined Retrieval Framework	31
3.4	Implementation	36
3.5	Sensitivity and Information Content	39
4	Algorithm Validation	45
4.1	Cloud and Drizzle In Non-Raining Pixels	45
4.2	Kwajalein	48
4.3	Melbourne, FL	51
4.4	Brightness Temperature Statistics	53
4.5	Disdrometer comparisons	55
5	Regional and Global Properties of the Raindrop Size Distribution Inferred from the Combined Algorithm	58
5.1	Introduction	58
5.2	Database Construction	62
5.3	Sources of DSD variability	64
5.4	Relationships between radar reflectivity structure and the rain DSD	72
5.5	Regional and Seasonal Distribution of DSD variability	78
6	Constraints on Global Rainfall and Energy Budgets	84
6.1	The Global Oceanic Tropical Rainfall Rate and Uncertainty	84
6.2	Detection of Trends in Global Mean Rainfall	87
7	Conclusions	91
7.1	Main Findings	91
7.2	Future Work	95
7.3	Concluding Remarks	96

Bibliography	97
Appendices	106
A Covariance Structure of the Rain DSD	107
A.1 Datasets	107
A.2 Analysis	110
B Residual Brightness Temperature Errors	113
B.1 Summary Statistics	113
B.2 Residual Error Maps	114
C A Bayesian Radar Profiling Algorithm	117
C.1 Algorithm	117
C.2 Results	119

FIGURES

1.1 Global population density and mean precipitation	2
2.1 Backscattering and Extinction Efficiency	10
2.2 Contribution of Different Drop Sizes to Rainfall and Reflectivity	11
2.3 Example Hitschfield-Bordan Retrieval	13
2.4 2A25 Flow Chart	14
2.5 Distribution of the SRT PIA	16
2.6 Rainrate-Brightness Temperature Relationships	18
2.7 GPROF Flow Chart	19
2.8 Combined Algorithm Flow Chart	21
3.1 Default profiles of snow/graupel and cloud water	28
3.2 Profiles of reflectivity and extinction in the melting layer	29
3.3 Rain CDFs for different DSD constraints	31
3.4 Flow chart of TRMM combined PR+TMI retrieval	32
3.5 Example of partially rain-filled TMI FOVs	33
3.6 Sample orbit segment	38
3.7 Composite reflectivity profiles used in sensitivity analysis.	39
3.8 Cost function for various constraint for each sample profile	40
3.9 Information content for each retrieved variable and rain type	43
3.10 Constraints on graupel fraction and IWP	44
4.1 Cloud LWP retrievals for a sample scene on 1 Jan 2000.	47
4.2 Cloud LWP retrieval statistics	49
4.3 Rain PDFs and CDFs for Kwajalein	50
4.4 Mean retrieved profiles of D_0 and Z at Kwajalein	51
4.5 An example case from Kwajalein	52
4.6 Monthly and yearly mean rain rates from different retrieval methods at Melbourne, FL	53
4.7 Brightness temperature scatter plots	54
4.8 Comparison of retrieved LWC and D_m to disdrometer measurements	56
5.1 Spatial distribution of profiles	62
5.2 Distribution of profiles and rainfall by information content	64
5.3 Spatial distribution of profiles by information content	65
5.4 Correlation of D_0 with the variables in Table 5.1	67
5.5 Same as Figure 5.5, except for ϵ_{DSD} instead of D_0	68
5.6 ϵ_{DSD} and D_0 versus freezing level and echo top height	69
5.7 Same as Figure 5.6 but for rain inhomogeneity and melt density.	70
5.8 Same as Figure 5.6 but for TPW and SST.	71
5.9 Same as Figure 5.6 but for TPW and column relative humidity.	72

5.10	Same as Figure 5.6 but for warm rain depth and ϵ_{ICE} .	73
5.11	Matrix of EOFs derived from the profile database.	74
5.12	Convective fraction of profiles by PC value.	75
5.13	Sample reflectivity EOFs	76
5.14	Correlation of ϵ_{DSD} , ϵ_{ICE} , and ϵ_{CLW} with reflectivity PC1 and PC2	77
5.15	Correlation of reflectivity PCs with D_0^* during the NAME field experiment.	78
5.16	One-degree gridded means of ϵ_{DSD} and D_0	79
5.17	Seasonal gridded means of ϵ_{DSD}	81
5.18	Maps of the mean values of the three leading PCs identified in section 5.3.	82
5.19	Maps of the reflectivity PCs identified in section 5.4.	83
6.1	Mean zonal rain rates	85
6.2	Various Rain Quantities as a function of TPW	88
6.3	Power law coefficients as a function of TPW	88
6.4	Algorithm biases as a function of rain rate	90
A.1	Sample event from Wallops Island	108
A.2	Sample event from Darwin	110
A.3	Covariance structure of D_0^*	111
A.4	Vertical Structure of D_0^* from Darwin	112
B.1	Brightness temperature error statistics	114
B.2	Brightness temperature error EOFs	115
B.3	Maps of brightness temperature errors	116
C.1	Gridded mean values of ϵ_{DSD} , ϵ_{ICE} , and ϵ_{CLW} from the hybrid Bayesian+PIA retrieval	120
C.2	Gridded mean rainrates from the hybrid Bayesian+PIA retrieval	121

TABLES

3.1	Summary of retrieval parameters.	30
3.2	Default PSD parameters by 2A23 rain type.	30
3.3	Observations and retrieval parameters (all at PR pixel scale) used in each OE module.	34
3.4	TRMM products used in the combined algorithm	37
3.5	Information content (bits) of various physical parameters in composite profiles.	42
4.1	Correlation and bias between microwave- and VIRS-based cloud LWP retrievals.	48
4.2	Brightness Temperature RMS error and bias.	55
5.1	List of profile database variables and sources.	66
6.1	Components of the atmospheric energy budget.	87
A.1	Rainfall events in Z-band polarimetric dataset from Wallops Island, VA.	109
A.2	Rainfall events analyzed by a 920-MHz profiler in Darwin, Australia during TWP-ICE.	109
C.1	Effect of database sampling on PR Bayesian retrieval	118

Chapter 1

INTRODUCTION

1.1 Opening Remarks and Motivation

At any given time, precipitation is falling upon approximately ten percent of the earth's surface (Berg et al., 2010). Despite this relatively low frequency, without rain and snow, all land would resemble the most arid deserts. Thus, it is no coincidence that throughout history, populations have flourished most readily in proximity to sufficient water resources, due to the simple fact that we, as humans, require water to drink and grow food. Floods and long-term droughts have both been credited to the decline of various civilizations (Weiss, 1982). Even today, with advanced irrigation technology, maps of population density and annual average rainfall indicate that both minimum and maximum thresholds of rainfall are conditions of habitability (Figure 1.1). With global populations continuing to increase, it is more important than ever to accurately measure precipitation globally and understand its variability in order to adequately manage this increasingly constrained resource (Endter-Wada et al., 2009).

Aside from these important direct societal impacts, precipitation plays an important active role in atmospheric processes ranging from the smallest scale of cloud droplet interactions to the global energy budget. The amount of rain that falls from any given cloud is a complicated function of several factors, including but not limited to environmental factors such as water vapor amount and temperature profiles, dynamical factors such as updraft speed and wind shear, and microphysical factors such as cloud condensation nuclei and ice nuclei concentrations. Nevertheless, averaged together across the globe all of these precipitating clouds must produce enough latent heat to exactly compensate for the heat

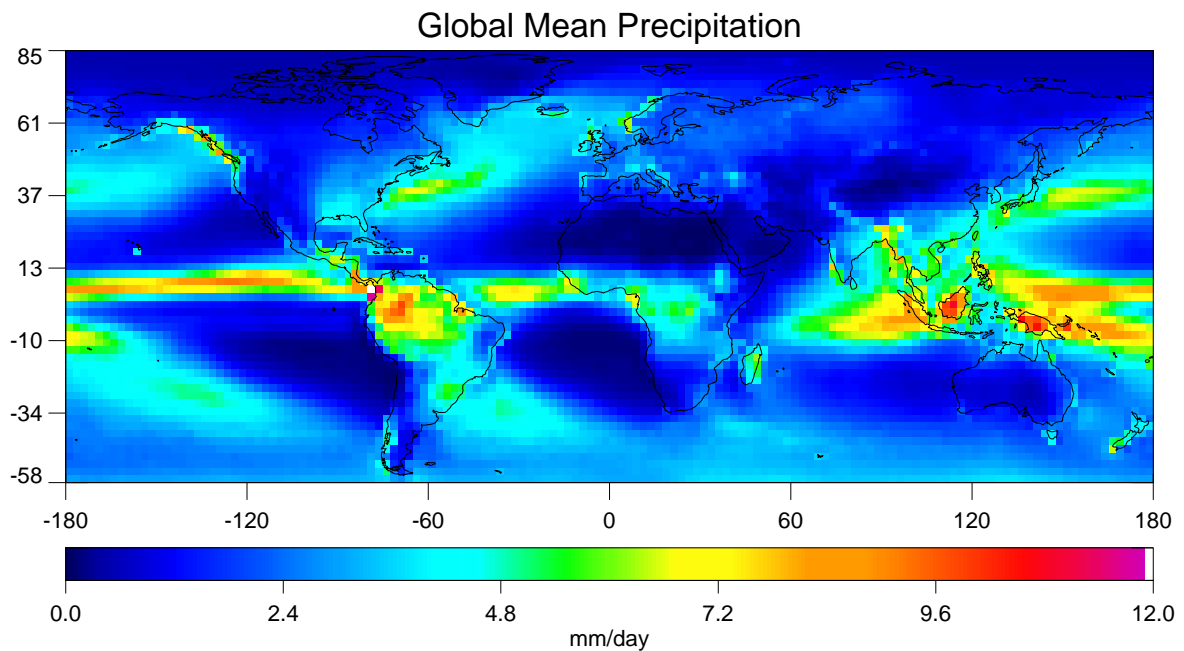
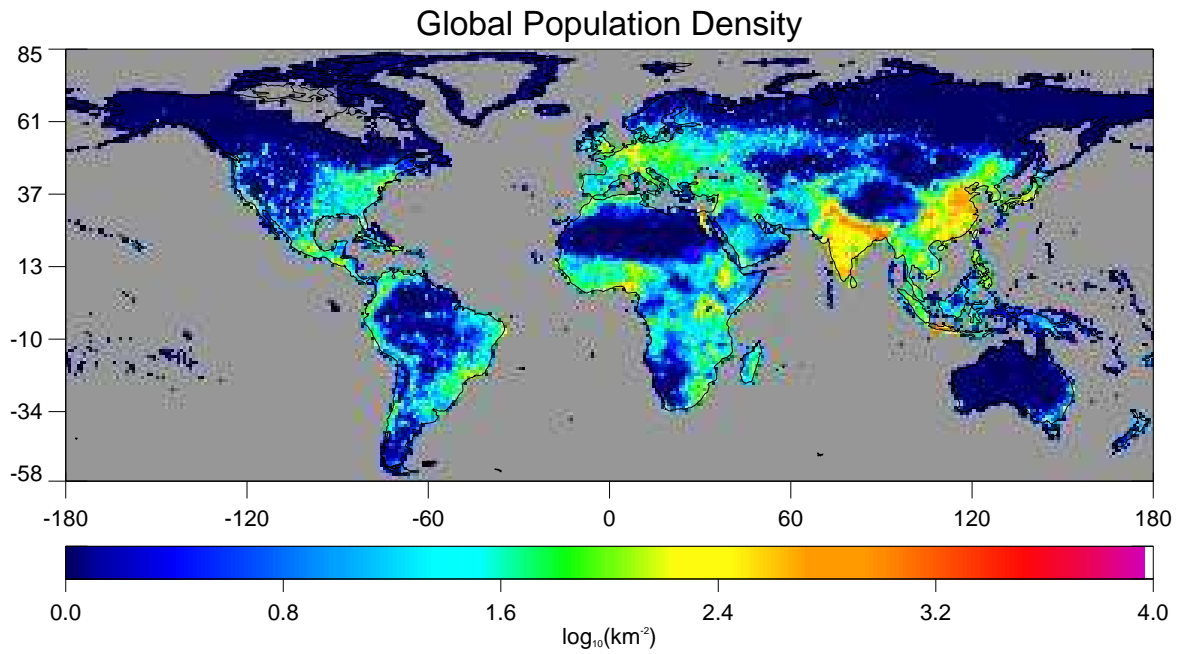


Figure 1.1: Top panel: Projected population density in 2010 (Center for International Earth Science Information Network (CIESIN), Columbia University; and Centro Internacional de Agricultura Tropical (CIAT), 2005). Bottom Panel: Global annual mean precipitation climatology from the Global Precipitation Climatology Project (GPCP; Huffman et al. (1997))

the atmosphere radiates to space, predominately in the clear subsidence regions that may be thousands of kilometers away! This connection between the global mean rainfall rate and the energy budget¹ also implies that the climate response of the global mean temperature and rain rate to increasing CO₂ concentrations are coupled (Allen and Ingram, 2002). Thus, the global mean rainfall rate and trend are an important climate metric for which accurate measurements are desirable.

Historically, measurements of rainfall have come from land-based gauges. Although these instruments are not without biases (*e.g.*, effects of wind (Yang et al., 1998)), assuming that good observational practices are followed, these represent the best estimates of precipitation reaching the ground at a point. However, the high spatial variability of rainfall, particularly in convective storms (Jameson et al., 1999), raises the probability that a point measurement may not be representative of the spatial average, which is more meaningful parameter for water resources and climate monitoring. Thus, since their inception meteorological radars have been used not only to detect storms but also to measure rainfall remotely (Marshall et al., 1947). Despite the considerable variability in the relationship between radar reflectivity and rainfall rate, ground-based radars have provided reasonable first-order estimates of rainfall but are limited to approximately 200km radius due to beam geometry and the curvature of the earth. Thus, over much of the earth's oceans, mountainous regions, and countries without radar networks, satellites provide the only platform from which precipitation estimates are possible.

The earliest satellite-based precipitation estimates came from infrared (IR) techniques (*e.g.*, (Barret, 1970)); however, the relationship between IR brightness temperatures (T_b) and surface rainfall is rather tenuous. More reliable satellite precipitation estimates were achieved in 1987 with the launch of the Special Sensor Microwave/Imager (SSM/I) on the polar-orbiting Defense Meteorological Satellite Program F8 (Hollinger et al., 1990). At lower microwave frequencies (*e.g.*, 19 GHz), the emission from precipitating clouds over oceans appears radiometrically warm compared to the background. This “warmth” is strongly related to the column-integrated liquid water. At higher microwave frequencies (*e.g.*, 85 GHz), the emission signal saturates at smaller amounts of liquid water, but increasingly effective scattering by precipitation-size ice crystals creates a T_b depression. Both of these signatures are physically related to the hydrometeor profile, but contain limited information. Algorithms that seek to

¹ specifically, the outgoing longwave radiation

retrieve the surface rain rate from microwave observations often rely on Bayesian matching schemes that involve a database of cloud and precipitation profiles (Kummerow and Giglio (1994), Kummerow et al. (2001)).

Another major milestone was reached in 1997 with the launch of the Tropical Rainfall Measuring Mission (TRMM). In addition to a microwave radiometer (TMI), the platform included the first space-borne precipitation radar (PR). In addition to its higher spatial resolution, the PR measures the vertical profile of precipitation. Both instruments have shortcomings, which can be attributed to their sensitivity to different geophysical parameters related to rainfall as well as assumptions inherent in the algorithms used to retrieve rainfall from T_b or reflectivity measurements. A global comparison of PR and TMI rainfall retrievals reveals distinct regional biases (Berg et al., 2006). It has been suggested that these may be a result of differences between the instruments' threshold sensitivity to shallow and/or light rainfall (Shimizu et al., 2009), errors in assumptions about the raindrop size distribution (DSD) in the radar algorithm (Iguchi et al. (2009), Kozi et al. (2009)), or systematic biases in the database that is the foundation for radiometer-based retrievals (Seo et al., 2007).

Notwithstanding these inconsistencies, the TRMM data have provided unique insight into the tropical hydrologic cycle and its response to short-term variability such as the El Niño Southern Oscillation (ENSO) and the Madden-Julian Oscillation (MJO) (*e.g.*, L'Ecuyer and Stephens (2007), Chen et al. (2007), Masunaga et al. (2006), Morita et al. (2006), Cho et al. (2004)). However, longer-term trends are more difficult to discern, in part due to these discrepancies between retrievals. One of the most pressing questions surrounding climate change is the rate at which precipitation scales with water vapor in the atmosphere. Held and Soden (2006) reviewed the projections from the suite of climate models included in the Fourth Assessment Report of the Intergovernmental Panel on Climate Change, and noted that, while water vapor scales at a rate near $7\% \text{ K}^{-1}$, precipitation scales at a reduced rate near $2\% \text{ K}^{-1}$. This predicted scaling is consistent with the energy budget analyses of Allen and Ingram (2002). However, Wentz et al. (2007) observe that in the 20-year record of precipitation derived from SSM/I instruments, which closely resembles the TMI record during coincident time/space subsets owing to their similar physical basis and algorithm, precipitation and evaporation scale at the same rate as water vapor. Interestingly, Berg et al. (2006) found that the ratio of TMI to PR rain rate was greatest in regions with high

values ($> 3 \text{ g cm}^{-2}$) of column-integrated water vapor, and suggested that these differences may be due to incorrect assumptions about cloud properties in higher vapor environments. If there is a true positive bias in radiometer-only precipitation in high water vapor regimes, then the observed precipitation-water vapor scaling relationship may be reduced in radiometer-only products. This underscores the importance of resolving the differences between radar and radiometer estimates of precipitation, and in particular understanding the relation between the environmental water vapor and cloud properties. To address these issues, a retrieval framework that incorporates both PR and TMI measurements to retrieve a set of consistent geophysical parameters has been developed and is the primary subject of this dissertation.

Aside from examining the TRMM record, development of a combined radar+radiometer algorithm is also of practical value to numerous existing and future spaceborne radiometers, such as the various SSM/Is, the Advanced Microwave Scanning Radiometer for the Earth Observing System (AMSR-E) (Kawanishi et al., 2003), and MADRAS to be launched as part of the Megha-Tropiques mission (Aguttes et al., 2000) in 2011, for example. The Bayesian rainfall algorithms used to retrieve rainfall from radiometers are currently moving away from databases of cloud-resolving models and towards profiles observed by the TRMM PR with adjustments to be consistent with TMI (Kummerow et al., 2010), such as those produced by the algorithm described in this dissertation. This architecture is the basis of the upcoming Global Precipitation Measurement (GPM) mission (Hou et al., 2010), which will carry a dual-frequency radar to further enhance the combined radar-radiometer retrieval on the core satellite for use as a database for retrievals on the various constellation radiometers.

1.2 Research questions and scope

In formulating this research a number of questions were posed, some initially, along with others that presented themselves as the research progressed. The purpose of the following list is to identify the areas of knowledge that the research described in this dissertation has sought to improve.

- What techniques are required to combine radar reflectivity profiles and multi-resolution, overlapping passive microwave radiometric measurements in an internally consistent geophysical product?

- Can a combined algorithm compare favorably to single-instrument algorithms, in terms of bias, compared to well-calibrated ground-validation (GV) products?
- What causes the observed regional bias patterns between the TRMM radar and radiometer algorithms (and GV)? Could these biases potentially mask or exaggerate long-term trends in global precipitation?
- Can the combined algorithm reliably measure two independent parameters of the raindrop size distribution (DSD)? If so, are these parameters related to properties of the clouds and/or the environment?
- What is the mean rainfall rate over the tropics and its uncertainty? Is this consistent with estimates derived from the measurements of the other components of the energy budget?

1.3 Outline of dissertation

This dissertation is divided into several chapters as follows: Chapter 2 provides a comprehensive review of the mechanics and assumptions underlying rainfall retrieval algorithms that have been developed for spaceborne radar and radiometers, including combined techniques. Chapter 3 describes the algorithm developed for this work, including sensitivity and information content analyses. Chapter 4 provides some comparisons of algorithm output with ground validation products including dual-polarimetric radar retrievals and disdrometer measurements. Chapters 3 and 4 draw heavily from a manuscript that has been submitted and conditionally accepted to the *Journal of Applied Meteorology and Climatology* as Munchak and Kummerow (2010).

Algorithm results and their interpretation can be found in the next two chapters. Chapter 5 provides global maps of the retrieved rain DSD parameters and relates them to surrounding cloud and environmental properties. Much of this material comes from a manuscript that has been submitted to the *Journal of Climate* as Munchak et al. (2010). Chapter 6 interprets the algorithm results in the context of the global energy budget and examines uncertainties in the global mean tropical rainfall rate.

The key findings, largely corresponding to the questions listed in section 1.2, along with some concluding remarks and suggestions for future work are given in chapter 7. An early part of this work

was an examination of the three-dimensional covariance structure of the rain DSD using observational datasets in order to develop realistic *a priori* constraints on the retrieval. This analysis, not included in the aforementioned publications, is presented in Appendix [A](#). Residual errors in simulated brightness temperatures are examined in Appendix [B](#). Finally, an application of the retrieved profiles as an *a priori* database for radar retrievals is presented in Appendix [C](#)

Chapter 2

A REVIEW OF RADAR, RADIOMETER, AND COMBINED SATELLITE RAINFALL MEASUREMENT ALGORITHMS

Remote Sensing: Look, but don't touch.

—anonymous

In this chapter, a brief overview of rainfall retrieval algorithms is presented. The history, physical basis, and mechanics of radar, radiometer, and combined algorithms are discussed in sections 2.1, 2.2, and 2.3, respectively. Each of these sections includes a description of the current official TRMM algorithm.

2.1 Radar Algorithms

The earliest attempts to measure rainfall with radar by Marshall et al. (1947) found that, in general, a power law relationship between radar reflectivity Z and rainfall rate R existed:

$$Z = aR^b. \quad (2.1)$$

The coefficient a and exponent b of this power law were later provided by Marshall and Palmer (1948), whose values are still in wide use today. Despite this common usage, it was quickly recognized (e.g., Atlas and Chmela (1957)) that these parameters varied widely and seemed to be associated with synoptic conditions. It is now recognized (e.g., Brandes et al. (2006)) that the power law of Marshall and Palmer (1948) is more representative of frontal stratiform rainfall, which is the predominant rainfall type in Ontario, Canada where the radar and rainfall observations upon which this power law was based were taken. Convective and tropical rainfall, for example, is observed to have a smaller coefficient a (Tokay and Short, 1996). A more comprehensive review of varying power law relations is given in section 5.1.

For the purposes of this chapter, is sufficient to recognize that the non-uniqueness of the Z-R relationship is a fundamental result of the general equations for effective radar reflectivity and rainfall rate:

$$Z_e = \frac{\lambda^4}{\pi^5 |K^2|} \int_{D_{\min}}^{D_{\max}} N(D) \sigma_b(D, \lambda) dD, \quad (2.2)$$

where $|K^2|$ is the dielectric constant, λ is the radar wavelength, and σ_b is the backscattering cross section, and

$$R = \frac{\pi}{6} \int_{D_{\min}}^{D_{\max}} D^3 N(D) v(D) dD, \quad (2.3)$$

where $v(D)$ is the drop fall speed. Owing to the fact that vertical air motions are small near the ground and that raindrops achieve terminal fall velocity within about 100m (Pruppacher and Klett, 1997, Section 10.3.6), formulae relating terminal fall speed to drop size are often used. A simple power law such as $v(D) = 17.67D^{0.67}$ (where V is in m s^{-1} and D is in cm) (Atlas and Ulbrich, 1977) is convenient for calculation of Z-R power law coefficients by combining equations 2.2 and 2.3, especially when an analytic form of the drop size distribution $N(D)$ is assumed. Slightly more accurate piecewise power laws such as the one given by Beard (1976) account for different hydrodynamic regimes as drops grow in size, and this is the relationship used for all rain rate calculations in this work.

The backscattering cross section depends on diameter and the size parameter ($\pi D/\lambda$) by Mie theory (Mie, 1908) as shown in Figure 2.1. For sufficiently small size parameters (small drops and/or long wavelengths) the Rayleigh approximation holds:

$$Z = \int_{D_{\min}}^{D_{\max}} N(D) D^6 dD. \quad (2.4)$$

Thus, while reflectivity is approximately proportional to the 6th moment of the DSD, rain rate is proportional to a much lower (3.67th) moment. This is illustrated in Figure 2.2, which shows the relative contribution of different drop sizes to reflectivity and rain rate for a example exponential DSD. Thus the fundamental problem is radar meteorology is that multiple values of R can be associated with a single value of Z .

For years, the field of radar meteorology has developed solutions this problem in the form of multi-parameter radars. Dual-polarimetric radars measure reflectivity at horizontal and vertical polarization, along with the differential phase (K_{DP}) and linear depolarization ratio (L_{DR}) (Bringi and Chandrasekhar,

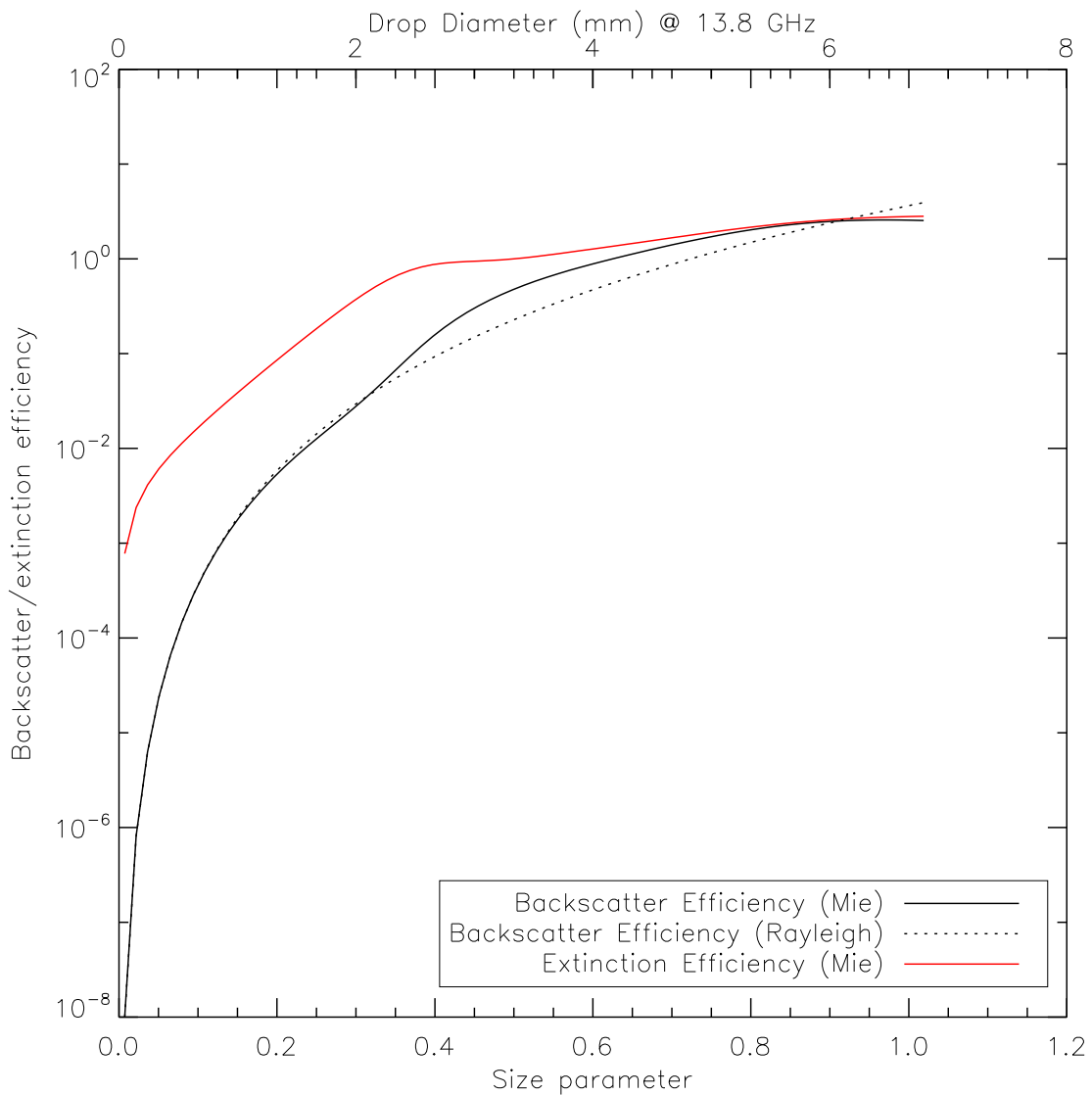


Figure 2.1: Backscattering and extinction efficiency from Mie and Rayleigh theory. Corresponding cross sections can be found by multiply efficiency by actual drop cross-sectional area.

2001). Relationships between these parameters and R (e.g., [Bringi et al. \(2004\)](#)) have been developed based on the physical principle that large raindrops assume oblate spheroidal shapes ([Beard and Chuang, 1987](#)) and propagation of the radar beam through them results in unequal backscatter between the vertically and horizontally polarized waves.

An alternate solution has been the use of dual-frequency radars. In addition to the dependence of reflectivity on the size parameter, there is also a wavelength dependence of the extinction cross section

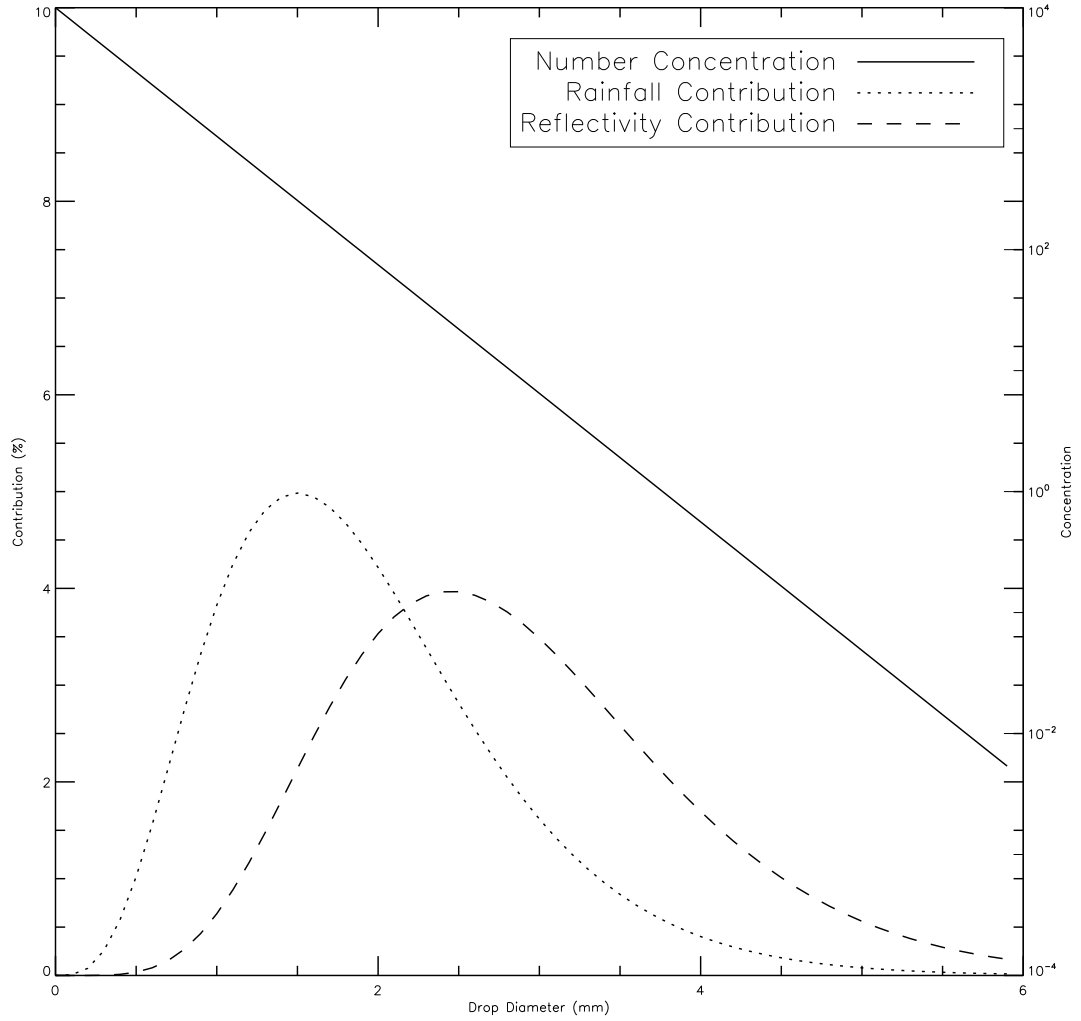


Figure 2.2: Contribution of Different Drop Sizes to Rainfall and Reflectivity for an assumed exponential distribution. Contribution percentages are for 0.1-mm bins.

σ_e (Figure 2.1), which affects the amount by which the radar beam is attenuated. The specific attenuation is given by:

$$k = \int_{D_{\min}}^{D_{\max}} N(D)\sigma_e(D, \lambda)dD, \quad (2.5)$$

and the measured reflectivity at range r can then be given by:

$$Z_m(r) = Z_e(r)e^{-0.2\ln(10) \int_0^r k(s)ds}, \quad (2.6)$$

taking into account the two-way path-integrated attenuation (PIA). By knowing the differential attenuation¹, both Z and k are known and since k is proportional to the 3rd moment of the DSD, the rain rate is much better constrained than by Z alone.

The Precipitation Radar (PR) on board the TRMM satellite is neither dual-polarimetric² nor dual-frequency. A dual-frequency radar was originally planned (Simpson et al., 1988) but reduced to a single frequency for budget reasons. The power and size constraints of a spaceborne platform also necessitate a higher frequency (13.8 GHz) where large raindrops do not scatter according to the Rayleigh approximation (Figure 2.1) and attenuate significantly. For further technical details regarding the PR the reader is referred to Kummerow et al. (1998).

Since the TRMM PR operates at an attenuating frequency, a correction for this attenuation must be made. A radar algorithm that corrects for attenuation was first described by Hitschfield and Bordan (1954). This method uses a forward-recursion technique that assumes no attenuation at the first range gate. A $Z - k$ relationship is then used to calculate the attenuation that occurs in this range gate, correct for it in the following range gate, and so on. However, this method is numerically unstable because small changes in the $Z - k$ relationship can lead to large changes in PIA at far range gates. An example, illustrated in Figure 2.3 shows why this is the case. If the estimated attenuation is too large, then corrected reflectivities will be overestimated. These overestimated reflectivities will produce an even larger attenuation correction in further range gates, which will result in even larger reflectivities and attenuation estimates which can quickly increase exponentially to unphysical values.

The attenuation at the TRMM radar frequency is a potential source of error, if not accurately corrected, but also an additional source of information. Equation 2.6 includes an attenuation term that can be used to define the PIA in dB:

$$\text{PIA} = -10\log_{10} \left(\frac{Z_m(r)}{Z_e(r)} \right) = -10\log_{10} (e^{-0.2\ln(10) \int_0^r k(s) ds}). \quad (2.7)$$

If a reflector of known effective radar cross section is placed at the end of the path, then the ap-

¹ Most commonly, by using one wavelength for which attenuation is negligible, *e.g.*, Eccles and Mueller (1971).

² The nadir view of raindrops is symmetric, thus no information about drop size is contained in the differential reflectivity but some information about phase is still contained in L_{DR} . Nevertheless, this capability was eliminated for budget reasons.

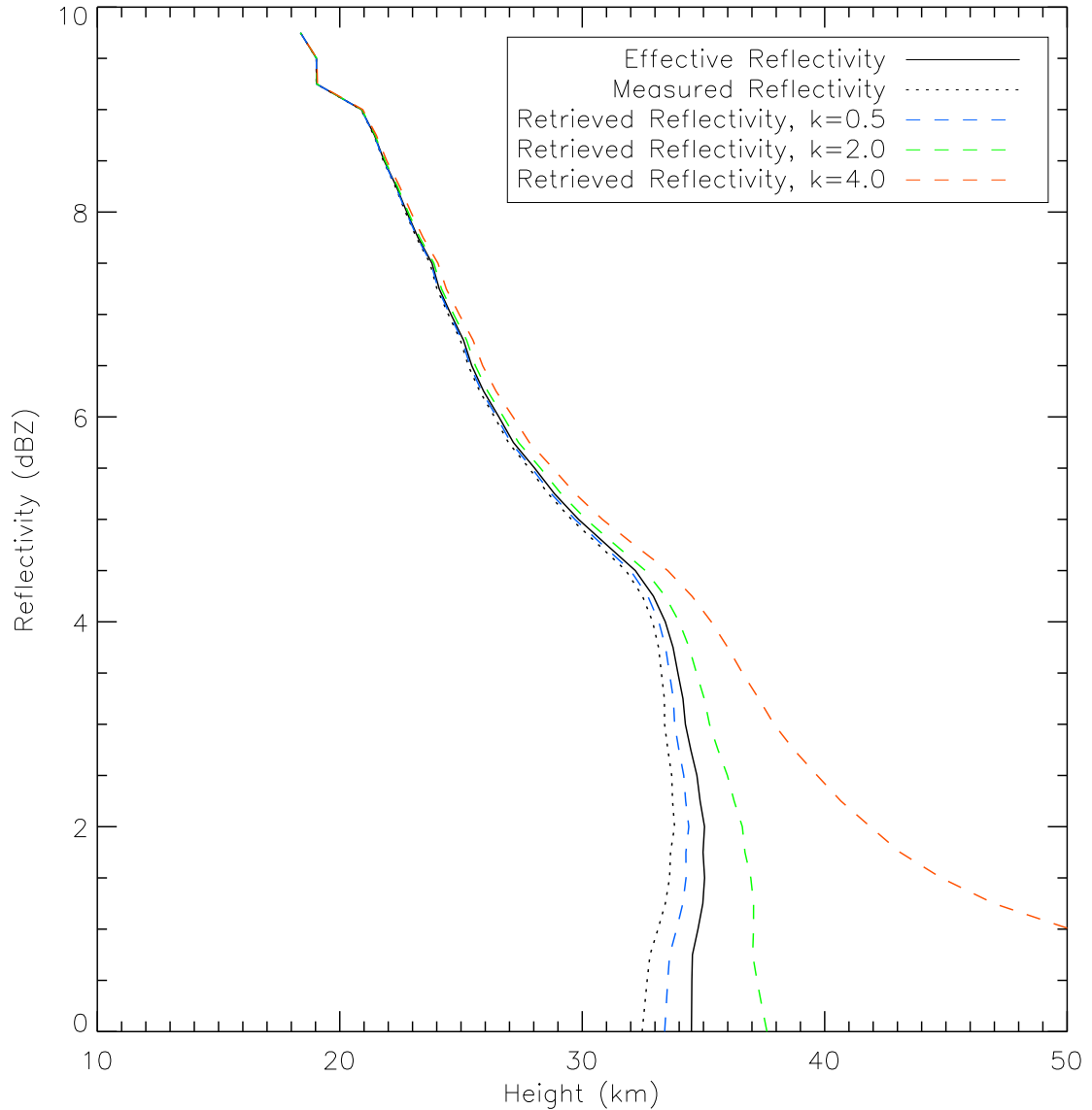


Figure 2.3: An example attenuation-correcting radar profiling algorithm. The true effective reflectivity (solid) is attenuated to the measured signal (dotted). An attenuation correction is applied assuming a $Z - k$ relationship that is half (blue), twice (green), and four times (red) the nominal value.

parent decrease in this cross section from its known value is equal to the PIA. Fortuitously, a downward-looking radar has exactly such a reference cross section in the earth's surface itself. This fact was recognized by [Meneghini et al. \(1983\)](#) and forms the fundamental basis for the TRMM operational radar algorithm, known as product 2A25 (Table 3.4).

This so-called surface reference technique ([Meneghini et al., 2000](#), SRT) can be used to determine

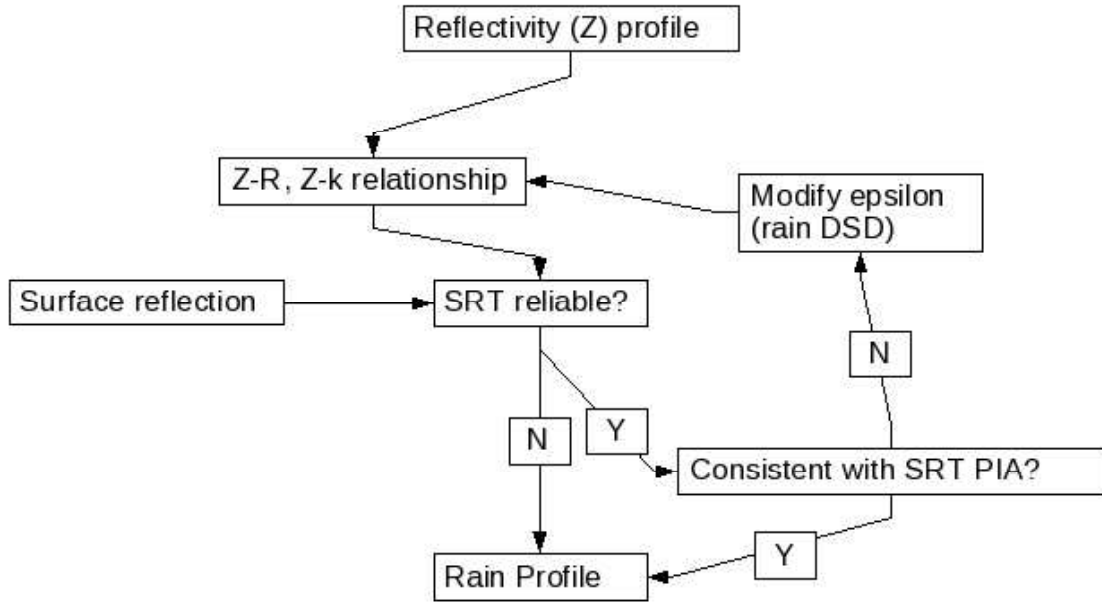


Figure 2.4: Schematic Diagram of the 2A25 Radar-Profiling Algorithm

the attenuation-corrected reflectivity at the range gate nearest to the surface. Then, a backwards recursion algorithm is used to correct reflectivities towards the radar. The $Z - k$ relationships can then be adjusted such that the calculated and measured reflectivity at the range gate nearest to the radar match. This method contains two complications: it requires a vertical profile of $Z - k$ relationships, and is subject to noise in the SRT PIA estimate. The operational 2A25 algorithm (Figure 2.4) is largely designed to address these two issues.

The vertical profile model in the 2A25 algorithm contains five nodes at which $Z - R$ and $Z - k$ relationships are specified: echo top, top of melting layer, middle of melting layer, bottom of melting layer, and bottom of rain layer (Iguchi et al., 2000). The coefficients of these relationships are interpolated in-between nodes. At each node, a hydrometeor model is used to relate the $Z - R$ and $Z - k$ coefficients to a single parameter ϵ , which is a proxy for the DSD (Kozu et al., 2009). The value of ϵ which matches the SRT PIA is designated ϵ_0 .

Even though ϵ_0 results in a PIA that is consistent with the SRT, it may not necessarily represent the true reflectivity and rain rate profile. This is because the PIA estimate itself is subject to noise. In practice, the SRT PIA is calculated using either a spatial reference or temporal reference. The spatial

reference is a running mean and standard deviation of surface cross section in profiles without a rain echo for each of the 49 angle bins that PR samples. The temporal reference is a database of the mean and standard deviation for each angle bin for each $1^\circ \times 1^\circ$ grid box. The estimate with the lower standard deviation (typically 1.7 dB) is used as the SRT PIA. Figure 2.5 illustrates the distribution of SRT PIA as a function of the highest measured reflectivity in the profile. Note that, due to the noise in the SRT database, many weak-reflectivity profiles have a negative PIA, which is unphysical. To account for this possibility, the 2A25 algorithm weights the final solution as a combination of that given by ϵ_0 and that given by the default relationships ($\epsilon = 1$). This weighting is described by Iguchi et al. (2000) and generally favors the default solution unless the PIA exceeds approximately 4 dB.

In summary, radar algorithms have historically sought to produce exact solutions using relationships between the radar reflectivity and rainrate that correspond to an assumed DSD. When additional information is available, either in the form of polarimetric parameters, reflectivities at multiple frequencies, or in the case of the TRMM PR, independent estimates of attenuation, the rainrate can be better constrained.

2.2 Radiometer Algorithms

The earliest attempts to measure rainfall over oceans with a satellite-based microwave radiometer were performed by Allison et al. (1974) using the electrically scanning microwave radiometer (ESMR) on board the Nimbus 5 satellite. This radiometer had a single, horizontally-polarized channel at 19.35 GHz. With only a single channel, a relationship between brightness temperature and rain rate was derived, ignoring possible variations in the sea surface temperature or emissivity. Despite these limitations, the microwave data proved to uniquely identify the areas of heaviest rain that were not distinguished in other forms of satellite imagery. Further refinements to this technique were made by Wilheit et al. (1977), but it was not until multi-frequency, multi-polarization measurements were available with the Scanning Multichannel Microwave Radiometer (Gloersen and Hardis, 1978, SMMR) and the Special Sensor Microwave/Imager (Hollinger et al., 1990, SSM/I) that more sophisticated algorithms could be developed.

With additional channels, the precipitation signal could be better isolated from the surface emis-

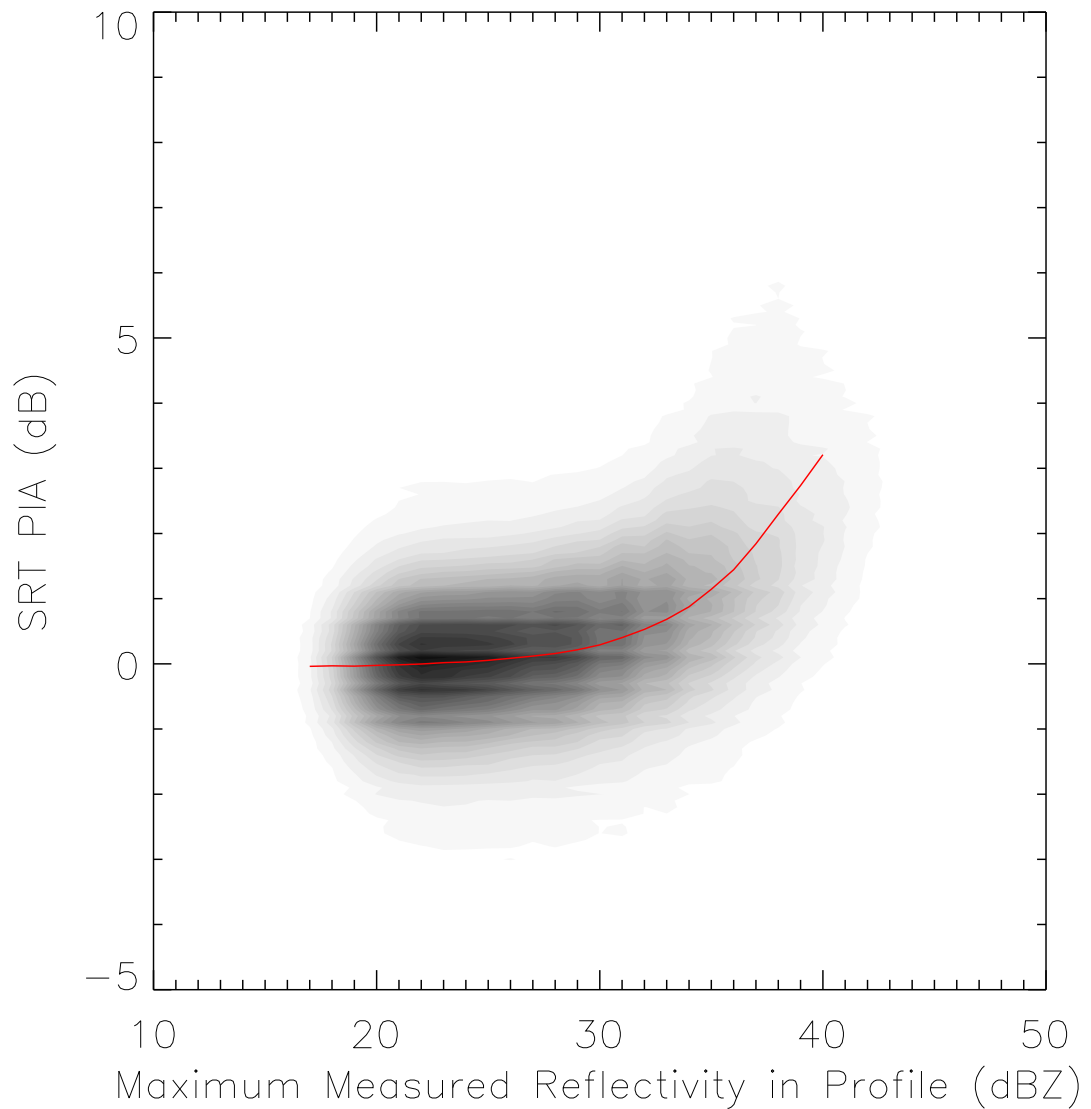


Figure 2.5: Contour plot of the distribution of SRT PIA as a function of maximum measured reflectivity during the month of January 2001. Mean values of PIA at 1-dBZ intervals are plotted in red.

sion. Additionally, the presence of higher-frequency channels allowed use of the ice scattering signal as well as the lower-frequency emission. Early algorithms (*e.g.*, Spencer (1986), Prabhakara et al. (1986), Hinton et al. (1992)) began to take advantage of radiative transfer models (*e.g.*, Huang and Liou (1983), Wu and Weinman (1984), Kummerow and Weinman (1988)) and idealized cloud profiles to create empirical relationships between T_b s and the surface rainfall rate.

At this time two problems became apparent. As with radar, there was not a unique relationship be-

tween the measurement (in this case, a set of T_b s) and the rainfall rate, due to differences in the rain DSD (McKague et al., 1998), water vapor and cloud liquid water content (Berg et al., 2006), and precipitation ice (Bennartz and Petty, 2001), among other factors (Figure 2.6). Additionally, the low spatial resolution (approximately 30km) of many of the rain-sensitive channels resulted in the necessity of assumptions regarding the nonuniformity of rain within a single radiometer field-of-view (FOV) (Wilheit, 1986). Partly stemming from these issues, there was a divergence of algorithms into those that attempted to measure instantaneous rain rates (e.g., Mugnai et al. (1993), Kummerow and Giglio (1994) and Smith et al. (1994)), and those that used regional probability density functions (pdfs) of T_b s to calculate long-term mean rain rates (Wilheit et al. (1991), Chang et al. (1999)).

A key improvement in the Kummerow and Giglio (1994) algorithm, which came to be known as the Goddard Profiling Algorithm (GPROF), was the replacement of idealized cloud layers with a database of cloud profiles from cloud-resolving model simulations (Kummerow et al. (1996), Kummerow et al. (2001)). Since these databases provided a sample distribution of more realistic cloud profiles, Bayes' theorem could be invoked to obtain the most probable rain rate from a set of brightness temperatures:

$$P(R|T_b) = P(R) \times P(T_b|R). \quad (2.8)$$

Thus, each profile in the database is assigned a weight based upon how well it matched the observed T_b s and the retrieval result is a weighted average of these profiles.

Due to the difficulties in obtaining representative samples over large oceanic regions in which the physical retrieval algorithms operate, relatively few validation studies have been performed. Bowman (2005) compared TMI (GPROF) and PR (2A25) retrievals to rain gauge measurements from buoys in the Tropical Pacific Ocean and found that the bias of TMI in this region was only 3% lower than the gauges. Wolff et al. (2005) and Wolff and Fisher (2008) compared the TRMM satellite products to ground validation sites (gauge-tuned radar estimates) and found slightly larger errors, generally between 5% and 10%, which systematically varied at different sites. Potential error sources were examined by L'Ecuyer and Stephens (2002b) and Kummerow et al. (2006), who found that database correctness and representativeness were both potential problems. The correctness problem is a result of the fact that multiple distinct profiles may all produce the same set of T_b s. Thus, the distribution of profiles in

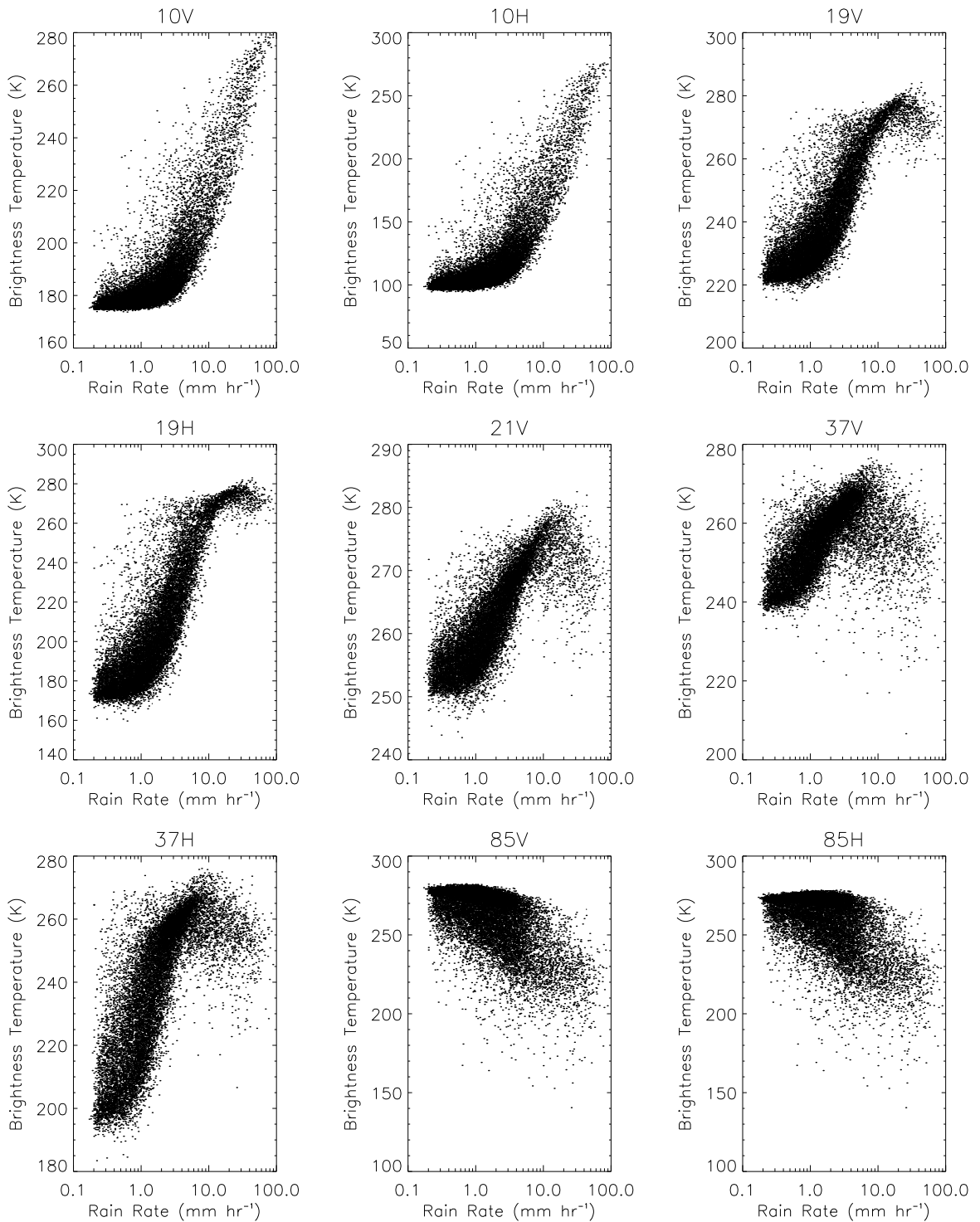


Figure 2.6: Brightness Temperature versus Rain Rate from PR profiles near Kwajalein over a 6-month period. Brightness temperatures were calculated at the PR resolution, so these data do not account for partial beam-filling effects at the larger TMI FOVs.

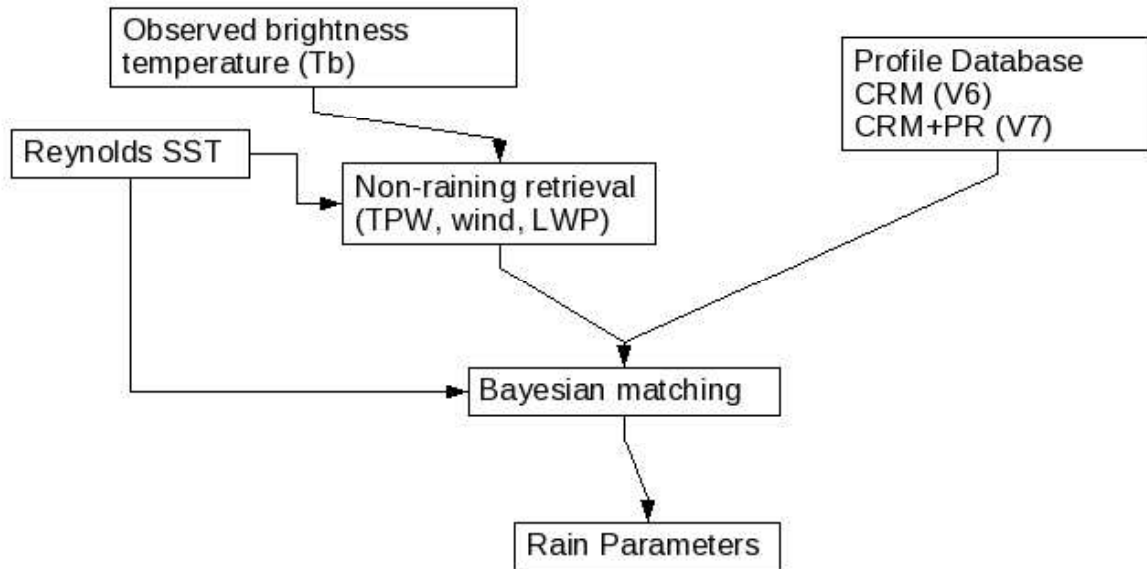


Figure 2.7: Schematic Diagram of the GPROF radiometer rainfall retrieval algorithm.

the database must match the distribution in nature, pr results will be biased. In order to remedy these problems, the most recent version of GPROF (GPROF2008; Figure 2.7) uses a database of profiles that come from the TRMM PR (Kummerow et al., 2010). However, many of the PR profiles did not reproduce the observed T_b s. A conservative adjustment strategy was adopted that grouped profiles by SST and TPW, then added or removed cloud water and drizzle in nonraining pixels so that each TPW/SST bin was unbiased at 19 GHz. Errors in individual modeled and observed T_b s could still be quite large for individual profiles under this strategy.

2.3 Combined Algorithms

Although the theory for multi-measurement retrievals has been reasonably well established (Rodgers, 2000), a problem posed by the multi-instrument data provided by TRMM and other platforms such as the A-Train (Stephens et al., 2002) lies in the greatly differing resolutions and mismatched instrument fields-of-view (FOVs), especially where the FOVs are significantly larger than the scale of the features being retrieved. With the launch of TRMM in 1997, new retrieval schemes were developed to combine measurements from the TMI and PR to retrieve hydrometeor profiles consistent with both sets of

measurements.

The initial operational combined algorithm for TRMM (Haddad et al., 1997) sought only to adjust the PIA via empirical relation to the extinction measured in the 10 GHz channel. In this algorithm, each PR pixel was sensitive to the 4 nearest TMI 10 GHz FOVs and a Bayesian approach was used to adjust the radar-derived rain profiles in the intersection of these 4 footprints to match the observed brightness temperatures. Since then, algorithms have been developed to utilize information from all TMI channels to enhance the PR retrieval and to generate databases to be used in passive-only retrievals. Grecu et al. (2004) and Masunaga and Kummerow (2005) independently developed methodologies to match PR observations to a database of hydrometeor profiles generated from CRMs. Brightness temperatures are then simulated from these profiles and convolved to the TMI channel FOVs. In both of these algorithms, an adjustment is made to the DSD in the hydrometeor profile to simultaneously match the TMI-observed brightness temperatures; however, the methodologies differ in how these adjustments are made.

Masunaga and Kummerow (2005) developed a technique primarily intended to adjust the CRM databases of raining profiles and associated brightness temperatures to be used in passive-only retrievals. Initial profiles were selected based upon similarities in the observed and CRM reflectivity profiles, and T_{bs} were computed from the modeled profiles at the PR resolution. The modeled T_{bs} were then convolved to the TMI resolution, and compared to observed T_{bs} that were interpolated at each pixel. Thus, the adjustment made to the DSD to account for the difference in observed and modeled brightness temperature is done independently for each PR pixel. A shortcoming of this method is the implicit assumption that each PR pixel within a given TMI FOV is equally responsible for the difference in observed and modeled brightness temperature. This assumption may not be valid for scenes with a significant variability in rainfall physics within an FOV.

Grecu et al. (2004) formulated a retrieval that modified a parameter of the DSD in the hydrometeor profiles. The initial profiles were derived by matching reflectivities to a CRM database, similar to Masunaga and Kummerow (2005). Unlike their retrieval, however, Grecu et al. (2004) perform the retrieval on multiple TMI FOVs and PR profiles simultaneously due to the overlapping nature of the TMI FOVs. Their retrieval minimized a cost function consisting of three terms: the difference between observed and modeled values of an index related to brightness temperature, the deviation of the modified DSD par-

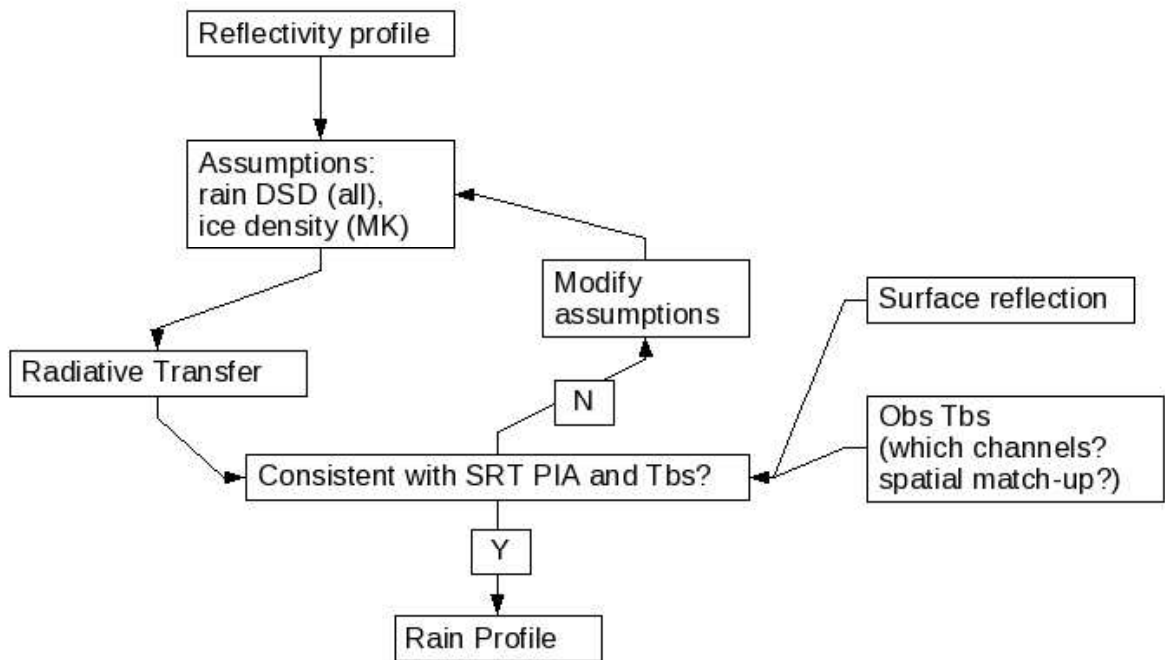


Figure 2.8: Schematic diagram of the common features in the [Haddad et al. \(1997\)](#), [Grecu et al. \(2004\)](#), and [Masunaga and Kummerow \(2005\)](#) combined algorithms.

ameter from its spatial average, and difference between the radar-estimated and modeled path-integrated attenuation (PIA). All of the terms in the cost function are weighted by covariances which represent the expected deviation between observed and modeled values, and mostly represent uncertainties in non-retrieved parameters that nevertheless are necessary to perform the radiative transfer calculations. The authors noted that the the values of covariances were somewhat uncertain, and performed an analysis showing that the retrieval was rather sensitive to their magnitudes. Thus a more precise estimate of these errors, or a formulation that is less sensitive to their relative magnitudes, is desirable for increased confidence in the retrieved precipitation estimates.

The primary differences in these algorithms (common features are illustrated in [Figure 2.8](#)) are how the radar reflectivity is used to generate a hydrometeor profile (either via a profiling algorithm or Bayesian matching), and how the TMI radiances are incorporated, including channel selection and down-scaling of the low-resolution TMI FOVs to the relatively high-resolution PR footprint. All of the methods described above assume that the DSD is the source of differences between observed and modeled T_{bs} ,

but this need not be the case as T_b s are also sensitive to the ice particle size distribution (PSD), surface emissivity, cloud water profile, and water vapor profile.

Chapter 3

ALGORITHM DESCRIPTION

A brief outline of the relevant aspects of optimal estimation theory is given in this chapter, followed by a detailed description of the radar profiling algorithm. The incorporation of this algorithm into the larger framework of the combined retrieval is then described. This chapter closes with an analysis of the information added to the radar-based retrieval by the TMI observations and details of the implementation for retrieving full TRMM orbits.

3.1 Optimal Estimation Theory

Optimal estimation (OE) is an inversion method that has been devised for retrieving a set of parameters \mathbf{x} , which represent the true state of the system being observed, from a set of measurements \mathbf{y} that are related through a forward model, $\mathbf{y} = f(\mathbf{x})$. This methodology was originally applied towards temperature and humidity soundings, however, it has recently been applied to radar (L'Ecuyer and Stephens, 2002a) and lidar (Mitrescu and Stephens, 2002) retrievals. This methodology is described in detail by Rodgers (2000); a brief summary is presented here. Optimal estimation seeks to find the set of parameters $\hat{\mathbf{x}}$ that minimizes the cost function

$$\Phi = (\mathbf{y} - f(\hat{\mathbf{x}}))^T \mathbf{S}_y^{-1} (\mathbf{y} - f(\hat{\mathbf{x}})) + (\hat{\mathbf{x}} - \mathbf{x}_a)^T \mathbf{S}_a^{-1} (\hat{\mathbf{x}} - \mathbf{x}_a), \quad (3.1)$$

where \mathbf{S}_y is the measurement covariance matrix. This cost function differs slightly from that of Grecu et al. (2004) in the inclusion of \mathbf{x}_a , the *a priori* parameter set, and its covariance matrix \mathbf{S}_a . Without \mathbf{x}_a , the solution only minimizes the variance in the observations, and can be underconstrained. The *a priori* parameter set represents the expected value of the retrieved parameters absent any information from the measurement and prevents extreme, unphysical values from being retrieved. Thus, the two

terms in the cost function represent the weighted differences between the measurements and retrieved parameters from their forward-modeled and expected values, respectively. The relative weighting of these two terms that can substantially influence the location of the minimum cost, thus we describe the covariance matrices in more detail in section 3.3. The diagonal elements in these matrices contain the variances of the elements of \mathbf{x}_a and \mathbf{y} . The off-diagonal elements represent the covariances between different measurements or the retrieval parameters. Non-zero values reduce the cost function if structures in the measurement or retrieval fields resemble those implied by the covariance matrices.

The solution that minimizes the cost function can be calculated iteratively if the forward model is moderately nonlinear, as is the case for radiative transfer. In each iteration, the forward model is linearized by calculating the Jacobian \mathbf{K} , where $\mathbf{K}_{ij} = \frac{\partial y_i}{\partial x_j}$. Then, Newton's method can be used to arrive at a solution once a convergence condition is satisfied. The iterative step is defined as:

$$\hat{\mathbf{x}}_{n+1} = \hat{\mathbf{x}}_n + [(\mathbf{S}_a^{-1} + \mathbf{K}_n^T \mathbf{S}_y^{-1} \mathbf{K}_n)^{-1}] [\mathbf{S}_a^{-1} (\mathbf{x}_a - \hat{\mathbf{x}}_n) + \mathbf{K}_n^T \mathbf{S}_y^{-1} (\mathbf{y} - \mathbf{F}(\hat{\mathbf{x}}_n))]. \quad (3.2)$$

The convergence criterion is usually defined in terms of the closeness of subsequent iterations. One such criterion is that the standardized change in $\hat{\mathbf{x}}$ from one iteration to the next is much less than (in practice, 10% of) the number of retrieved parameters N :

$$(\hat{\mathbf{x}}_{n+1} - \hat{\mathbf{x}})^T (\mathbf{S}_a^{-1} + \mathbf{K}_n^T \mathbf{S}_y^{-1} \mathbf{K}_n)^{-1} (\hat{\mathbf{x}}_{n+1} - \hat{\mathbf{x}}) \ll N. \quad (3.3)$$

The OE methodology also provides useful retrieval diagnostics. The confidence in the retrieved scene can be estimated by calculating the actual value of the cost function (3.1), sometimes referred to as χ^2 because of the statistical distribution it should resemble over a large number of retrievals. The value of χ^2 should not significantly exceed the number of measurements plus the number of retrieved parameters, and a value much larger than this sum indicates either a poor forward model (or non-retrieved parameters) that is unable to match all the measurements within their respective uncertainties, or significant departure from the *a priori* state. An uncertainty value for each retrieved parameter can also be derived from the *a posteriori* pdf which is derived from \mathbf{S}_y , \mathbf{S}_y , and the linearized forward model \mathbf{K} :

$$\mathbf{S}_x = (\mathbf{K}^T \mathbf{S}_y \mathbf{K} + \mathbf{S}_a^{-1})^{-1}, \quad (3.4)$$

Finally, the information content of the measurements can be diagnosed by substituting the linearized forward model into the linear solution (not shown) so that it is of the form $\hat{\mathbf{x}} = \mathbf{A}\mathbf{x} + (\mathbf{I} - \mathbf{A})\mathbf{x}_a$,

where

$$\mathbf{A} = \mathbf{S}_x \mathbf{K}^T \mathbf{S}_y^{-1} \mathbf{K}. \quad (3.5)$$

The diagonal elements of \mathbf{A} indicate the influence of the *a priori* and measurements on the retrieved state. As the A-matrix values approach 1, the retrieved value is increasingly influenced by the measurements over the *a priori* value.

3.2 Radar Profiling Algorithm

An attenuation-correcting radar algorithm was described by [Hitschfield and Bordan \(1954\)](#) using internally consistent relationships between reflectivity Z , hydrometeor content W , and attenuation k to retrieve hydrometeor profiles. This method is numerically unstable, that is, small changes in the $Z - k$ relationship can lead to large differences in the surface rain rate as errors in attenuation estimates amplify towards the surface. However, independent measurements of path-integrated attenuation (PIA) provided by the surface reference technique (SRT; [Meneghini et al. \(2000\)](#)) can provide a constraint on the $Z - k$ relationship or the DSD model used to derive it.

It is worth noting that potential sources of error exist in the PR noise/calibration and attenuation by gases. PR fading noise and calibration errors are small (0.7 dB and within 0.5 dB, respectively) and unbiased ([Akihiro et al., 2004](#)), so they are not expected to be a leading source of error in the combined retrieval. Attenuation by gases (H_2O and O_2) is not a significant source of error even compared to the radar calibration given that the total gaseous attenuation near the surface is around 0.3 dB and its variability is an order of magnitude less. Another potential source of error is the detection threshold of PR, approximately 17 dBZ. The 2A25 algorithm can afford to ignore this problem, since rain of this reflectivity has negligible attenuation, but it may nevertheless contribute to a substantial fraction of the total LWP and thus is important for modelling microwave T_{bs} (e.g., [Berg et al. \(2010\)](#)). Thus, in profiles with sporadic gaps between near-threshold echoes, it is assumed that precipitation exists but was not detected by PR. Our algorithm fills these gaps by adding reflectivity of the lowest value observed in that profile. This has a modest effect on computed T_{bs} , with an increase of up to 5K in the horizontally-polarized 37 GHz channel.

The vertical model of the precipitating cloud requires a description of hydrometeor phase, size

distribution, ice density and morphology (Bennartz and Petty, 2001), and melting layer structure (Olson et al., 2001) at each range gate in order to properly simulate radar reflectivity and upwelling microwave radiances. Due to the computational cost of retrieving multiple variables in each profile, our radar profiling algorithm is designed to capture the natural variability of these properties in as few parameters as possible.

As in many other rain profiling algorithms (e.g., TRMM 2A25 (Iguchi et al., 2000), Grecu and Anagnostou (2002)), a gamma distribution is assumed to describe the rain DSD: $N(D) = N_0 D^\mu e^{-\Lambda D}$, with an intercept parameter (N_0), shape parameter (μ), and slope parameter (Λ). In this model, the median volume diameter D_0 can be expressed as

$$D_0 = \frac{3.67 + \mu}{\Lambda}, \quad (3.6)$$

following Ulbrich (1983). This relationship formulates a power law relating D_0 and Z :

$$D_0 = (3.67 + \mu) \left[[N_0 \Gamma(7 + \mu)]^{-1} Z \right]^{\frac{1}{7+\mu}}. \quad (3.7)$$

The constants can be grouped together to form a more simple power law $D_0 = aZ^b$, where a represents the Z -normalized D_0 and is dependent on N_0 and μ whereas b only depends on μ . It should be noted that these relationships are only strictly valid if Z represents the 6th moment, i.e., Rayleigh reflectivity, which is not true for large raindrops (> 1 mm diameter) at the PR frequency. However, the error introduced by this approximation does not significantly affect the shape of the relationship, so no systematic error is introduced so long as N_0 and D_0 are derived from PR reflectivity values using Mie theory to calculate Z . In order to simplify the retrieval, the coefficients a and b are fixed by rain type (Table 3.2) and, along with the assumption $\mu = 3$, are chosen to approximate the 2A25 default $Z - R$ relationships.

To adjust the $Z - D_0$ relationship (e.g., in order to match the SRT PIA), we define a multiplicative factor ϵ_{DSD} , so that $D_0 = \epsilon_{\text{DSD}} a Z^b$. This type of DSD adjustment is mathematically similar to the δN_0^* adjustment employed by Grecu and Anagnostou (2002) in their profiling algorithm, and the α -adjustment employed by 2A25 (Iguchi et al., 2000). Although this procedure does not allow the $Z - D_0$ relationship to vary with height, analysis of profiler-derived DSDs (Williams, 2008, Appendix A) suggests that this is a reasonable assumption.

The ice phase is treated similarly. An exponential size distribution (*i.e.*, $\mu = 0$) is assumed for both snow and graupel above the melting layer, which is consistent with available aircraft measurements (*e.g.*, (Houze et al., 1979), (Stith et al., 2002)). The following size-density relationships for snow (ρ_s) and graupel (ρ_g), based on Heymsfield et al. (2004) are assumed:

$$\rho_s = 128D^{-0.95}, \quad (3.8)$$

$$\rho_g = 96D^{-0.95}, \quad (3.9)$$

where D is in mm and density in kg m^{-3} and not allowed to exceed the density of pure ice. The snow-graupel partitioning is assumed to be a function of temperature and rain type (figure 3.1) and derived from the database of CRM simulations used in radiometer-only retrievals (Kummerow et al., 2001). Improving the microphysics schemes in these simulations is an active area of research (*e.g.*, Li et al. (2008)) and part of planned pre-launch GPM ground validation.

As with rain, a $Z - D_0$ power law ($D_0 = aZ^b$, where D_0 represents the mass-weighted average diameter of snow and graupel) is used to derive the ice particle size distribution (PSD) from the corrected reflectivity. From this PSD, the attenuation and scattering properties at all TMI frequencies can be calculated. In this study, the equivalent-mass sphere approach has been used to calculate the scattering properties of snow and graupel. This assumption can lead to significant errors in the scattering and extinction parameters for a given ice water content (Petty and Huang, 2010), on the order of the difference between an all-snow and all-graupel column of the same reflectivity. Despite these numerous sources of error, there is minimal impact on the retrieved rainfall because attenuation at radar and lower TMI frequencies is insignificant ($< 0.01 \text{ dB km}^{-1}$ for 1 g m^{-3} at 13.8 GHz). The parameters of the $Z - D_0$ relationships for rain, snow and graupel are given in Table 3.2 and are consistent with the Z-IWC relationships reported by Black (1990). Like the rain DSD, these can be adjusted by a multiplicative factor, which we define as ϵ_{ICE} . This has the effect of increasing or decreasing the ice water path, *e.g.*, to match the scattering signature at 85 GHz.

Our melting layer model is based on the finding of Zawadzki et al. (2005) that the strength of the reflectivity peak is strongly related to the density of the melting ice particles. Our treatment begins

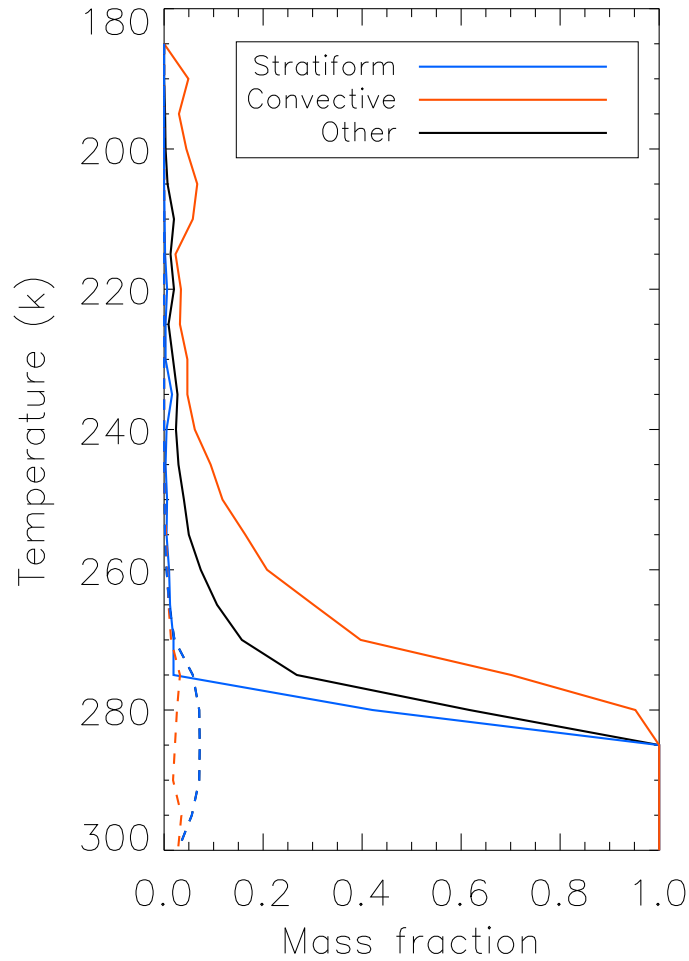


Figure 3.1: Default profiles of graupel (solid) and cloud water (dashed), both as fraction of total precipitation water content.

by finding the peak corrected (2A25) reflectivity (Z_{peak}) within 0.5 km of the horizontally-interpolated bright band height, provided by the standard TRMM 2A23 product. The bright band strength is given by the difference between Z_{peak} and the lowest 2A25 reflectivity within 1km below Z_{peak} and is used to determine the initial snow density at the top of the melting layer. For a given density, there is a relationship between melt fraction and $Z_{\text{peak}}-Z$ (figure 3.2) which is used to determine the dielectric constant and fall velocity ratio at levels up to 0.5 km above and 1 km below Z_{peak} . With this additional information, the PSD is derived using the same μ and $Z - D_0$ relationship as the rain, ensuring continuity between the melting and rain layers.

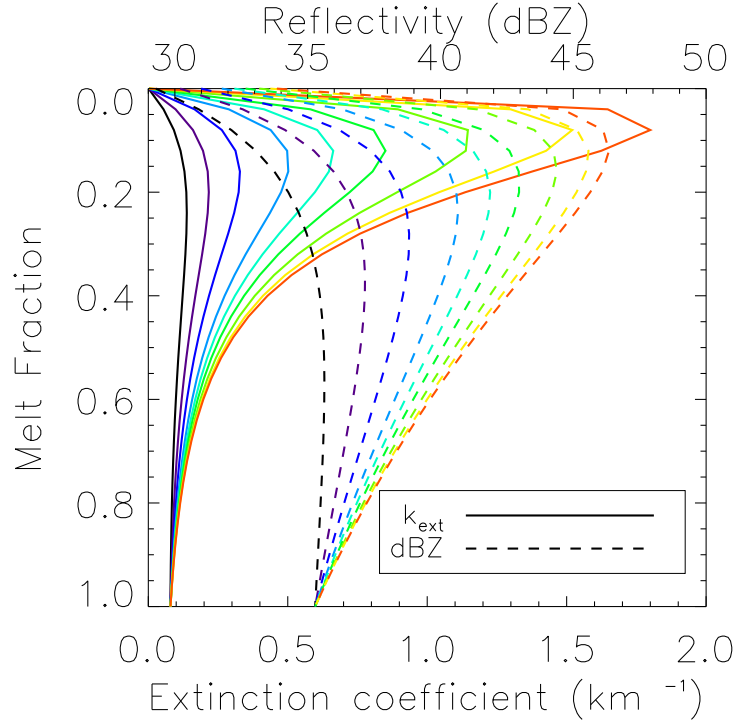


Figure 3.2: Profiles of the 13.8 GHz extinction coefficient and reflectivity for a sample distribution of melting particles. Density decreases going from black to red; values are 50,67,100,150,200,267,400,567, and 800 kg m⁻³.

Although this model does not account for coalescence and breakup, these processes lead to errors of only 1 dB (Fabry and Zawadzki, 1995), only slightly more than the noise in the radar itself. This approach has the advantage of mass consistency from top to bottom of the layer, which is an improvement over static $Z - R$ and $Z - k$ relationships in the melting layer which are not valid at all densities. Furthermore, there is no need for explicitly separate convective and stratiform melting layer models since a weak Z_{peak} implies high particle density, *i.e.*, graupel, whereas a stronger value is associated with lower-density snow.

Cloud water has a small, but non-negligible contribution to attenuation at the PR frequency, and a stronger contribution to T_{bs} , especially at higher frequencies and in lighter rain. Like the snow/graupel partitioning, default cloud water profiles are derived from the CRM database (figure 3.1) for each rain type. Since the cloud liquid water path (cLWP) makes an important contribution to microwave T_{bs} , particularly in light rain, we define a third adjustable parameter, ϵ_{CLW} , which is used to multiply the

Table 3.1: Summary of retrieval parameters.

Parameter	Description
ϵ_{DSD}	Median raindrop size (D_0) divided by aZ^b
ϵ_{ICE}	Median ice particle size divided by aZ^b
ϵ_{CLW}	Multiplicative factor for default cloud water profile

default cLWP equally at all levels in the combined retrieval algorithm.

In summary, the profiling algorithm converts the observed reflectivity profile into a profile of hydrometeor PSDs with three adjustable parameters: ϵ_{DSD} , ϵ_{ICE} , and ϵ_{CLW} (Table 3.1). From top down, an attenuation correction is made at each range gate, the PSD is derived from the corrected reflectivity and ϵ values, and the process is repeated to the lowest clutter-free bin, below which the same DSD is extrapolated to the surface. This process is similar to 2A25, although there are differences in details of the ice, mixed phase, and cloud water models.

Perhaps the most important difference is in incorporation of the SRT PIA. Since the standard deviation of the SRT can be greater than the PIA estimate itself in light and even moderate rain, the profiling algorithm needs to account for this to prevent unphysical profiles from being retrieved. The 2A25 algorithm uses a combination of the default and SRT solution that gives higher weight to the SRT PIA in heavy rain, where the SRT is most reliable. With the OE methodology, the default and SRT solution can be weighted with knowledge of the variance of the SRT, which is known, and the variance of ϵ_{DSD} , which has not been defined. When our profiling algorithm is used without radiometer input, we desire that the global rainfall estimates be unbiased relative to 2A25 to serve as both a standard reference to compare the radiometer-adjusted estimates and to indirectly utilize the data against which 2A25 itself has been validated. In this simple case, \mathbf{x} consists of ϵ_{DSD} and \mathbf{y} is the SRT PIA, with the profiling

Table 3.2: Default PSD parameters by 2A23 rain type.

Parameter	Convective/Other	Stratiform
a_{rain}	0.4778	0.5973
b_{rain}	0.1210	0.1073
a_{snow}	1.85	1.85
a_{graupel}	0.31	0.31
b_{snow}	0.16	0.16
b_{graupel}	0.16	0.16

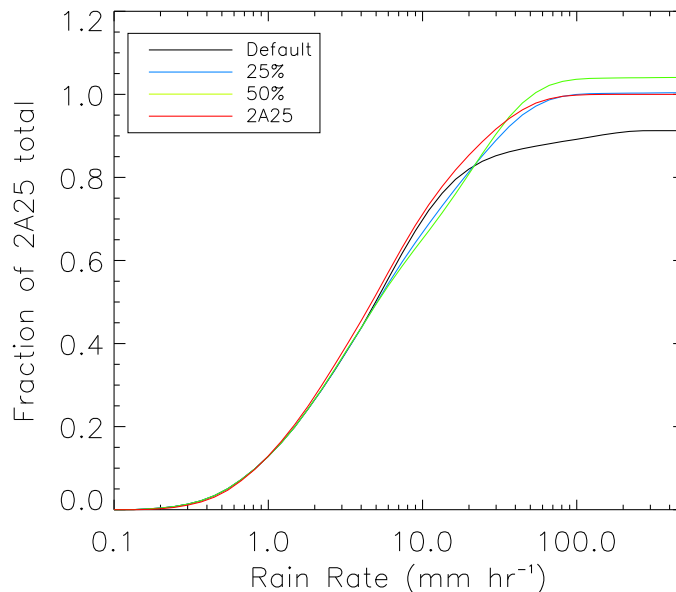


Figure 3.3: Rain CDFs over global ocean for January 2000 using different constraints on the default DSD.

algorithm serving as the forward model to calculate the PIA from the measured Z profile (ϵ_{ICE} and ϵ_{CLW} are not considered in the radar-only retrieval due to their minimal impact upon the PIA). The only free parameter in this retrieval is the uncertainty in ϵ_{DSD} . An analysis of profiler- (Williams, 2008) and polarimetric radar-derived (Matrosov et al., 2002) DSDs suggests a Z -normalized D_0 standard deviation of approximately 35%. One month of global retrievals over ocean provides a best match to 2A25 when 25% variance is assumed. Different variance levels in figure 3.3 illustrate the tradeoff between matching the observations (SRT PIA) versus the constraint of the default DSD. When the constraint on the DSD is strong, it is difficult to adjust rain rates away from the default value, which tends to produce less rain than the standard 2A25 solution.

3.3 Combined Retrieval Framework

This section describes the use of the radar profiling algorithm within the optimal estimation framework along with the other components that are necessary to retrieve precipitation parameters from a combination of radar profiles and microwave radiances. The flow of the overall retrieval is illustrated in figure 3.4. The parameters ϵ_{DSD} , ϵ_{ICE} , and ϵ_{CLW} required by the radar profiling algorithm form the

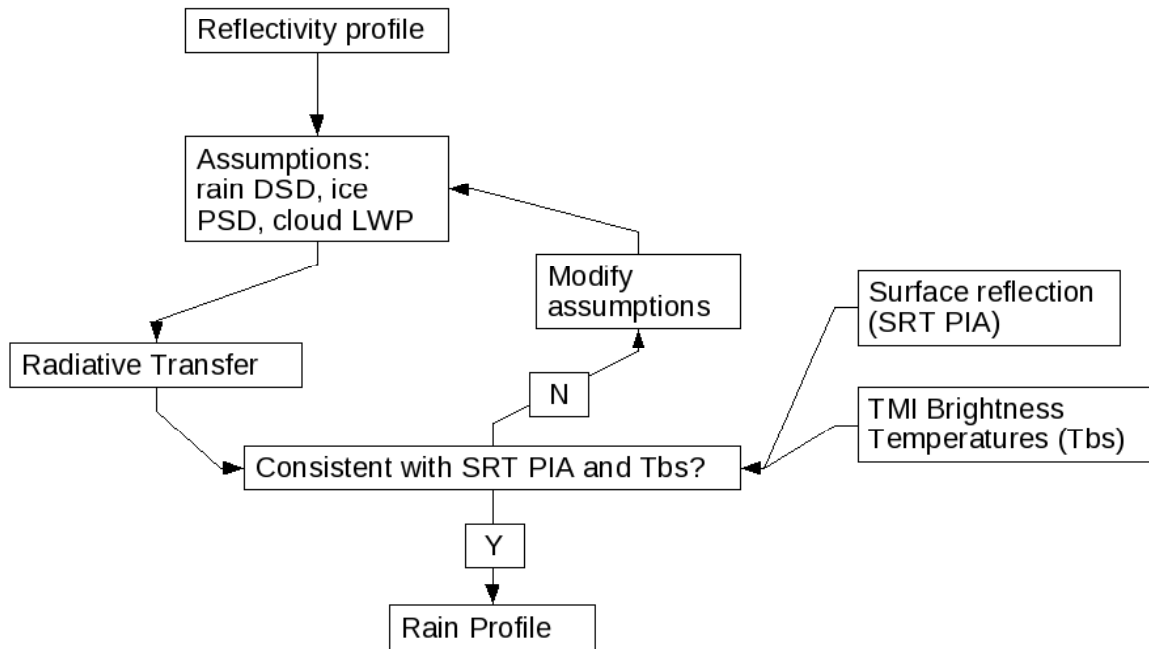


Figure 3.4: Flow chart of TRMM combined PR+TMI retrieval, illustrating the modular nature of the overall algorithm.

retrieval vector \mathbf{x} . In addition, there is another set of parameters that do not affect the radar solution but are necessary to model the T_{bs} . These parameters include SST and surface wind speed, which are necessary for emissivity calculations. A further complication introduced by the relatively large¹ TMI FOVs is that many cover a mixture of raining and non-raining PR pixels (an example is shown in Figure 3.5). In these pixels, the surface emission, cloud liquid water path (cLWP), total precipitable water (TPW), and height of the freezing level need to be known for these pixels in order accurately model the microwave T_{bs} . These parameters are obtained either through ancillary sources or direct retrievals from the TRMM data.

SSTs are derived from a multi-day optimal interpolation (Reynolds and Smith, 1994) of TMI-based SST retrievals (Gentemann et al., 2004). The SST data are gridded at 0.25° resolution, so a bilinear interpolation is used at each pixel. The freezing level at all PR pixels within 300 km of a reliable bright band height is interpolated using an inverse distance scheme with smoothing from the top of the

¹ compared to the PR footprint

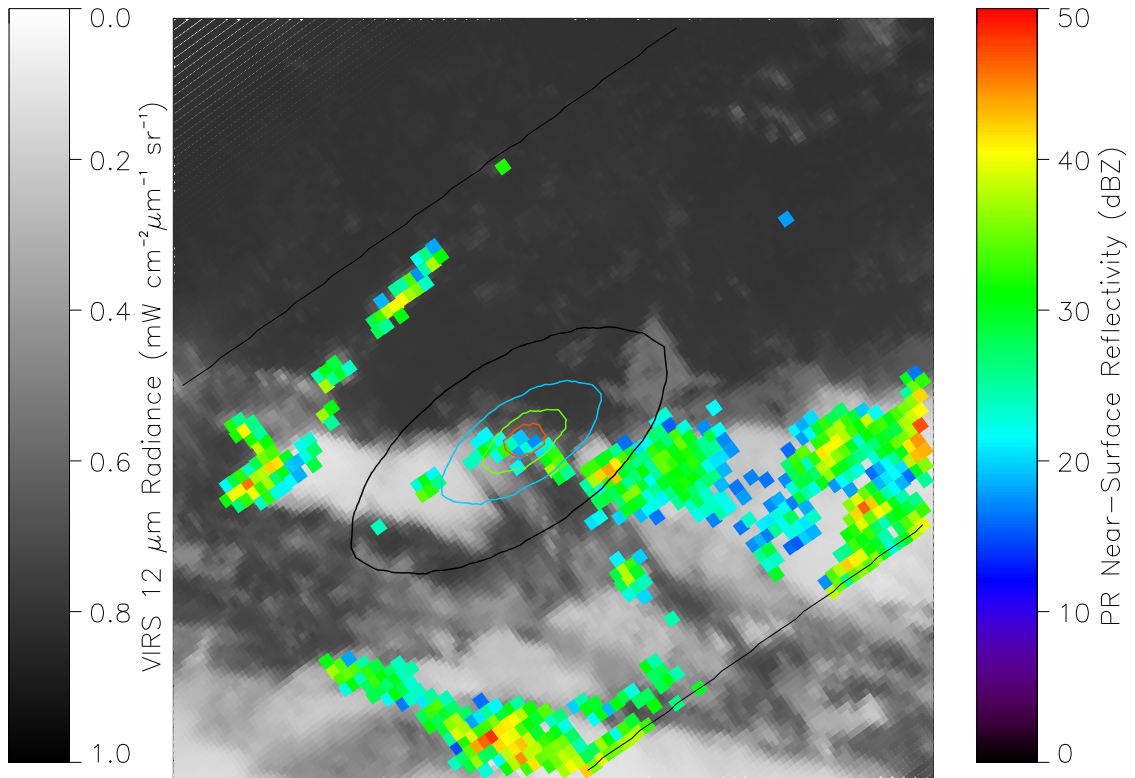


Figure 3.5: An example illustrating that TMI FOVs can contain a mixture of cloud-free sky, nonraining clouds, and raining clouds. Ellipses indicating the size of the 10, 19, 37, and 85 GHz FOVs are colored black, cyan, green, and red, respectively.

bright band as given by the 2A23 product (rain characteristics) where a bright band is detected. For pixels more than 1000 km from a reliable height, the climatological freezing height level used by 2A25 is given instead, and a linear combination is used in between 300 km and 1000 km.

The surface wind, TPW and cLWP are retrieved independently at each TMI FOV using the method of [Elsaesser and Kummerow \(2008\)](#) and interpolated to the non-raining PR pixels. This retrieval is considered valid where the χ^2 error statistic is less than 18, which is indicative of a homogeneous wind, TPW, and cloud water field with no precipitation, and the retrieved wind and TPW field is interpolated into the $\chi^2 > 18$ region which often includes precipitation detected by PR. The temperature profile is calculated assuming a constant lapse rate that is calculated from the freezing height and SST (with a maximum of 7K km^{-1}), and a scale height of 2.3 km is assumed for water vapor. In pixels with a radar echo, wind is interpolated as in the rain-free pixels, but the water vapor values are adjusted to 95% RH

Table 3.3: Observations and retrieval parameters (all at PR pixel scale) used in each OE module.

OE Module	TMI Obs	PR Obs	Retrieved Parameters
Cloud/Drizzle	19,37,85 GHz, < 10% rain coverage	none	cloud+drizzle LWP
Ice	85 GHz, > 50% rain coverage	dBZ	ϵ_{ICE}
Rain DSD/Cloud Water	10,19,37 GHz, > 50% rain coverage	dBZ, PIA	$\epsilon_{DSD}, \epsilon_{CLW}$

in range gates with an echo.

Since many of the TMI FOVs are only partially filled with raining PR pixels, it is necessary to have an accurate representation of the non-raining parameters outside the raining pixels. The chief cause of poor non-raining retrievals, aside from rain, is sub-FOV inhomogeneity of the cloud water field (Rapp et al., 2009) as well as contributions from drizzle, which has larger drops that create a different T_b signature than cloud water, but are too small to be detected by PR. Thus, we retrieve the cloud+drizzle LWP for all non-raining PR pixels that were within 30 km (approximately the size of a 19 GHz FOV) of any TMI non-raining retrieval that did not meet the χ^2 test or are adjacent to a PR pixel with rain. Cloud is assumed to transition to drizzle once a LWP of 150 g m^{-2} is reached; this is based on a median value inferred from CloudSat and MODIS observations by Kubar et al. (2009), and has a slight effect on the modeled T_b s at a given total LWP. In order to maintain continuity among raining and non-raining pixels, the retrieved cloud LWP is interpolated into the raining pixels if it exceeds the value given by the default rain water-cloud water relationships. We show in section 4.1 that this procedure improves the correlation of the retrieved cloud water field from the initial non-raining retrieval relative to VIRS retrievals.

The next two routines retrieve the parameters used by the profiling algorithm. Since modifying the ice PSD affects primarily the 85 GHz channels, where the emission signal is saturated even in light rain and therefore insensitive to cloud water/rain DSD modifications, this process is separated from the rain DSD and cloud water retrieval for computational efficiency. Rain and cloud water, on the other hand, must be retrieved simultaneously due to their similar, but not identical, contributions to upwelling microwave radiation at the TMI frequencies. The input observations and retrieved variables (all at PR pixel scale) are listed in table 3.3 for each retrieval.

In each retrieval routine, the *a priori* covariance matrix S_a must be carefully constructed so that

the algorithm can reproduce the variability observed in nature, but not produce unphysical profiles. The variance of ϵ_{DSD} has already been established via matching to 2A25 and observations, but the covariance also needs to be defined, because the observational datasets (Matrosov et al. (2002), Williams (2008)) used to determine the variance of ϵ_{DSD} also show spatial/temporal autocorrelation structure of the form

$$\mathbf{S}_a(i, j) = \mathbf{S}_{a0} e^{-\Delta Z/Z_0 - \Delta L/L_0}, \quad (3.10)$$

where \mathbf{S}_{a0} is the variance of ϵ_{DSD} , ΔZ is the reflectivity difference (in dBZ), Z_0 is the reflectivity scale, ΔL is the distance between pixels i and j (in km), and L_0 is the length scale. Based on the aforementioned datasets (a more detailed analysis is presented in Appendix A), a length scale of 10 km and reflectivity scale of 3 dBZ is used for ϵ_{DSD} , and, lacking sufficient observations for independent determinations, also assumed for ϵ_{ICE} and ϵ_{CLW} . Including these covariances allows for nearby pixels to influence each other if, for example, both have similar reflectivity profiles, but only one has a reliable PIA estimate.

There is less observational evidence for constraining ϵ_{ICE} than ϵ_{DSD} , but a slightly larger value (50%) is sufficient to match nearly all 85 GHz brightness temperatures with reasonable mass continuity within the column. It is likely that some snow/ice may fall below the PR detection threshold and still slightly depress 85 GHz brightness temperatures, which may lead to a low bias in retrievals of ϵ_{ICE} . This problem is effectively minimized by increasing \mathbf{S}_y at 85 GHz, which also reflects the additional uncertainties in modeling the microwave scattering properties of ice particles.

The value chosen to represent the variance of ϵ_{CLW} is especially important, because rain water and cloud water produce similar radiometric signatures, making it easy (with respect to minimizing χ^2) to adjust one at the expense of the other. However, if the rain water content is known, then the variance in ϵ_{CLW} can be set indirectly. This approach is used in section 4.2.

The observation covariance (\mathbf{S}_y) matrices contain the measurement and modeling errors. In addition to the previously described PIA uncertainty, \mathbf{S}_y represents the expected error in the brightness temperatures. This is considered to come from three sources: error in non-retrieved parameters, instrument noise, and radiative transfer model approximations. The first term is calculated by perturbing the non-retrieved parameters (SST by ± 0.7 K, column water vapor by ± 4 mm, wind by ± 1.5 m s⁻¹ follow-

ing [Elsaesser and Kummerow \(2008\)](#)) in each pixel and convolving the perturbations to TMI resolution. Typical values of these errors range from 2-4 K, depending on channel and rain coverage. Instrument noise is much smaller, approximately 0.5 K ([Kummerow et al., 1998](#)), and is also added to the error estimate. If the sum of these is less than 3 K, then the variance is increased to 3 K to account for radiative transfer model error ([Kummerow, 1993](#)). Higher minimum values of 5 K at 37 GHz, and 20% of the T_b depression from 280 K at 85 GHz, are used to account for errors in ice particle modeling as well.

Some hard limits are also set to prevent the profiling algorithm from retrieving unphysical profiles. A lower limit of either 0.3 or the minimum value necessary to perform the Hitschfield-Bordan adjustment to the surface is set on ϵ_{DSD} in reliable PIA pixels, and a lower limit that produces a maximum of 4 dB of attenuation is set in unreliable PIA pixels. This represents the maximum PIA that might be regarded as unreliable by the 2A21 algorithm ([Meneghini et al., 2000](#)) over ocean. Meanwhile, the upper limit on ϵ_{DSD} is set to 3.0, to prevent unrealistically large raindrops from being retrieved. The limits of ϵ_{ICE} are set at 0.2 and 4.0, mainly prevent unphysical mass concentrations. The cloud water limits are set from 1% of the original value to a maximum LWP of 10 kg m^{-2} , based upon autoconversion thresholds in a high-aerosol environment ([Liu and Daum, 2004](#)).

For computational simplicity and continuity with operational algorithms, a modified plane-parallel Eddington approximation along the TMI slant path is used to calculate the upwelling microwave radiances in this particular study, although the overall framework is constructed so that interchangeability with other radiative transfer schemes is possible. The extinction, bulk scattering, and asymmetry properties of rain, snow, graupel, and melting hydrometeor size distributions are computed using Mie theory and stored in look-up tables. Like the radiative transfer model, these tables can be easily interchanged with others, such as those generated from T-matrix or discrete dipole approximations of the hydrometeors which would more realistically simulate scattering properties at multiple frequencies and are thus particularly needed for GPM.

3.4 Implementation

To be of use to the broader community, this section describes the implementation of the conceptual algorithm outlined previously in this chapter with key computational details. The first stage is a pre-

Table 3.4: TRMM products used in the combined algorithm

Name	Description
1B11	Calibrated Microwave Brightness Temperatures
1C21	Measured Reflectivity Profile
2A21	Surface Cross Section and Estimated PIA
2A23	Rain Characteristics (type and bright band properties)
2A25	Rain Profile

processing routine that reads in the TRMM 1B11, 1C21, 2A21, 2A23, and 2A25 products (Table 3.4). This routine also interpolates the freezing level and SSTs to all PR and TMI pixels, adds sub-threshold echoes as described in section 3.2, and performs the non-raining parameter retrieval. Finally, this routine divides an orbit into segments which is necessary to improve computational time.

The definition of an orbit segment is somewhat arbitrary but needs to be larger than a single 10-GHz FOV, and preferably, contain several such FOVs in order to take advantage of that channel’s sensitivity to heavy rain. Conversely, a segment should not be so large that, when filled with rain, the simultaneous retrieval of two parameters (ϵ_{DSD} and ϵ_{CLW}) results in prohibitive computation time. Using Newton’s method to evaluate the non-linear solution to minimize the cost function (Eq. 3.2) requires a number of computationally intensive steps, which have different scaling relationships with the number of raining pixels n .

The calculation of the Jacobian matrix (\mathbf{K}) requires the substitution of modified perturbed values of ϵ_{DSD} , ϵ_{ICE} , and ϵ_{CLW} in each PR pixel followed by a convolution to TMI resolution. Several time-reducing steps are taken to minimize the cost of this calculation. First, non-perturbed T_{bS} at PR resolution only need to be computed once and stored in memory. Likewise, the weighting function of each TMI FOV is calculated once for the entire scene and stored in memory. Then, difference between each perturbed PR pixel-level T_{b} and non-perturbed value is calculated, convolved to TMI resolution, and stored in \mathbf{K} . The limiting step in this procedure is the radiative transfer module which has been optimized through the use of look-up tables for scattering parameters and reduction of the height resolution from 0.25 km to 1 km above the precipitation. Thus, while the Jacobian takes some time to compute, it scales somewhere between $O(n)$ and $O(n^2)$.

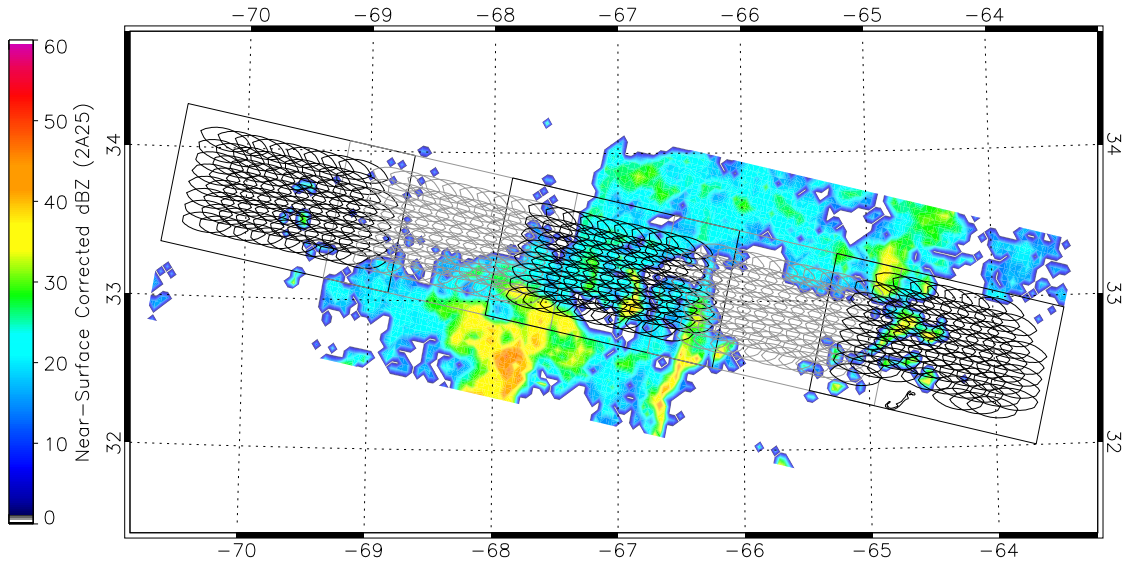


Figure 3.6: Orbit segments covering the central 25 PR pixels overlaid on PR reflectivity for a sample scene. Alternating segments are colored in black and gray, with 19 GHz FOVs (ovals) also shown to give a sense of the geometry of the combined algorithm.

The inversion of the S_x covariance matrix in equation 3.2, meanwhile, takes $O(n^3)$ time steps to compute, and for large scenes becomes the limiting step in the retrieval. As a result of these scaling relationships, a segment size of 49×49 PR pixels was chosen for comparison with ground validation sites in chapter 4. For the full orbits examined in chapter 5, only the central 25 pixels were analyzed with an along-track dimension of 42 pixels, matching the geometry of the TMI FOVs. An overlap region of 12 pixels is included (Figure 3.6) so that no 19 GHz FOVs are excluded due to insufficient coverage. A post-processing routine takes an average (weighted by information content A-matrix value) of the retrieved parameters in the overlap region as the final result.

Using this implementation, a full orbit takes approximately 40 minutes on a 3 GHz Intel Xeon CPU with 8MB of L2 cache. By running multiple orbits simultaneously on a machine with 4 dual-core CPUs a year of data can be processed in approximately two weeks.

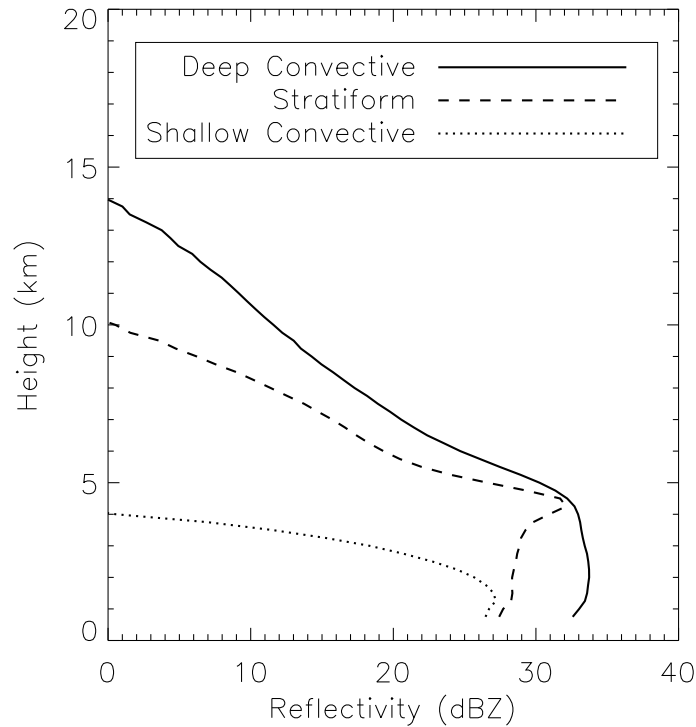


Figure 3.7: Composite reflectivity profiles used in sensitivity analysis.

3.5 Sensitivity and Information Content

A particularly interesting outcome of this retrieval is the partitioning of rain and cloud water. This partitioning has always been either an explicit or implicit assumption in the TRMM 2A12 and 2A25 products, thus this retrieval offers additional insight by retrieving it directly. However, it is first useful to evaluate the extent to which these two variables can be determined from the measurements.

We consider three reflectivity profiles which are a composite of stratiform, deep convective, and shallow convective rain types near Kwajalein in 2008 (Figure 3.7). The DSD and cloud water ϵ parameters were perturbed so as to produce a wide range of rain and cloud LWPs for each reflectivity profile, along with the associated T_{bs} . Given an uncertainty in the observations (*i.e.*, S_y), we can then determine their constraint on the physical parameters. For each profile, the difference between the perturbed and default T_{bs} and PIA was normalized by standard deviations of 3 K and 0.7 dB, respectively, and are plotted in Figure 3.8.

The constraint provided by PIA is very poor in these profiles, which is not unexpected as they

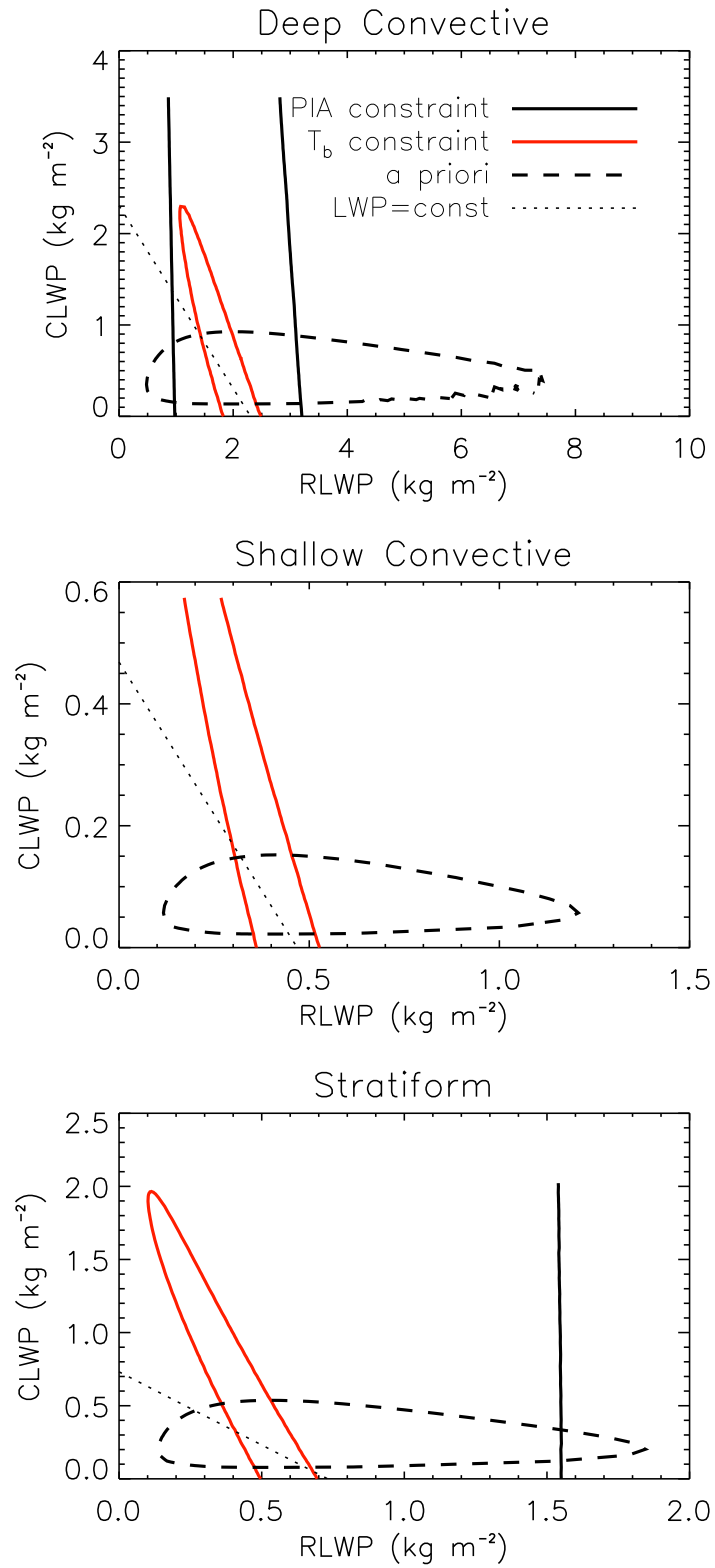


Figure 3.8: Contours of the cost function for various constraint for each sample profile. The light dotted line follows the default value of total liquid water path.

are composites of all rainfall, which skews towards light rain (only the deep convective profile barely exceeds 30 dBZ). The constraint provided by the T_{bs} is much narrower than that provided by the PIA. Although this represents an ideal scenario, *i.e.*, uniform rain within same-size FOVs, there is clearly some additional information present in the microwave radiances. Finally, note that the slope of the region constrained by the T_{bs} is not parallel to contours of constant total LWP, but instead represents a stronger response to rain water than cloud water, a consequence of the increased extinction efficiency of raindrops relative to a distribution of cloud droplets with the same liquid water content due to Mie effects.

The shape and position of the various constraints in Figure 3.8 indicate that the DSD is strongly constrained by the observations relative to the *a priori* constraint, while cloud water is not. A more precise measurement of the information content in the observations is to divide the area constrained by S_a by the area constrained by the full pdf defined by observations and S_a . With the assumption of Gaussian statistics, this can be extended to physical parameters by dividing the variance of that physical parameter in the retrieval pdf by the *a priori* variance. The base-2 logarithm of this ratio can be thought of as the ‘bits’ of information present in the retrieval and is a common information content metric (L’Ecuyer et al., 2006). Using this metric, the information content of the rain LWP, cloud LWP, and IWP retrievals are given for each sample profile in table 3.5. In addition, since the information present in some measurements (*e.g.*, PIA) is strongly dependent on rainfall intensity, we performed this analysis for composite profiles in 5-dBZ bins (Figure 3.9). It is clear that the ability of the observations to resolve rain LWP and IWP increases with increasing rain intensity for all types. However, there is no similar trend for cloud water², although for profiles with a higher true ratio of cloud water to rain water, this would not be the case.

A similar exercise is performed to examine the sensitivity of the retrieval to ice water path (IWP) and snow/graupel partitioning. Only the deep convective and stratiform profiles are examined here since no ice is present in the shallow convective profile; however, reflectivities were increased by 10 dBZ for each profile in order to create a significant ice scattering signature. The 85V T_{bs} are contoured in IWP-graupel fraction space in Figure 3.10, with the lines enclosing the region defined by the default T_{bs}

² The values themselves depend upon the definition of S_a , so the fact that they are sometimes negative is meaningless.

Table 3.5: Information content (bits) of various physical parameters in composite profiles.

Parameter	Deep Convective	Shallow Convective	Stratiform
Rain LWP	5.3	3.81	3.81
Cloud LWP	-2.34	-2.99	-2.95
IWP	2.32		1.67

± 5 K. The most important feature of these plots is that, while T_b does vary with graupel fraction, a greater range can be achieved by altering the total IWP via ϵ_{ICE} . In some cases it may be necessary to adjust the graupel fraction to match the coldest observed T_b s, although this is not done in the current implementation.

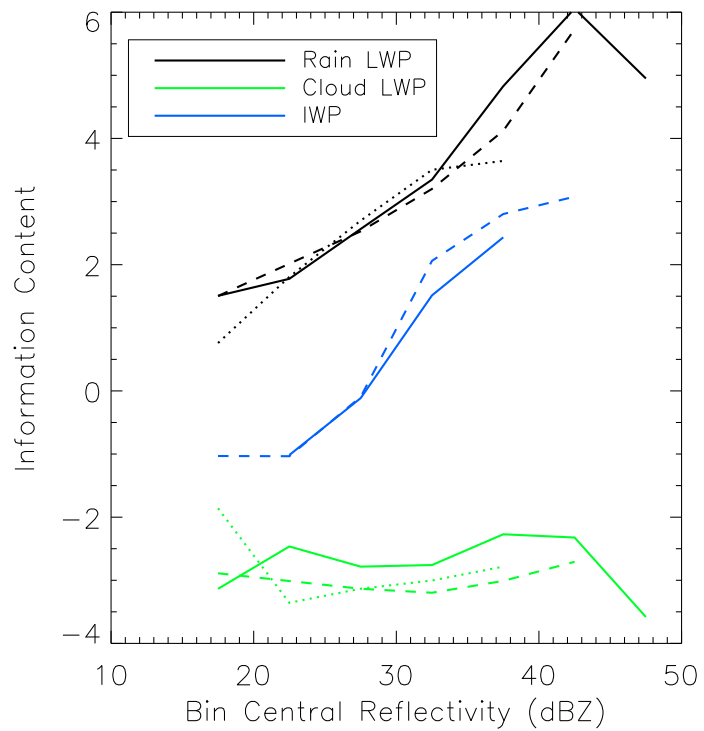


Figure 3.9: Information content for each retrieved variable and rain type (deep convective=solid,shallow convective=dotted,stratiform=dashed) as a function of reflectivity (5-dBZ bins).

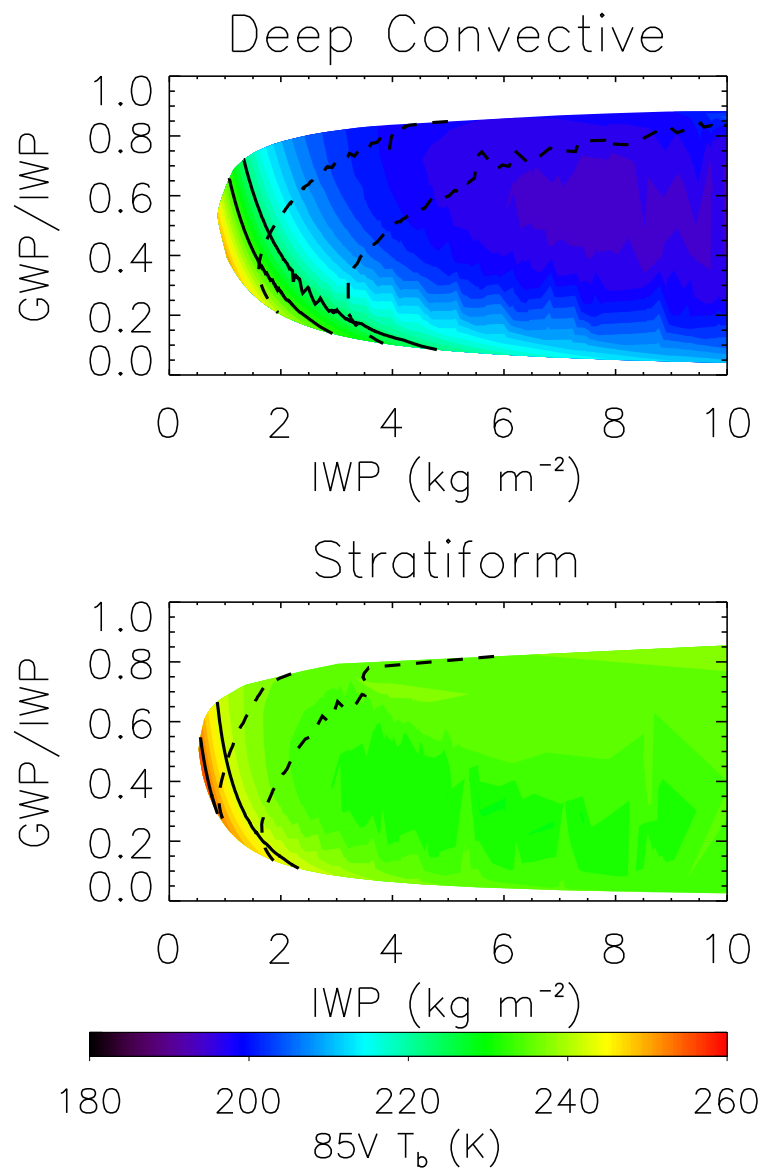


Figure 3.10: Contours of the *a priori* (dashed) and T_b (solid) constraints as a function of graupel fraction and total IWP, overlaid on 85V T_b s.

Chapter 4

ALGORITHM VALIDATION

The results of the optimal estimation components of the algorithm are verified in this chapter. First, the cloud/drizzle retrieval over non-raining pixels is compared to coincident VIRS-based cloud LWP retrievals. This is done both to illustrate the method of retrieving a high-resolution field from lower-resolution, overlapping TMI FOVs and to quantify its accuracy against a well-known independent method. Next, the combined retrieval algorithm is applied to TRMM datasets within 150 km of ground radars that are part of the TRMM Ground Validation (GV) network at Melbourne, FL, and Kwajalein, Republic of Marshall Islands (Wolff et al., 2005). These sites were selected because they represent differing precipitation regimes, significant coverage over ocean, and, in addition to the standard 2-km resolution rain map (GV product 2A53), disdrometer measurements and dual-polarimetric rainfall retrievals¹. The dual-pol data from Kwajalein is used to determine the cloud water/rain water partitioning via the uncertainty in ϵ_{CLW} , while Melbourne is used as an independent verification site. Finally, DSD statistics from ground-based disdrometers are compared to the retrievals in both locations.

4.1 Cloud and Drizzle In Non-Raining Pixels

The first retrieval module in the algorithm is used to retrieve the cloud + drizzle LWP outside of the raining pixels. This is done because of the three fields retrieved by the non-raining retrieval, cloud water is most inhomogeneous and most sensitive to partial beam filling effects (Rapp et al., 2009). Because of the size and overlap of the TMI FOVs, it is important to retrieve these fields as accurately as possible so that errors in the non-raining field are a minimal error source in computing the convolved T_b of an FOV

¹ Kwajalein only

that covers both raining and non-raining PR pixels.

To evaluate the retrieval of cloud water+drizzle in nonraining PR pixels, it is compared to the [Elsaesser and Kummerow \(2008\)](#) microwave retrieval and a VIRS-based retrieval using the method of [Nakajima and King \(1990\)](#) over one day of TRMM orbits. To obtain maximum accuracy of the VIRS retrieval, only rain-free scenes with a solar zenith angle of less than 70° were considered.

The results of the VIRS data were first used to determine the decorrelation length scale of cloud LWP. Values for scenes ranged between 7.9 and 193 km, with most between 10 and 40 km. Since the effect of including this length scale in the *a priori* covariance matrix is to smooth the field, a value of 10 km that is close to the lower bound yet is enough to effectively smooth the artifacts caused by the space between 85 GHz scan lines is used. The mean ratio of cLWP variance to the mean was 120%. Due to the wide range of this value from scene to scene, however, the retrieval was tested using *a priori* logarithmic variances representing 50%, 100%, and 300%.

An example scene is illustrated in [Figure 4.1](#). The improvement from the independent-FOV to whole-scene retrieval is clear, even though the same observations are used in each. The bulk statistics confirm and quantify this improvement. Regardless of the assumption regarding *a priori* variance, the correlation improved from the independent-FOV method ([Table 4.1](#)). The best results were obtained with an *a priori* variance of 100%. The overall bias increases going from the independent FOV to whole-scene method, however, a closer examination of the microwave vs. VIRS cloud LWP pdfs ([Figure 4.2](#)) shows why this is the case. Since the overall distribution of the water is skewed towards low values, the positive bias of both TMI-based retrievals dominates here. This bias is barely reduced in the whole-scene method, however, the low bias at higher VIRS LWPs is improved somewhat. Thus, the overall bias increases, although the results of the [Nakajima and King \(1990\)](#) technique become more sensitive to assumptions about the vertical distribution of cloud water at these high LWPs and should not necessarily be considered absolute truth. The inability of the microwave channels to retrieve cloud LWPs much lower than about 0.05 kg m^{-2} may be due to a combination of model biases and sensor calibration ([Elsaesser and Kummerow, 2008](#)). Although this error is significant in terms of non-raining cloud water statistics, the effect on the lower-frequency channels which are used to retrieve rain is minimal.

These results highlight the ability of the whole-scene retrieval to eliminate errors from partial

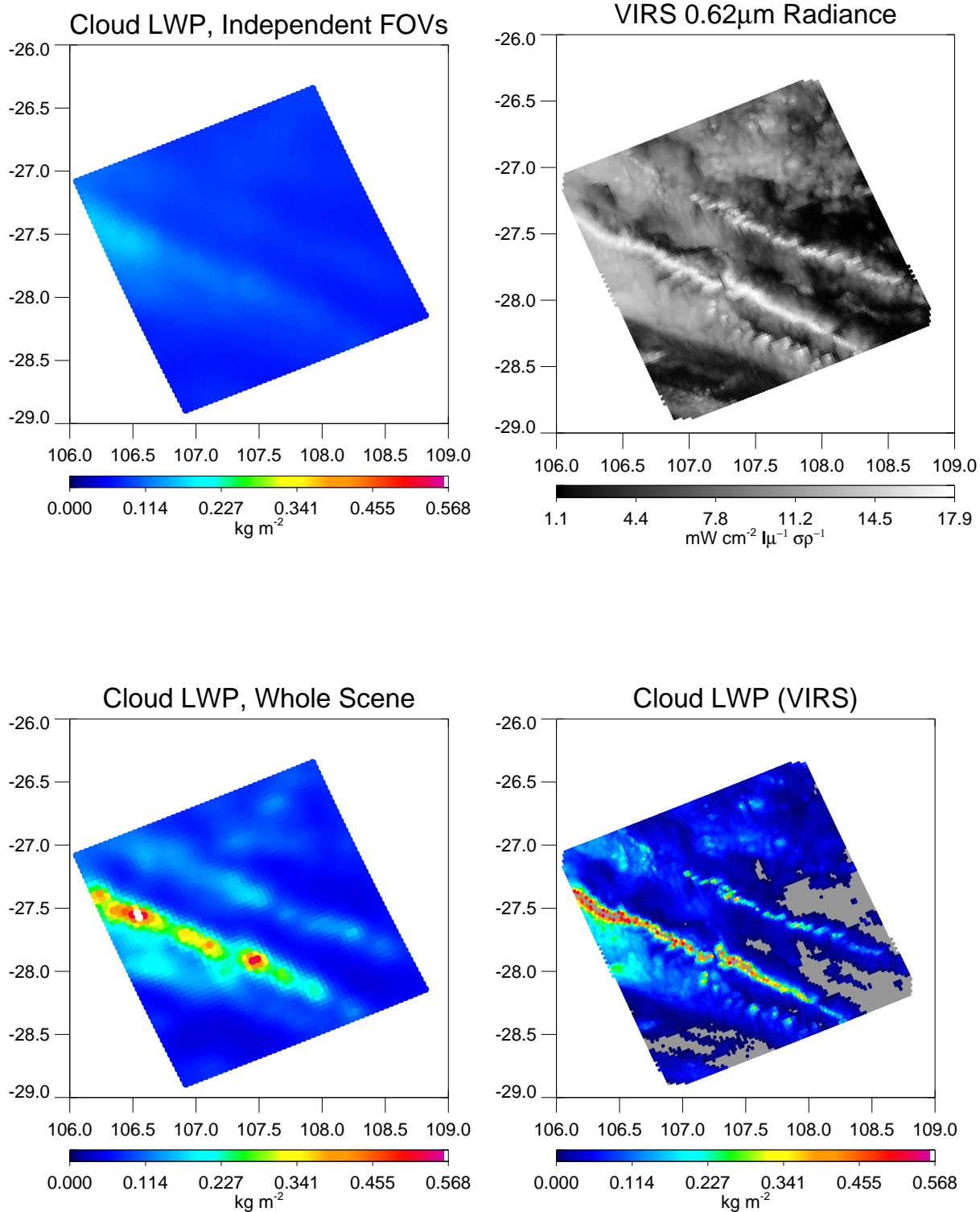


Figure 4.1: Cloud LWP retrievals for a sample scene on 1 Jan 2000. For reference, the visible-wavelength VIRS radiances are also shown.

Table 4.1: Correlation and bias between microwave- and VIRS-based cloud LWP retrievals.

Microwave Method	<i>a priori</i> variance	Correlation (r^2)	Bias
Independent FOV	172%	0.468	1.379
Whole Scene	50%	0.537	1.413
Whole Scene	100%	0.551	1.410
Whole Scene	300%	0.504	1.427

beam filling effects above the PR resolution, albeit at greater computational expense than deconvolution methods. There is still reduced resolution relative to VIRS, owing to its much smaller footprint relative to the 85 GHz channel on TMI and the PR-resolution grid on which the field is retrieved.

4.2 Kwajalein

The Kwajalein Ground Validation site, located on a small atoll in the central Pacific Ocean, is an ideal site to test the combined algorithm because of its oceanic location, where the radiometer has the potential to add the most information to the radar. Although GV rain products are available since 1998, only recently have calibration problems been addressed and dual-polarization capability added (Silberstein et al. (2008), Marks et al. (2009)). With these additional capabilities, a robust dataset of polarimetric rain retrievals has been developed by Wolff (2009; pers. comm.) using the method of Bringi et al. (2004). This dataset is used for two purposes: First, to constrain the free parameters in the retrieval, and second, for direct comparisons with the results of the combined retrieval algorithm.

A free parameter in the combined retrieval is the variance of ϵ_{CLW} , which determines the cloud water-rain water partitioning. The rain PDFs and CDFs (Figure 4.3) show that a reasonable range of uncertainty in ϵ_{CLW} provides estimates that are in line with those of the GV radar, with an optimal uncertainty of 100%. Higher values reduce the cost of changing ϵ_{CLW} , thus, the rain DSD is modified to a lesser extent; similarly, lower values constrain cloud water more strongly, and the rain DSD is modified more readily. The GV-tuned value results in a 10% increase of rainfall over 2A25, which is in line with the PR-GV bias at Kwajalein reported by Wolff and Fisher (2008). These PDFs also show the general agreement of 2A25 and the PIA-only profiling algorithm, the low rain bias of the default DSD in this region, and general agreement of all methods in heavy rain, where the SRT measurement of PIA is most

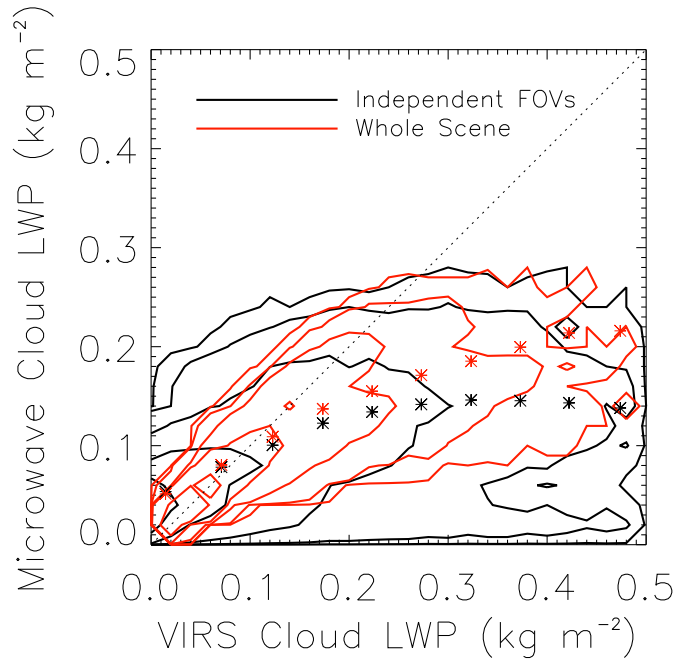


Figure 4.2: Contours of the 2D density function of cloud LWP retrieved by VIRS and both microwave-based methods. Contours represent 1,10,100,1000,and 10000 data points. The corresponding mean values, in 0.05 kg m^{-2} bins, are plotted with asterisks (*).

reliable.

To further compare the retrieval results to the GV radar data, profiles of reflectivity and D_0 are examined in Figure 4.4. These are grouped by SRT PIA, since profiles where SRT PIA is less than 4 dB are usually considered unreliable and the SRT value is not used to adjust the DSD. The combined retrieval results in a slight low bias in D_0 relative to the co-located GV and radar-only retrievals in light rain, but this may be a result of the low bias in reflectivity in these profiles, a possible consequence of the PR detection threshold. In the profiles with reliable PIA, D_0 is generally in better agreement with GV, especially relative to the default values. Reflectivity profiles also show better agreement, with the combined algorithm matching GV better than the default DSD and PIA-based methods.

An example case is shown in Figure 4.5. The top panels show a good match of the general reflectivity features despite the degradation of the PR resolution relative to the ground radar. In the lower panels, the Z-normalized D_0 is shown. The polarimetric radar shows relatively large drops in the

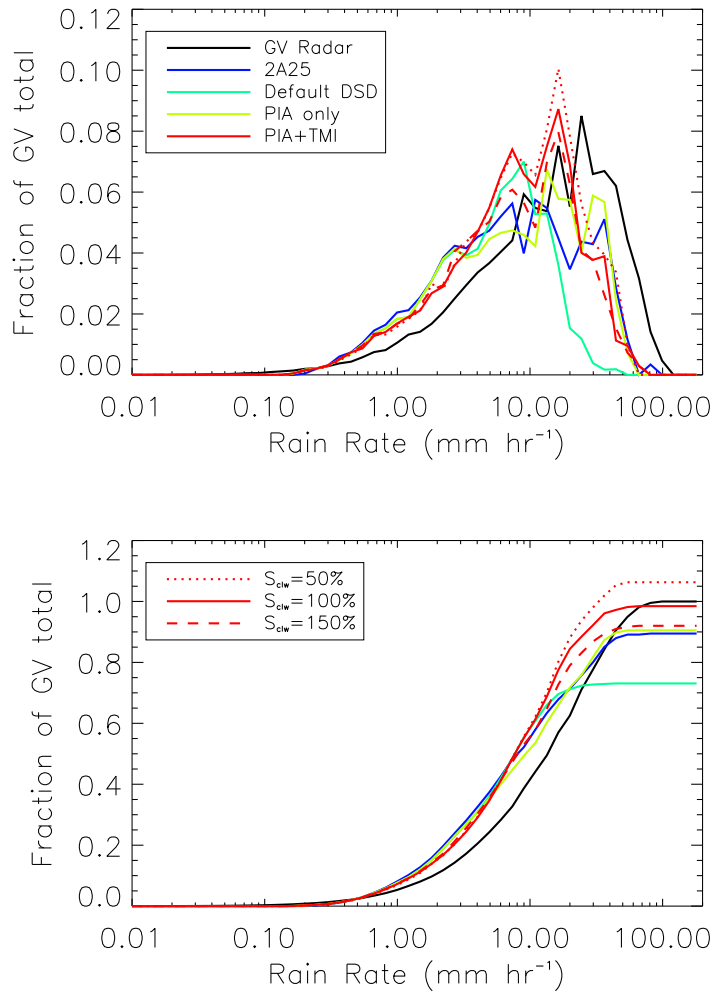


Figure 4.3: PDF (upper panel) and CDF (lower panel) of rainfall rates within 110 km of the Kwajalein GV radar site during May-November 2008. The legend in the top panel refers to the retrieval method; in the bottom panel, the PIA+TMI retrieval is further divided by cloud water sensitivity. The GV radar data was not degraded to PR resolution in this figure.

stratiform regions (inferred from the more homogeneous reflectivity field) north and south of the radar. To the east and southeast, there is a line of convection with relatively smaller drops. The combined retrieval captures the contrast between the southern stratiform region and the convection, but does not do as well with the northern stratiform region. There is convection embedded within the northern region which may dominate the radiometric signal, despite being a small fraction of the area. Despite this region having a low bias in D_0 , the mean rainrate is still less than the GV mean, although it represents a significant improvement from the PIA-only retrieval.

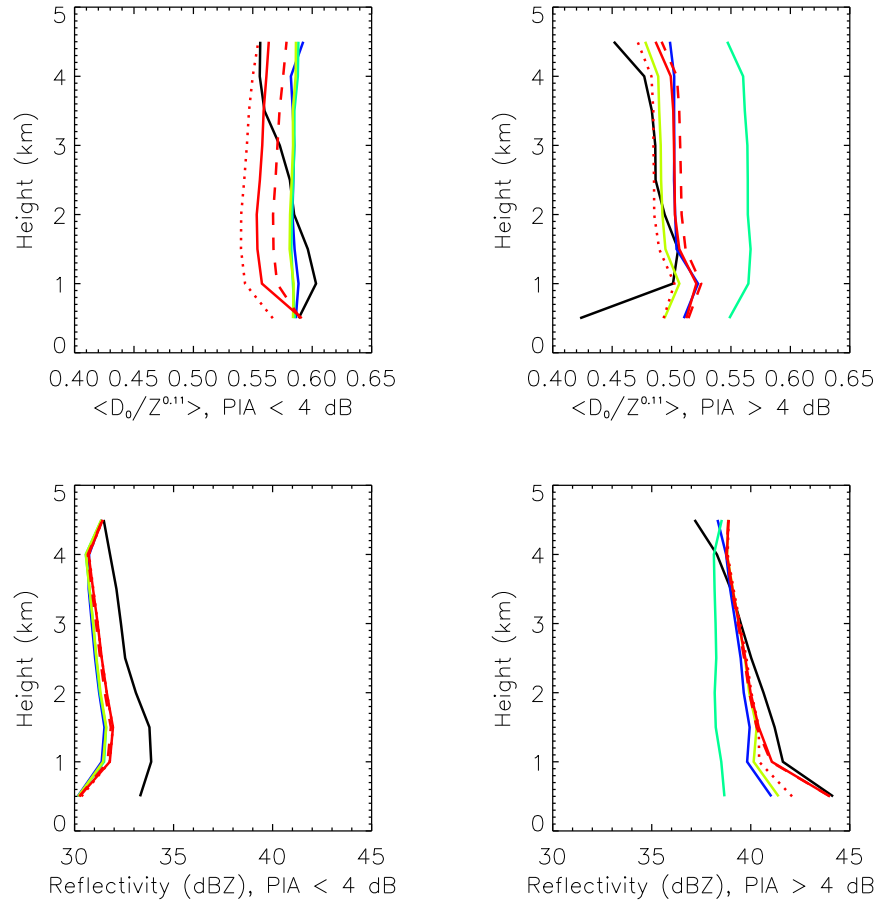


Figure 4.4: Mean profiles of normalized D_0 (upper panels) and reflectivity (lower panels) for PR pixels with (right) and without (left) reliable SRT PIA. Line style and color represent the same retrieval as in Figure 4.3. The GV radar data is degraded to PR resolution.

4.3 Melbourne, FL

An independent validation test was performed by comparing retrieval results to those from the standard 2A53 GV radar products over Melbourne, FL for the years 2006-2008. The mean rain rates from each retrieval are plotted in Figure 4.6. It is apparent that there is much month-to-month and year-to-year variability as to which retrieval method best matches the co-located GV totals. The GV $Z - R$ relationship is based on monthly gauge accumulations, whereas there are only 10-20 overpass events each month, with just a few of these dominating the total rainfall. Thus, the average rain DSD that determines the monthly $Z - R$ relationship may be quite different than that in the overpasses, especially considering the gauges are all on land whereas the retrievals compared here are all over the

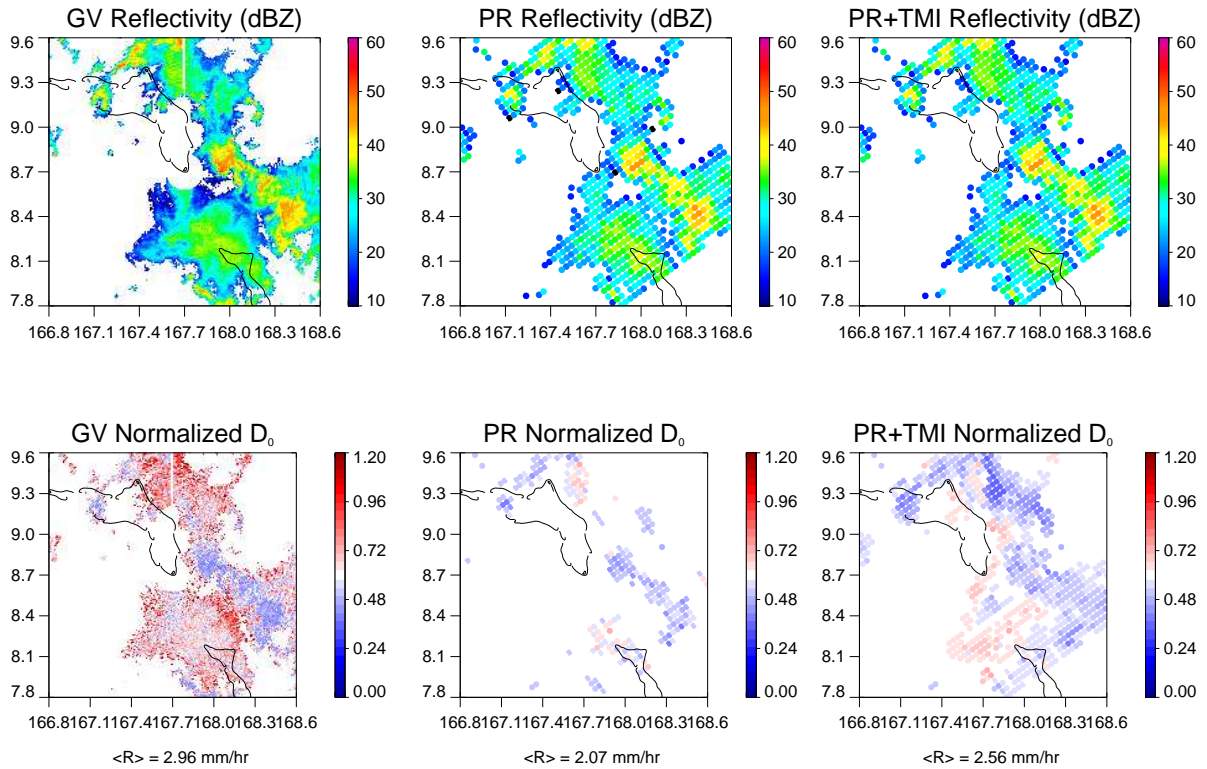


Figure 4.5: An example case from 1647 UTC on 26 October 2008 at 1.5km height. D_0 is normalized by $Z^{0.11}$ in the lower panels.

ocean. Nevertheless, the combined algorithm at the very least does no worse than the PIA-based radar algorithms in making adjustments from the default DSD. This is especially clear during Jan-Apr, when all algorithms reduce rainfall considerably relative to the default, implying larger drops as might be expected in the predominately frontal, stratiform rain that falls this time of year. During the summer and fall, when rainfall comes from a mixture of isolated convection and tropical cyclones, the departure from the default DSD is less clear and probably depends on the dominant source of rain during each month. The total accumulated rainfall from the combined algorithm is only 1.6% higher than GV, while 2A25 underestimates the GV total by 5% and the default DSD overestimates it by 14%. Thus, the combined method is able to match the Melbourne rainfall while also being unbiased at Kwajalein, where 2A25 underestimates GV significantly.

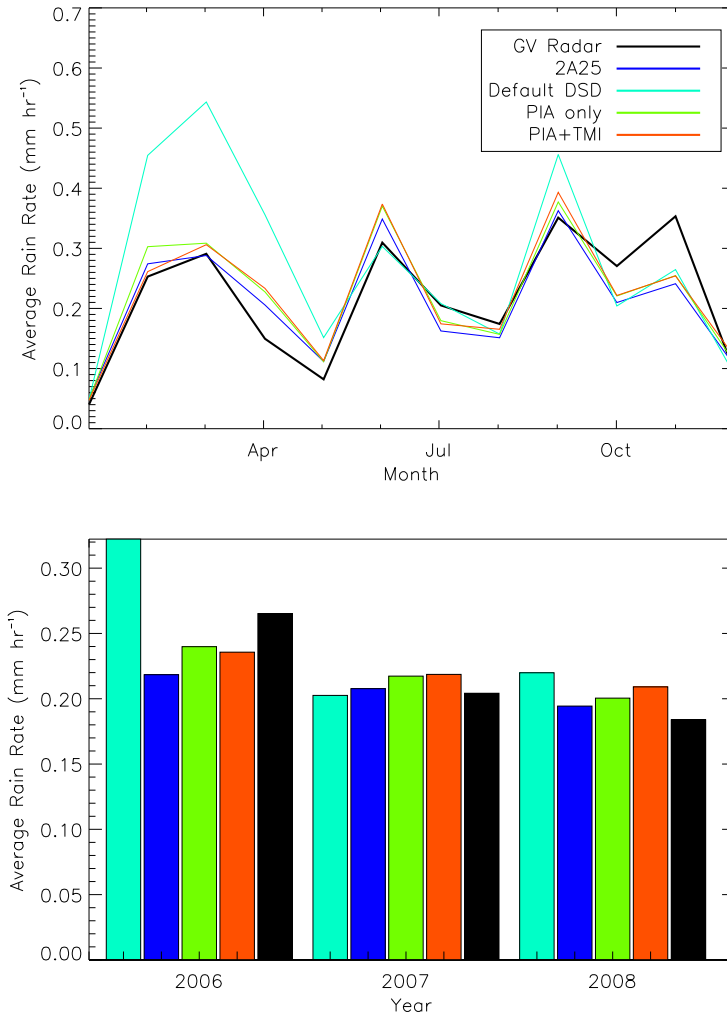


Figure 4.6: Monthly (top) and yearly (bottom) mean rain rates from different retrieval methods at Melbourne, FL.

4.4 Brightness Temperature Statistics

While agreement between the retrieved and observed brightness temperatures does not guarantee that correct DSD parameters are being retrieved, and cannot be considered validation in a strict sense, such internal consistency does indicate that the vertical model described in section 3.2 is adequate to explain the observed T_b s. Moreover, the degree to which simulated T_b s improve in the combined algorithm relative to a radar-only algorithm (such as 2A25) can also be considered a measure of the effectiveness of the retrieval.

Scatter plots of observed and simulated T_b s are shown in Figure 4.7. At the lower-frequency

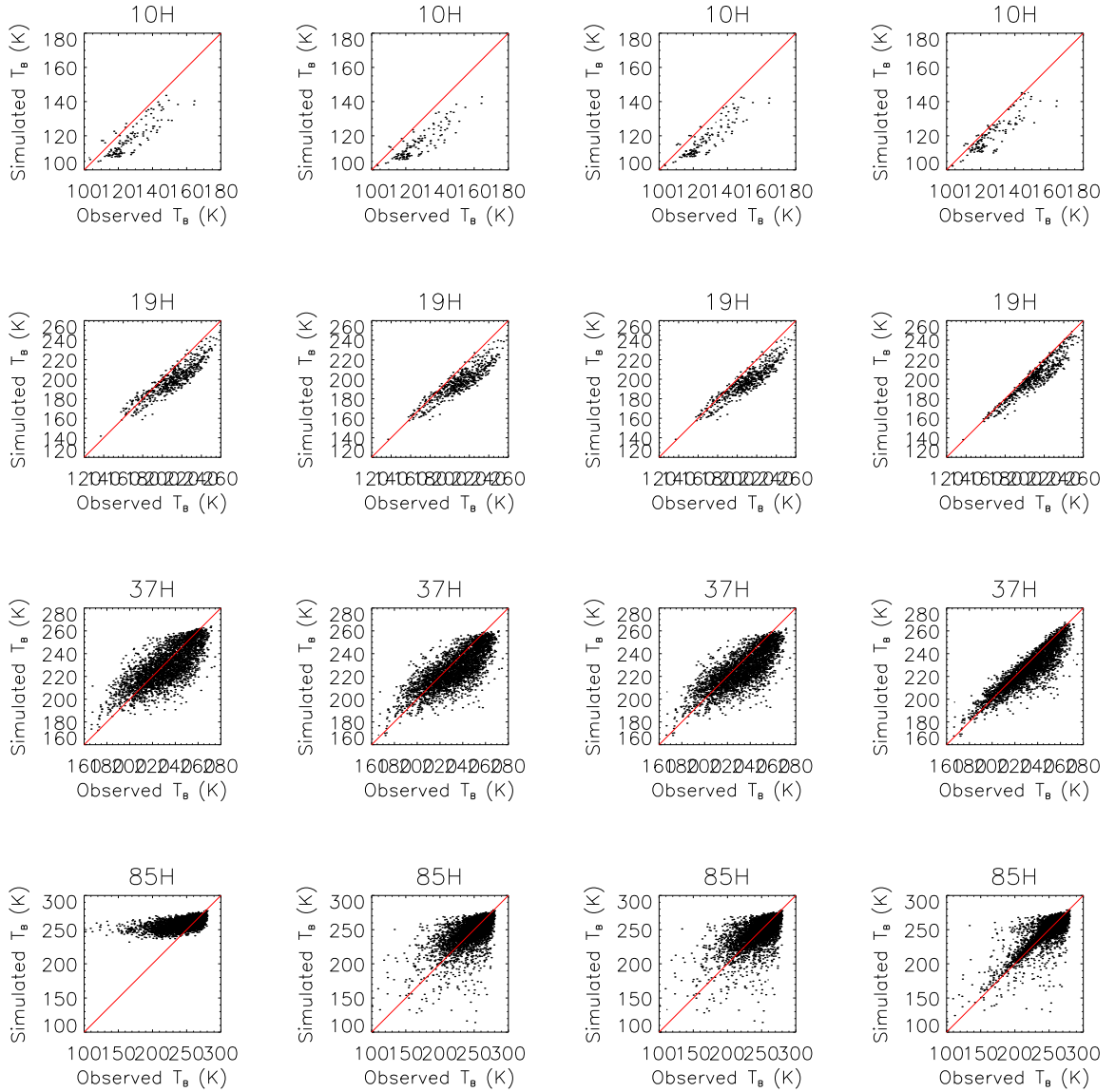


Figure 4.7: Scatter plots of simulated versus observed brightness temperature for selected TMI channels and four retrieval methods: First column- 2A25; Second column - Default DSD, Third column - PIA only OE, Fourth column - Combined OE. In order to minimize the influence of errors in the non-precipitation parameters, only TMI FOVs with at least 30% rain coverage are included. These data come from the Kwajalein and Melbourne validation regions described in sections 4.2 and 4.3, respectively. Due to major differences in the ice parameterization between 2A25 and the combined algorithm, simulated 85 GHz T_b s for 2A25 should be ignored.

channels it appears that a slight cold bias is evident in the default DSD and PIA-adjusted products (both 2A25 and the PIA-only version of the combined retrieval), particularly at 10 GHz. These biases are improved, but still exist to a slight degree in the combined product. Meanwhile, the fairly large scatter in

Table 4.2: Brightness Temperature RMS error and bias (simulated minus observed) for FOVs with at least 30% rain coverage.

Channel	RMS (K)				Bias (K)			
	2A25	Default	PIA-only	PIA+TMI	2A25	Default	PIA-only	PIA+TMI
10V	6.52	7.90	6.69	4.83	-5.70	-7.22	-6.04	-3.85
10H	10.58	12.91	10.72	7.98	-8.70	-11.46	-9.18	-5.60
19V	8.08	9.30	8.59	6.30	-6.29	-7.76	-7.16	-4.93
19H	14.17	16.12	14.85	10.89	-10.84	-13.28	-12.22	-8.37
37V	7.19	8.02	7.94	5.97	-0.77	-3.59	-3.50	-2.92
37H	13.34	13.85	13.75	9.98	-2.54	-5.91	-5.77	-4.96
85V	18.82	16.36	16.38	12.56	6.50	-2.15	-2.29	-2.83
85H	20.88	16.46	16.45	12.28	10.00	1.26	1.13	0.62
PIA (dB)	1.21	1.89	1.28	1.24	-0.38	-0.41	-0.36	-0.33

the T_{bS} simulated by the radar products at 37 GHz and 85 GHz is reduced significantly in the combined retrieval.

Quantitative measures of these errors are presented in Table 4.2. The largest errors and biases occur when no adjustments from the default DSD are made. When adjustments are made in heavy rain to match the PIA, errors are reduced slightly, by about 1 K, on average in the T_{bS} and by about 0.6 dB in the PIA. A further reduction in the T_b errors is seen with the combined algorithm but biases and RMS errors are only reduced by about one-third to one-half of the default values, approaching the expected errors defined in the S_y covariance matrix. It is notable that the reduction in T_b errors has occurred without increasing the PIA errors from the radar-only algorithm. The residual RMS errors are a consequence of the OE methodology, which does not give a high value to matching observations better than the *a priori* error. However, the residual biases remain significant, particularly in the emission channels. Analysis of regional patterns of these biases is presented in Appendix B.

4.5 Disdrometer comparisons

As a final reference point, the retrieved DSDs are compared to ground based disdrometer measurements. Because the disdrometer represents a point measurement and the number of TRMM overpasses during rain events would yield an extremely small sample size, it is more meaningful to compare

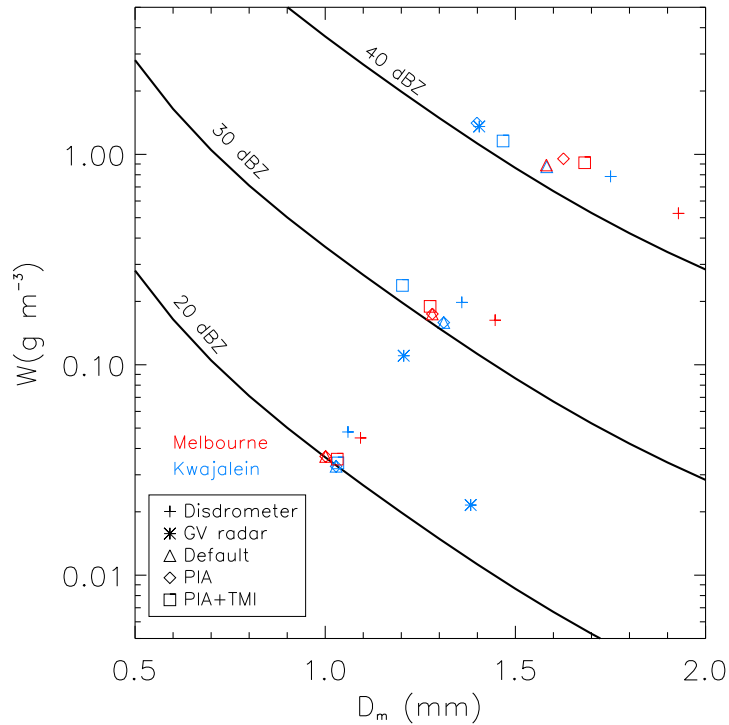


Figure 4.8: Mean liquid water content W versus mean mass diameter D_m from TRMM algorithms and ground instruments at Kwajalein and Melbourne at 20, 30 and 40 dBZ reflectivity. The solid lines represent the theoretical relationship between W and D_m at the given reflectivity assuming a gamma distribution with $\mu = 3$.

summary statistics than attempt to co-locate TRMM overpasses with the GV radar and disdrometer. Disdrometer data from Kwajalein are available from 2003-2004, and Melbourne, FL from 2006-2009. Although the former do not overlap the TRMM observations that were processed, the lack of a significant interannual change in DSD at Kwajalein (Kozu et al., 2009) should not prevent a statistical comparison.

Following Rosenfeld and Ulbrich (2003), liquid water content is plotted as a function of drop diameter in Figure 4.8 for reflectivities representing light (20 dBZ), moderate (30 dBZ), and heavy (40 dBZ) rain. Due to errors introduced by calculating D_0 from binned disdrometer data, the mass-weighted mean diameter D_m is used instead. For a gamma distribution, assumed in both ground radar and PR retrievals, $D_m = (4 + \mu)/(3.67 + \mu)D_0$. Deviations along the lines of constant reflectivity represent changes in the DSD, going from maritime to continental as D_m increases. Deviations perpendicular to these lines represent deviations in shape parameter or from the gamma distribution itself, in

the case of disdrometer data.

There is a relatively tight clustering of the DSDs derived from the TRMM data at low reflectivities that diverges as Z increases. This represents the increase in information (stronger PIA response) at higher rainrates that leads to a change from the default DSD. Curiously, the disdrometer data also show this divergence, despite the lack of any *a priori* assumptions in that dataset. There is also a clear increase in D_m and the decrease in W from Kwajalein to Melbourne, particularly evident in the disdrometer data, and both radar and combined retrievals. There is an apparent offset of the disdrometer data towards larger drop sizes, which was also noted by [Kozu et al. \(2009\)](#) in the Kwajalein dataset, where it was suggested that noisy conditions may have contributed to an undercounting of small drops. Notwithstanding this offset, the change in D_m from Kwajalein to Melbourne is nearly identical between the combined algorithm and disdrometer at all reflectivities. This ability of the combined algorithm to distinguish DSDs is particularly evident in moderate rain where PIA-only retrievals such as 2A25 must rely on default DSD assumptions. Even the polarimetric radar algorithm ([Bringi et al., 2004](#)) relies upon an assumed DSD in the lightest rain, although the small contribution of these rain rates to the total should not impact the cloud water constraint that was derived from the Kwajalein GV radar dataset.

Chapter 5

REGIONAL AND GLOBAL PROPERTIES OF THE RAINDROP SIZE DISTRIBUTION INFERRED FROM THE COMBINED ALGORITHM

In this chapter the results of the combined radar-radiometer algorithm applied to two years of TRMM data are analyzed to expand upon previous studies of global DSD patterns and to explore the relationship between the DSD and environmental, dynamical, and microphysical factors. An introduction towards current issues in DSD research is presented in section 5.1. In section 5.2, a database containing these retrieval results and ancillary data used to describe the environment associated with a given profile is described. Their influence upon the DSD is described in section 5.3. In section 5.4, the relationship between DSD and structures in the radar reflectivity profile is examined and show that this is consistent with ground-based radar observations. In section 5.5, the regional and seasonal patterns of all factors that are associated with the rain DSD are examined and it is shown that these patterns are consistent with the TMI/PR bias patterns in Berg et al. (2006) and the DSD map of Kozu et al. (2009).

5.1 Introduction

The raindrop size distribution (DSD) is a fundamental quantity in radar meteorology and other remote sensing applications and has been the subject of hundreds, if not thousands of studies including direct measurements (*e.g.*, Marshall and Palmer (1948), Waldvogel (1974), Tokay and Short (1996)), remote measurements (*e.g.*, Williams et al. (1995), Bringi et al. (2003)), parameterizations (*e.g.*, Ulbrich (1983), Haddad et al. (1996), Testud et al. (2001)), and numerical simulations (*e.g.*, List et al. (1987), Brown (1989), Hu and Srivastava (1995)). Various moments of the DSD describe physical quantities, such as the liquid water content W , rain rate R and median volume diameter D_0 , as well as quantities important for microwave remote sensing such as radar reflectivity Z and specific attenuation k . Relation-

ships between the physical and remotely-sensed quantities are often sought, particularly the reflectivity-rain rate ($Z - R$) relationship, which is frequently parametrized as the power law $Z = aR^b$. It has been known almost since the beginning of radar meteorology (Atlas and Chmela, 1957) that a single unique $Z - R$ relationship does not exist and instead, local relationships were often derived over long periods of time in order to provide radar rainfall estimates that were reasonable on seasonal and yearly scales at a given location (Battan, 1973).

With the advent of multi-parameter radars and their widespread deployment in the near future, the use of specific $Z - R$ relationships to estimate rainfall is becoming unnecessary as the additional measurements at horizontal and vertical polarization (Bringi and Chandrasekhar, 2001) or multiple frequencies (Keeler et al., 1989) provide additional information about the DSD, increasing the accuracy of instantaneous rain rate estimates. Nevertheless, the variability of reported $Z - R$ relationships, both between different locations and at the same location at different times, provides some insight into the variability of the microphysical processes that shape the DSD. These processes were summarized by Rosenfeld and Ulbrich (2003), who classified DSDs by dynamics (convective vs. stratiform) and microphysics (continental vs. maritime). Stratiform and continental DSDs are characterized by large D_0 for a given liquid water content, W , whereas convective and maritime DSDs of the same W have smaller drops (and lower Z). Although the names “continental” and “maritime” suggest that the proximity to the ocean is the primary driver of cloud microphysics, these designations do not reveal the mechanism(s) behind the differences between the two ends of the continuum. In fact, a number of factors are known to influence the DSD, and need not always dominate in the expected locations. For example, maritime DSDs have been observed over land (e.g., Fujiwara and Yanase (1968), Carey et al. (2001), Bringi et al. (2003)) and continental DSDs have been measured in tropical oceanic locations such as the Florida Keys (Tokay et al., 2003). Therefore, it is useful to briefly review the processes that are known to influence the rain DSD.

The formation of rain is typically classified microphysically as either a warm or cold process. Warm rain processes include the collision and coalescence of cloud droplets to a critical size and the collection of additional cloud droplets during fall. Eventually, the largest drops break up due to hydrodynamic instability. Various models (List et al. (1987), Hu and Srivastava (1995)) have shown the

collision-coalescence and breakup processes to result in an equilibrium shape to the DSD regardless of overall concentration which acts as a scaling factor. This equilibrium may be closely approximated by a gamma distribution with $D_0 = 1.76$ mm and $\mu = 9$, although [Prat and Barros \(2007\)](#) demonstrate that the shape of the equilibrium DSD is highly dependent upon the breakup parameterization kernel. However, this has only been observed in deep tropical convection ([Atlas and Ulbrich \(2000\)](#), [Munchak and Tokay \(2008\)](#)), as most rain that originates in weaker, shallower systems has not had enough fall time to achieve equilibrium. Cold rain formation occurs when rain results from the melting of frozen hydrometeors such as snow, graupel, or hail. These frozen particles, being much larger than the cloud droplets out of which warm rain forms, create correspondingly larger rain drops. As these fall, they too are subject to breakup which will push the DSD towards equilibrium, although the extent to which this occurs depends on the depth of the above-freezing layer.

Cloud dynamics influences the relative importance of warm and cold processes via updraft strength and structure. Convective rain can contain a mixture of warm and cold microphysics; cold microphysics becomes more important with stronger updrafts and cloud tops that reach above the freezing level. Stratiform rain, meanwhile, forms exclusively via cold processes by definition. Besides formation and internal processes, external processes such as evaporation and size sorting can also influence the DSD. Evaporation preferentially acts on small drops, thereby increasing the mean drop size, whereas the influence of size sorting by wind shear and turbulence is more complicated and its overall effect is unknown.

Considering all of the above processes, one would expect DSDs with smaller drops for a given Z in environments where warm rain processes are predominant and with deep, humid above-freezing layers. Meanwhile, larger drops would be expected in drier locations with a preference for deeper convection and/or more stratiform rain. Although these expectations qualitatively match observed DSDs, the relative influence of environmental and dynamical effects is still rather uncertain. In particular, the effects of aerosol loading are not well quantified, with data suggesting both suppression ([Rosenfeld, 2000](#)) and enhancement ([van den Heever et al., 2006](#)) of rainfall with increasing aerosol burden, depending on the aerosol properties and interaction between cloud microphysics and dynamics ([Givati and Rosenfeld, 2005](#)). These are also expected to affect the DSD via changing the relative importance of warm and cold rain formation processes.

Improved understanding of the relative importance of environmental, dynamical, and microphysical effects on the rain DSD can also benefit global satellite-based estimates of rainfall, which still rely on DSD assumptions to varying degrees, depending on the instrument. Microwave radiometer-derived estimates, available on a number of satellite platforms are physically tied to the emission signal (over ocean), which is roughly proportional to column-integrated W . The relationship between W and R is not as variable as the $Z - R$ relationship¹, but uncertainties in this relationship can still cause errors of as much as 10% (Wilheit et al., 2007) in R . Spaceborne radar-based estimates from the TRMM (Kummerow et al., 1998) precipitation radar (PR) rely on a set of default $Z - R$ relationships (Iguchi et al., 2000) that are modified to match the attenuation inferred by the apparent decrease in the surface reflection in heavy rain (Meneghini et al., 2000). Given the noise inherent in rain-free estimates of the surface cross section, this method is only reliable in rain rates exceeding approximately 10 mm hr^{-1} , and, in lighter rain, the default Z-R relationship must be assumed. Rain estimates from CloudSat (Stephens et al., 2002), which uses a higher frequency (94 GHz) that is subject to far greater attenuation than the TRMM PR, use the surface reference technique exclusively, disregarding the reflectivity information (Haynes et al., 2009), although a DSD is still implied in the $k - R$ relationship.

The reliance of each method upon DSD assumptions both introduces an element of uncertainty in the rainfall estimates and hinders the efficacy of the retrieval results to globally measure DSD properties. Indeed, Berg et al. (2006) suggest DSD variability as one possible mechanism for biases between the radar- and radiometer-(TMI) based rainfall estimates from the TRMM satellite. Global maps of DSD derived from 10 years of TRMM PR retrievals were presented by Kozi et al. (2009); however, these were limited to profiles classified as convective rain, since insufficient information is present to retrieve the DSD in weaker stratiform rain. Nevertheless, and perhaps owing to the fact that despite representing a small fraction of rain occurrence at any given location, convective rain accounts for a significant portion of total rainfall, the global patterns of DSD bear some resemblance to the PR-TMI differences. Areas where TMI estimates exceed PR estimates tend to have smaller values of a (corresponding to smaller mean drop sizes at a given reflectivity) and vice-versa. This suggests that either the PR is making an

¹ Recall from chapter 2 that R is approximately proportional to the 3.67th moment of the DSD, whereas Z is to the 6th and W is to the 3rd.

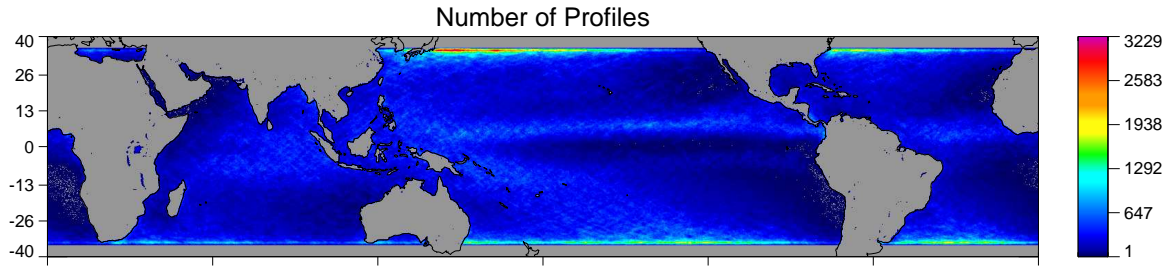


Figure 5.1: Number of profiles in 0.25×0.25 degree grid boxes.

adjustment to its default DSD in the right direction but of insufficient magnitude, or that the DSD implied in the TMI retrieval is somehow biased. The latter argument is supported by the fact that, of two DSDs with identical W but different D_0 , R will be greater for the one with the larger D_0 since larger drops fall faster.

5.2 Database Construction

Two years of TRMM data were processed with the combined algorithm, one representing the pre-orbit-boost period (August 1999-July 2000) and one representing the post-boost period (January-December 2006). In order to speed computations and avoid biases associated with ground clutter ([Shimizu et al., 2009](#)), only the central 25 PR angle bins were processed. Due to difficulties in estimating surface emissivities (a necessary component of the combined algorithm) over land, only over-ocean retrievals were considered in this analysis. These two years provided 75,639,452 precipitation profiles spatially distributed as shown in Figure 5.1.

In order to determine the effect of variables related to the background environment, storm structure, and microphysics on the retrieved DSD, each profile was associated with the variables listed in Table 5.1. Many, but not all, of these variables come from products derived from various instruments on board the TRMM satellite, ensuring coincidence in time and space. Storm echo top and maximum reflectivities near the surface and in the rain, mixed, and ice layers are taken from the attenuation-corrected reflectivity profile provided by the combined algorithm. The freezing height is derived from interpolated estimates of the top of the radar bright band. The strength of the bright band is used to determine the density of the melting particles as described in section 3.2 and [Zawadzki et al. \(2005\)](#). The local variability of rain

rate is simply the standard deviation of near-surface rain rate within 5 PR pixels (the 2A25 rain rate was used here in order to obtain values outside the central 25).

The combined algorithm provides the cloud and rain liquid water path, near-surface rain rate, and D_0 in addition to the parameters describing the rain DSD and ice PSD (ϵ_{DSD} and ϵ_{ICE}). The information content in the optimal estimation retrieval is given by the A-matrix statistic (Rodgers, 2000, Eq. 3.5), with higher values indicating an adjustment was made in accordance with the SRT PIA and T_{bs} . To indicate the relative contribution of these observations, Figure 5.2 shows the distribution of information content for retrievals performed using the SRT PIA only (similar to 2A25) along with the full combined algorithm. The PIA-only retrieval only adjusts about 10% of pixels, but these comprise 50% of total rain owing to the fact that the SRT is most reliable in heavy rain. The radiometer T_{bs} do not increase the number of pixels with high information content, due to the relatively lower resolution of the TMI channels, but do increase the number with some information, such that now 80% of pixels, representing 90% of rainfall, have been adjusted from the default DSD to match the TMI T_{bs} . The spatial distribution of different levels of information content is also shown in the lower three panels of Figure 5.3.

Background parameters total precipitable water (TPW) and sea surface temperature (SST) were derived from TMI data using the methods of Elsaesser and Kummerow (2008) and Gentemann et al. (2004), respectively. Note that these represent the nearest value outside of the raining area. The $12 \mu\text{m}$ channel on the TRMM VIRS instrument (Kummerow et al., 1998) was used to determine the cloud top temperature. Column relative humidity was calculated by dividing the retrieved TPW by the saturated TPW derived from a temperature profile consistent with the SST and freezing level.

A number of variables related to cloud microphysics are included. The cloud top effective radius (R_e) is retrieved from the VIRS data using the method of Nakajima and King (1990). The depth of the column where R_e exceeds $15 \mu\text{m}$ is also used as a variable to indicate the presence of warm rain processes as suggested by Rosenfeld and Lensky (1998). Since the visible-infrared retrieval technique only works during the daytime, daily and monthly composites of these variables were constructed and used where coincident data were unavailable. Finally, the SPRINTARS (Takemura et al., 2000) aerosol optical depth (AOD) reanalysis was included as an additional microphysics variable.

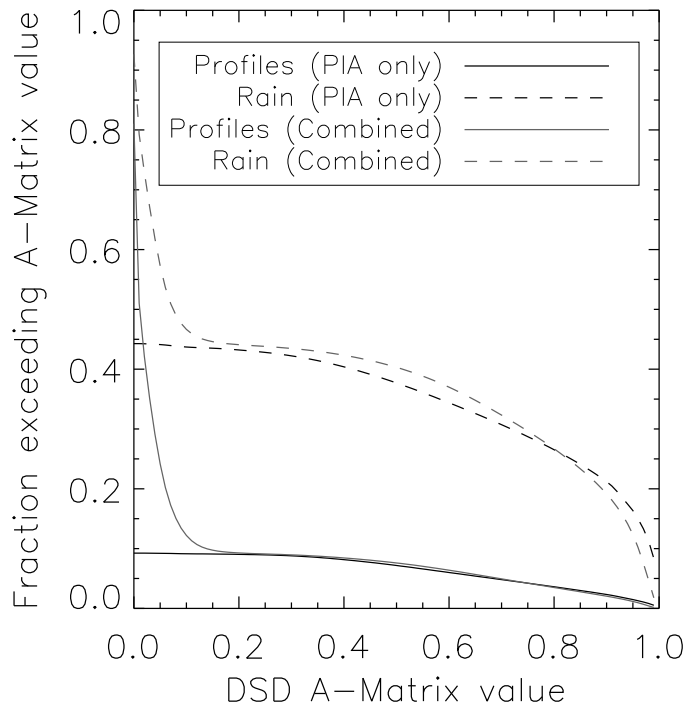


Figure 5.2: Distribution of profiles (solid) and rainfall (dashed) by information content for radar-only and combined algorithms.

5.3 Sources of DSD variability

In this section, correlations of DSD variability (represented by ϵ_{DSD} and D_0) with the various parameters listed in Table 5.1 are examined individually and in pairs. For this analysis, only profiles with an A-matrix value exceeding 0.01 were selected in order to balance having adequate information content in the retrieval while including profiles representative of weak and isolated rain, which are eliminated when a higher threshold is used.

Density contours with the mean value overlaid are shown in Figures 5.4 and 5.5 for D_0 and ϵ_{DSD} , respectively. Looking first at D_0 , it is most strongly correlated with reflectivity at various points throughout the profile. This is not surprising since a power law relationship between Z and D_0 has been prescribed; however, the variations about the mean show that significant adjustments have been made in many of the profiles. The next strongest correlations are associated with echo top, melt density, cloud LWP, and rain rate, all of which generally indicate that, to first order, heavier rain tends to contain larger

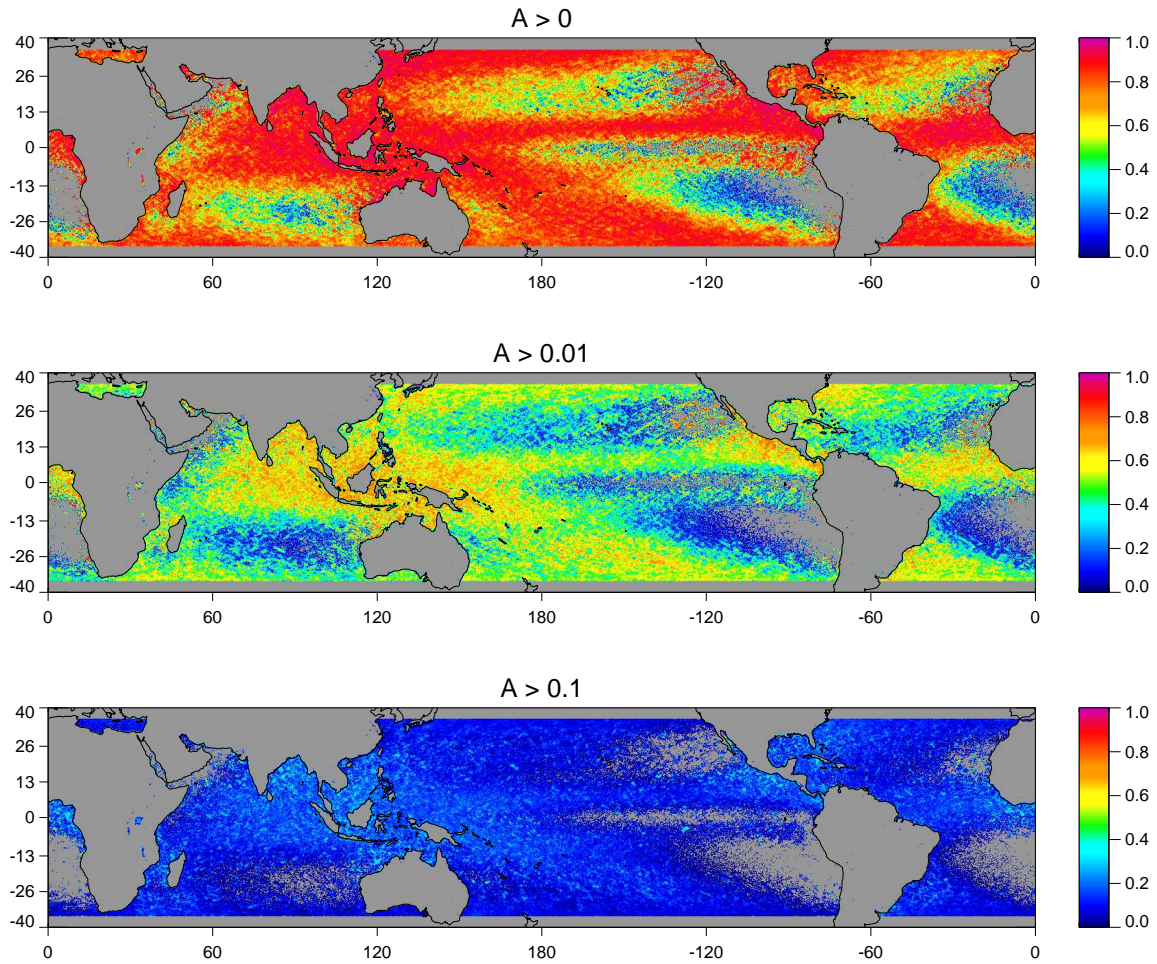


Figure 5.3: Fraction of profiles in each grid box that exceed the threshold of information content indicated.

drops. There are also significant negative correlations with environmental factors such as freezing level, SST, TPW, and column RH.

The correlations with ϵ_{DSD} , which can be thought of as a reflectivity-normalized D_0 , show different tendencies. Correlations with environmental parameters all show decreasing ϵ_{DSD} in more “tropical” environments (higher SST, water vapor, freezing height), in line with the expectation that warm rain processes should be more dominant under these conditions. Similarly, dryer environments (indicated by lower column RH) are associated with larger drops at a given reflectivity, as expected due to evaporation. Correlations with observables related to convective/stratiform separation, that is, melt density and

Table 5.1: List of profile database variables and sources.

Variable	Source
Total Precipitable Water	TMI
Sea Surface Temperature	TMI
Column Relative Humidity	TMI+PR
Cloud Liquid Water Path	TMI+PR
Rain Liquid Water Path	TMI+PR
Freezing Level	PR
Melt Density	PR
Echo Top Height	PR
Cloud Top Temperature	VIRS
ϵ_{DSD}	TMI+PR
A_{DSD}	TMI+PR
ϵ_{ICE}	TMI+PR
A_{ICE}	TMI+PR
ϵ_{CLW}	TMI+PR
Rain Rate Variability	PR
Maximum dBZ in rain layer	PR
Maximum dBZ in melting layer	PR
Maximum dBZ in ice layer	PR
Near-surface dBZ	PR
Near-surface rain rate	PR+TMI
Near-surface D_0	PR+TMI
Mean cloud effective radius	VIRS
Warm Rain Depth	VIRS
Aerosol Optical Depth	SPRINTARS

rain spatial variability, show the expected behavior, with smaller ϵ_{DSD} drops present with weaker bright bands and higher rain rate variability, despite absolute drop size (figure 5.4) increasing with these variables. There are only weak correlations with cloud microphysical parameters (mean R_e of nearby warm clouds, warm rain depth, AOD). A more direct indicator of microphysical processes, perhaps, is the negative correlation with ϵ_{ICE} , which indicates that profiles with more scattering tend to have larger drops at a given reflectivity, perhaps a result of more dominant cold rain processes. This is also supported by weakly positive correlations of ϵ_{DSD} with reflectivity in and above the melting layer, but negative correlations below this level. Finally, it is worth noting that ϵ_{DSD} tends to decrease with parameters associated with rainfall intensity (LWP and rain rate). Although this might be a reflection of the fact that the most intense rain is in those profiles where an adjustment towards smaller D_0 has been made, it may also be

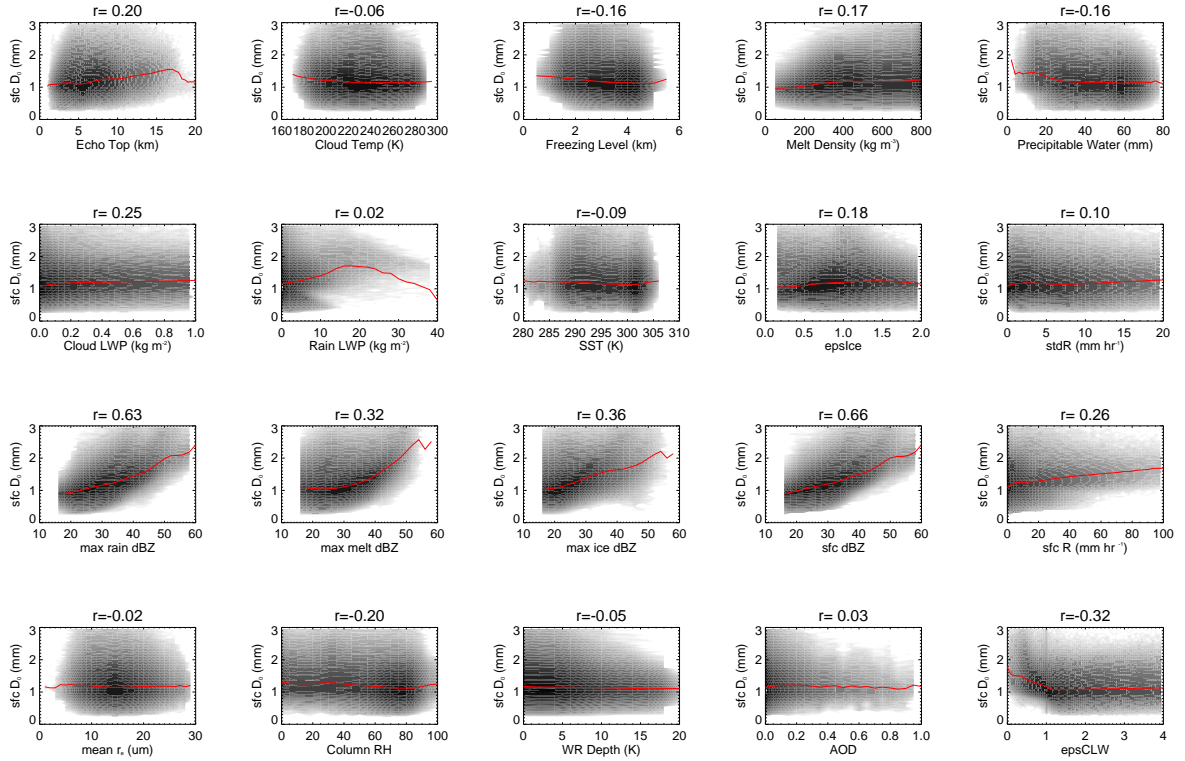


Figure 5.4: Correlation of near-surface median drop size D_0 with the variables in Table 5.1. Density contours are shaded at logarithmic intervals with mean values overlaid in red.

indicative of equilibrium DSDs being achieved in these heavy rain shafts.

In order to test the hypotheses in section 5.1 and further examine relationships between the DSD and variables that are correlated with each other (*e.g.*, TPW and SST), sets of two variables were selected for further analysis. The influence of warm vs. cold rain formation processes on the DSD is shown in figure 5.6 where contours of ϵ_{DSD} and D_0 are shown as a function of echo top and freezing height. Mean values of D_0 increase with echo top height, both above and below the freezing level. In both warm and cold rain this can be attributed to the increased path through which hydrometeors can grow and collect other particles as they fall. Relative to reflectivity, however, the strongest dependence is on the height of the freezing level, with larger drops favored for those profiles with lower freezing levels, even if the echo top does not extend above that level. Interestingly, there is a decrease in drop size as echo tops reach just above the freezing level. This is actually consistent with the conceptual models of warm and cold raindrop growth, where a drop that begins growing below the freezing level will have twice the path

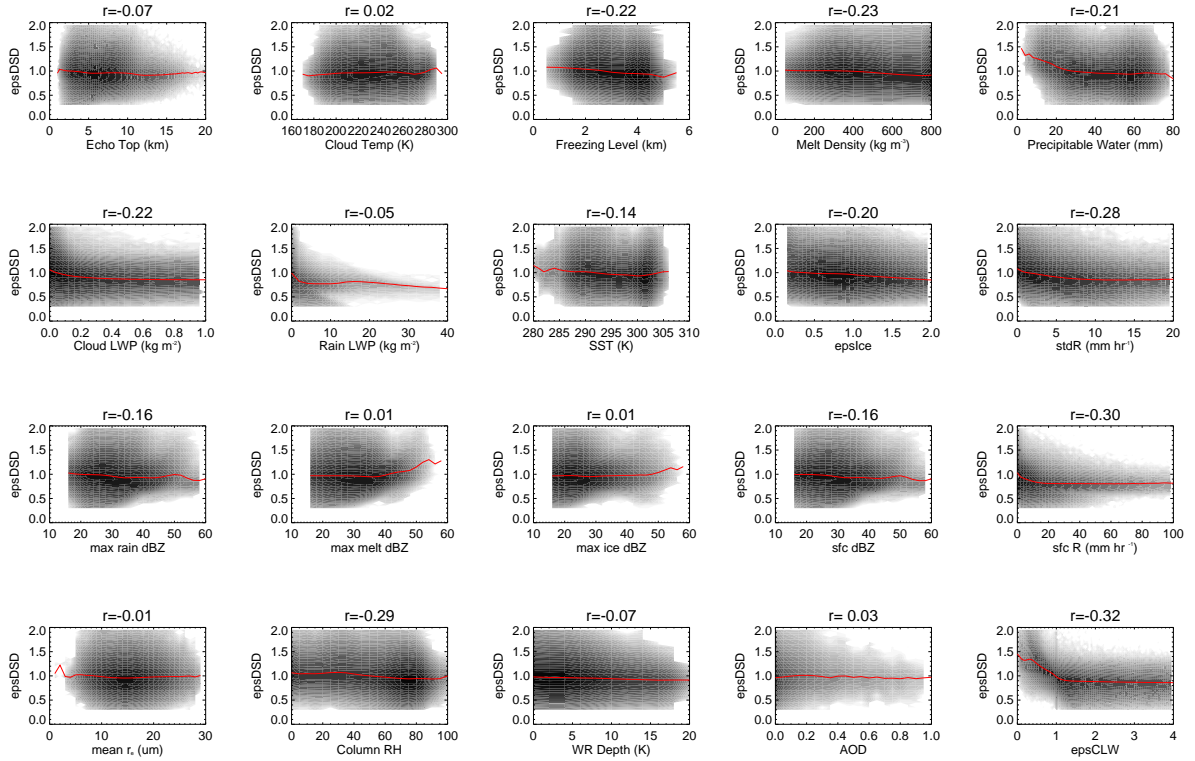


Figure 5.5: Same as Figure 5.5, except for ϵ_{DSD} instead of D_0 .

(upward and downward) to collect additional cloud droplets, and thus tend to be larger, than a drop that originates above the freezing level (downward only), assuming minimal growth via aggregation.

In figure 5.7, the two parameters most frequently used to categorize rain as convective or stratiform, the local standard deviation of rain rate and bright band strength (represented by the melt density) are examined. Here the absolute drop size depends mostly on the melt density, where weaker bright bands (higher melt density) represent graupel and hail, which form larger drops than melted aggregated snowflakes due to their higher water content. Meanwhile, the relative drop size is more strongly associated with the local variability of the rain rate.

The influence of environmental factors TPW and SST, which are used as look-up parameters in the latest version of the radiometer-only rain retrieval algorithm GPROF (Kummerow et al., 2010), is shown in figure 5.8. Here both the absolute and relative drop sizes follow similar patterns, indicating that each point in TPW-SST space has similar distribution of reflectivity profiles. The dominant pattern favors larger drops in low-TPW environments. At a given TPW, there is some preference for drop size

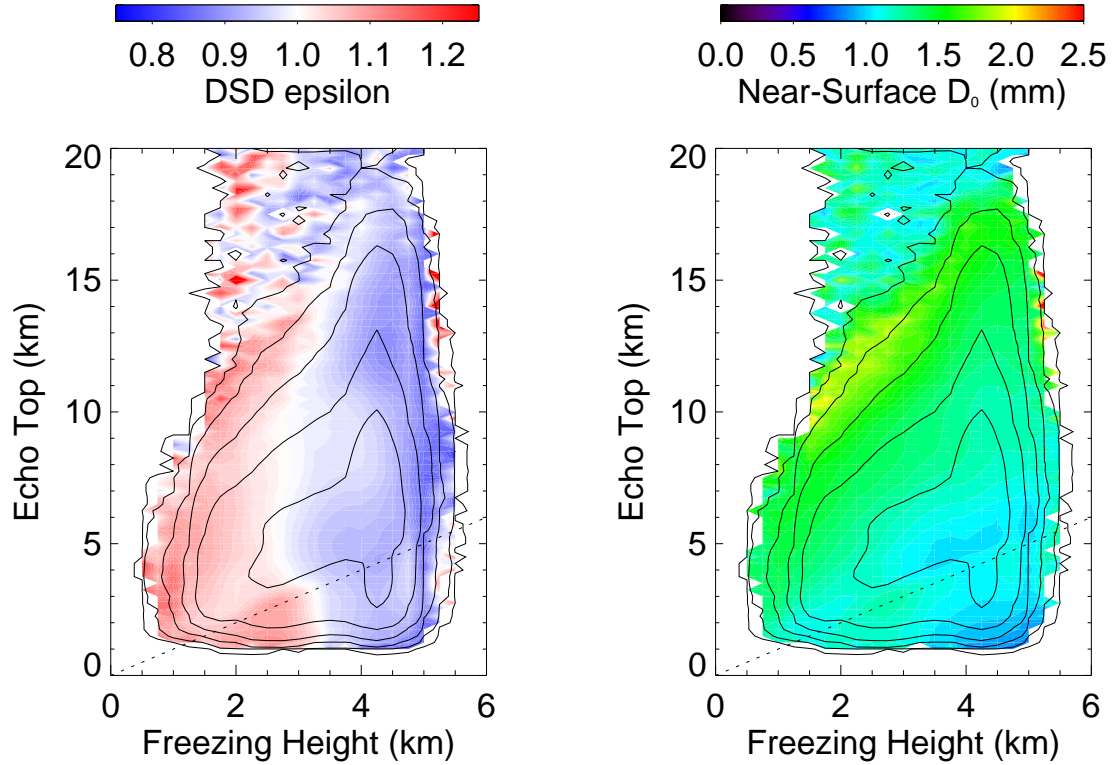


Figure 5.6: Contours of the mean values of ϵ_{DSD} (left) and D_0 (right) in versus freezing level and echo top height. Contours of number density are overlaid in black at levels of 1,10,100,1000,10000, and 100000.

to increase with SST which may represent lower relative humidity environments. A similar analysis performed between TPW and column RH (Figure 5.9) confirms this behavior, which is consistent with the effect of evaporation on DSDs. Low column RHs generally represent dry near-surface conditions since the column RH is effectively weighted by saturation vapor pressure, which is largest near the surface.

Finally, the two microphysical factors with the strongest correlations, warm rain depth and ϵ_{ICE} , are examined in Figure 5.10. Both absolute and relative drop size decreases slightly with increasing warm rain depths, however, D_0 increases with ϵ_{ICE} , which is greater than one when less scattering than the default model provides is observed. This is in contrast to relative drop size, which decreases when an adjustment towards less scattering is made.

In order to more clearly separate the influence of these factors, EOFs all of the variables in Table 5.1 are constructed. In subsets of pre- and post-boost periods as well as different information content

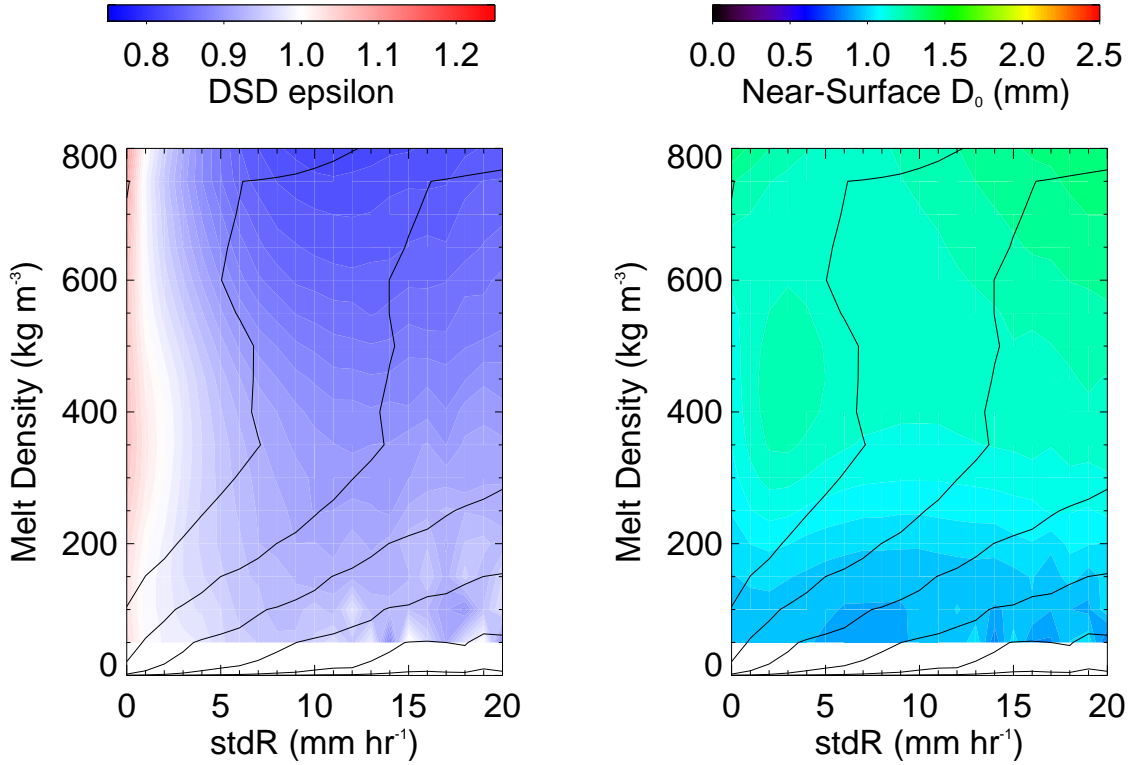


Figure 5.7: Same as Figure 5.6 but for rain inhomogeneity and melt density.

thresholds, the first three modes (Figure 5.11) remained remarkably similar for the different orbit altitudes and levels of information content, both in terms of correlations with each variable and percent of variance explained. Thus, the remainder of this section will focus on these, which also have the most clear physical interpretations and explain 46% of the variability in ϵ_{DSD} and 58% of the variability in D_0 .

The first EOF, explaining 8% of the variance in ϵ_{DSD} and 18% of the variance in D_0 , is most strongly associated with high reflectivities at all levels, high echo tops, cold cloud top temperatures, high rain and cloud LWPs, high spatial variability of rainfall, and weak bright bands (indicated by high melt density). All of these suggest that this mode represents rain intensity and is strongly correlated with the characteristics associated with stratiform rain on the weak end and convective rain on the strong end. For example, less than 10% of profiles with $\text{PC1} < -1$ are classified as convective, but this increases to nearly 60% for values of PC1 exceeding 2 (Figure 5.12). As expected, this mode contains large D_0 in an absolute sense, but small relative to the reflectivity.

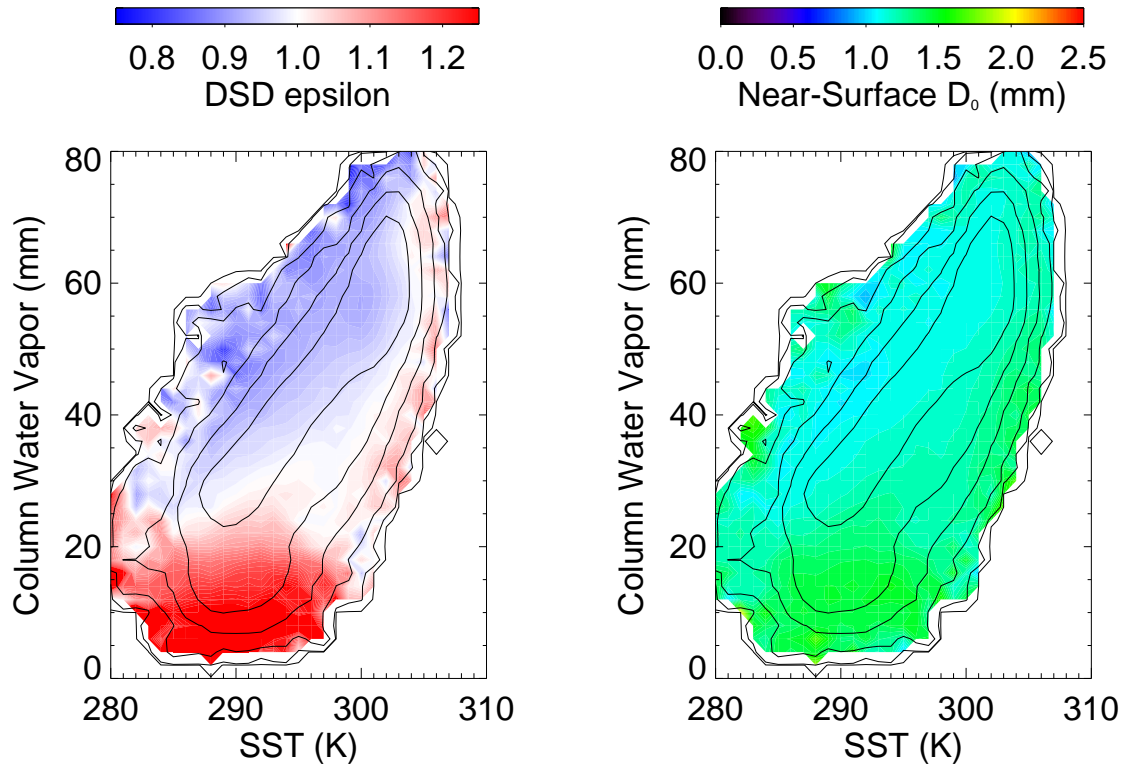


Figure 5.8: Same as Figure 5.6 but for TPW and SST.

The second EOF, which explains 13% of the variance in ϵ_{DSD} and 38% of the variance in D_0 , is most strongly associated with the environmental variables - freezing level, column water vapor, SST, and column relative humidity generally increase or decrease in unison. The tropical mode, represented by positive anomalies of these variables, is associated with smaller drops in a relative and absolute sense. This probably reflects the increasing contribution of warm rain processes to the evolution of the DSD in tropical environments, even for profiles that extend above the freezing level.

The next mode combines microphysical properties of the environment (warm rain depth, mean R_e , AOD) with storm reflectivity structure and microphysics. Continental-like environments (high AOD, low warm rain depth and mean R_e) are associated with larger ϵ_{DSD} , more ice scattering, colder clouds, and higher reflectivities in and above the freezing level, representing more dominant cold rain processes. This mode also contains the strongest correlation with ϵ_{DSD} of the first three EOFs as it represents 25% of its variance in the database (although only 2% of the variance in absolute drop size D_0). It should be noted that the next mode associates continental-like DSDs with a maritime environment and only

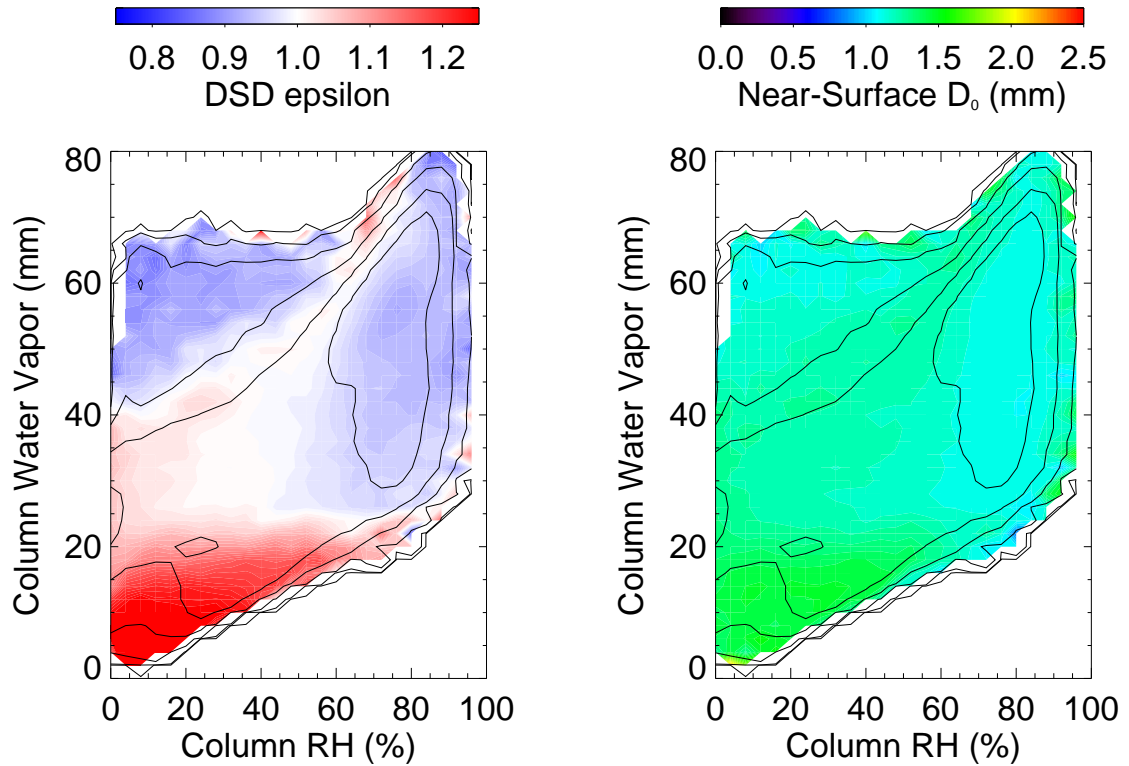


Figure 5.9: Same as Figure 5.6 but for TPW and column relative humidity.

explains slightly less variability in the dataset, however, the correlation with ϵ_{DSD} is much weaker (8% variance explained); thus, there is substantial evidence that not only are microphysically ‘cold’ clouds more likely to occur in an environment with higher aerosol loading, but these clouds are likely to contain larger drops at a given reflectivity than their microphysically warm counterparts.

5.4 Relationships between radar reflectivity structure and the rain DSD

The first and third EOFs in Figure 5.11 suggest that some of the DSD variability is related to the shape of the radar profile. To further investigate this relationship, a database of attenuation-corrected reflectivity profiles partitioned by freezing level, echo top, and stratiform/convective classification provided by the TRMM PR 2A23 product was created. For each freezing level–echo top subset, an EOF analysis was performed. In all cases, the first mode of variability represented the correlated increase/decrease of reflectivity at all levels, explaining 60-80% of the variance, whereas the second mode represented a negative correlation between reflectivities at high levels and those at low levels in the profile, typically

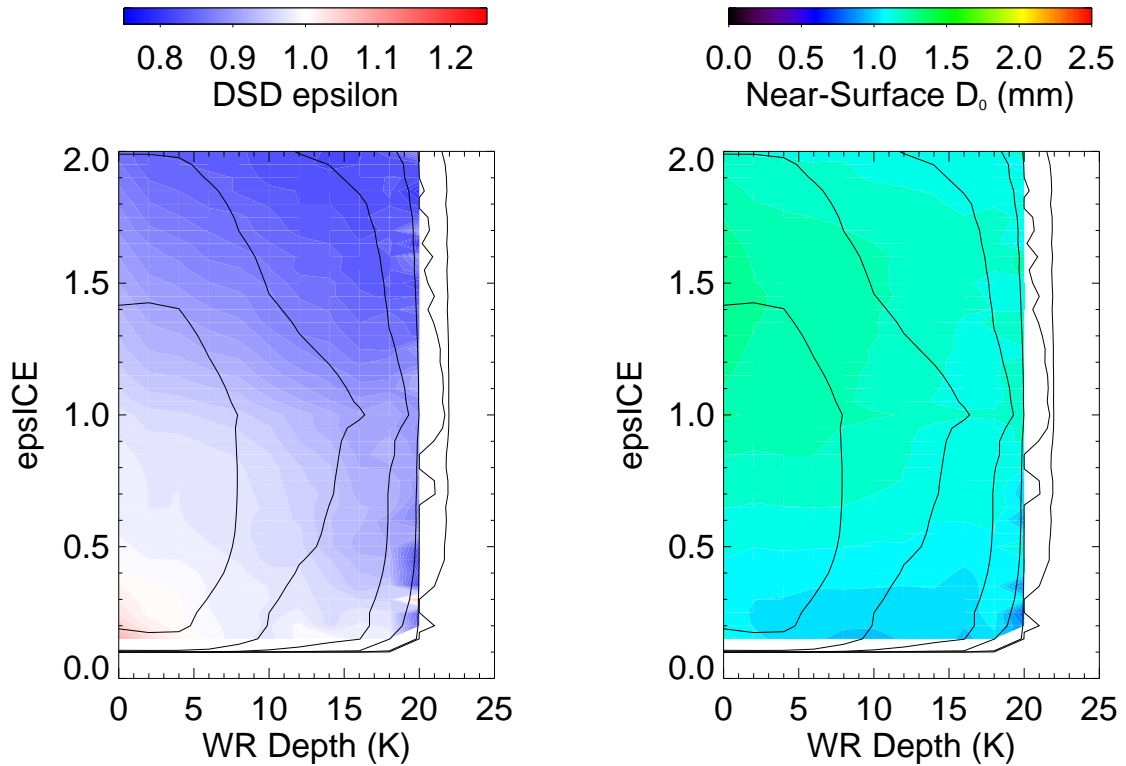


Figure 5.10: Same as Figure 5.6 but for warm rain depth and ϵ_{ICE} .

explaining 5-20% of the variance (an example is shown in figure 5.13).

The correlations between the first two reflectivity PCs (for each rain type) and ϵ_{DSD} , ϵ_{ICE} , and ϵ_{CLW} are shown in figure 5.14. The correlation of the first PC with ϵ_{DSD} can be thought of as a bias in the exponent (b) of the default $Z - D_0$ power law. If the true value of b were higher than the assumed value, one would expect that ϵ_{DSD} would systematically increase with reflectivity in order to compensate for the erroneous slope of the power law relationship. This tendency is noted particularly in the deep convective profiles with echo tops well above the freezing level. It is likely that a substantial amount of rain originates as frozen particles in these storms, and thus they contain larger rain drops near the surface. Conversely, stratiform profiles indicate a lower b , particularly as the freezing level increases. Since stratiform rain originates as aggregates above this level, this is consistent with the longer distance drops have to fall and approach the equilibrium DSD via breakup in these environments.

The second PC is almost always negatively correlated with ϵ_{DSD} , except for those profiles with freezing levels below about 3 km and echo tops below 4 km. In other words, bottom-heavy reflectivity

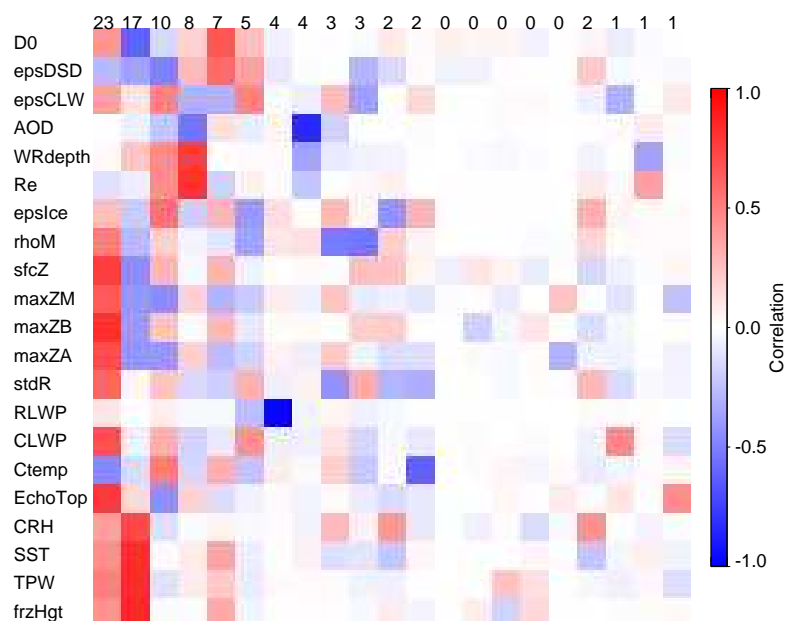


Figure 5.11: Matrix of EOFs derived from the profile database. The percent of variance explained is given at the top of each column. The correlation of each variable with each EOF is given by the color scale.

profiles are more likely to contain smaller drops at a given reflectivity than their top-heavy counterparts. Lower reflectivities above the freezing layer are indicative of less rain originating as ice, which is consistent with smaller drops according to the difference in warm and cold rain formation processes. The opposite tendency in profiles with lower freezing levels and echo tops may be because these represent shallow, post-frontal convection which occurs in a much different thermodynamic environment than the majority of profiles in the tropics.

As an independent verification of these tendencies, polarimetric radar data from the NAME field experiment were analyzed in a similar fashion. In this experiment, the National Center for Atmospheric Research (NCAR) S-Pol radar was situated near La Cruz, north of Mazatlan, Mexico for the 6-week period from early July through mid-late August, 2004. Quality-controlled, Cartesian gridded datasets were generated at 0.02° horizontal and 1 km vertical resolution every 15 minutes (Lang et al., 2010). For this analysis, the subset of profiles with full radar coverage from 0 to 20 km altitude was selected based

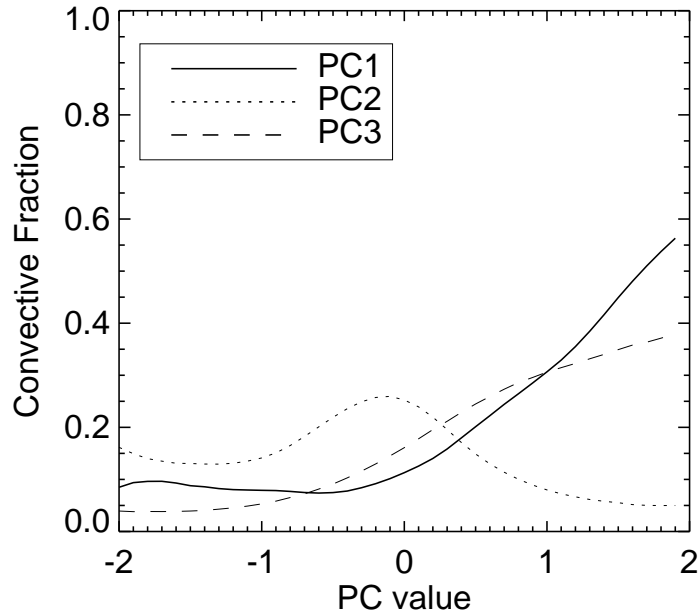


Figure 5.12: Convective fraction (according to 2A23 classification) of profiles as a function of PCs 1-3.

on the scan geometry. Convective/stratiform separation was determined by the absence or presence of a reflectivity peak at the 3 km height level. Below this level, D_0 was retrieved from the polarimetric variables horizontally-polarized reflectivity Z_H , differential reflectivity Z_{DR} , and differential phase K_{DP} using the equations provided in the appendix of [Bringi et al. \(2004\)](#). A power law $D_0 = 0.70Z_H^{0.104}$ was derived from this dataset by linear regression analysis, and a quantity D_0^* (analogous to ϵ_{DSD}) was derived by dividing the retrieved value of D_0 at each grid point by the value expected from the power law.

The EOFs of the reflectivity profiles (partitioned only by echo top since freezing level did not vary much over the course of the field experiment) are similar to those derived from the TRMM PR global dataset, with the first mode representing correlated changes in reflectivity throughout the profile and the second mode indicating the degree to which a profile is top- or bottom-heavy. The correlations of each PC with D_0^* (Figure 5.15) do show some resemblance to their counterparts in the TRMM dataset with some minor differences. There is a tendency for both the convective and stratiform PC1 to be positively

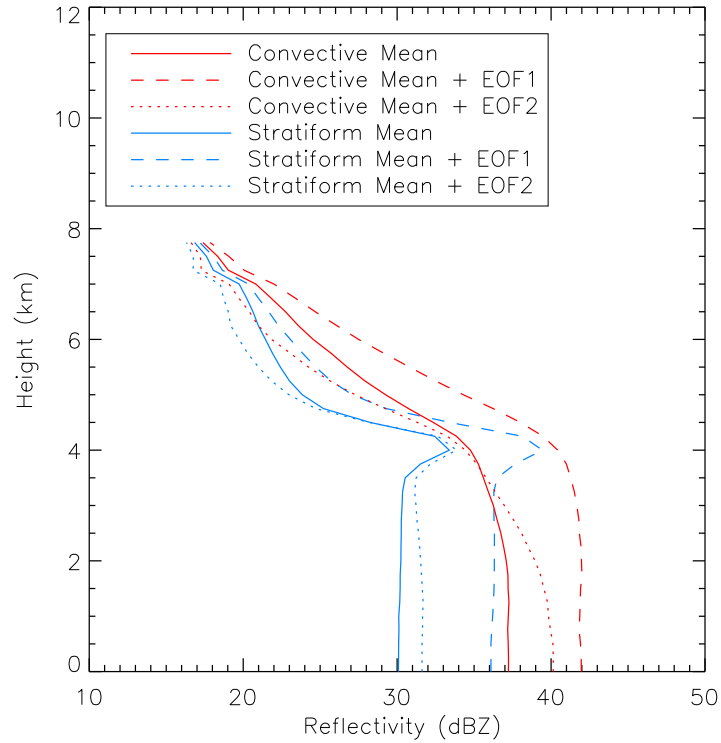


Figure 5.13: Sample reflectivity EOFs for all profiles with an echo top between 7.5 and 8 km and a freezing level between 4 and 4.5 km.

correlated with D_0^* for low and high-topped profiles, with negative correlations for those with tops in the mid-levels, although the trends are shifted upwards by a few km from the TRMM data. Meanwhile, PC2 is generally negatively correlated with D_0^* , although there are some positive correlations for shallow convection (also present in the TRMM dataset). That these tendencies agree in a general sense indicates that they are likely not an artifact of bias in the combined retrieval method.

Returning to the TRMM data, correlations of the first reflectivity PC with ϵ_{ICE} are positive for both rain types at all freezing levels and echo tops. This is probably indicative of a general bias in the assumed power law relating the ice PSD to reflectivity. Due to the simple ice model used, however, the only conclusion that can be drawn is that ice scattering at 85 GHz tends to be less strong than expected as PR reflectivity increases, particularly in stratiform rain. The second PC is only weakly correlated with ϵ_{ICE} , but a few patterns are apparent. For storms with echo tops just above the freezing level, the opposite behavior to correlations with ϵ_{DSD} is observed - that is, bottom heavy profiles have more scattering at

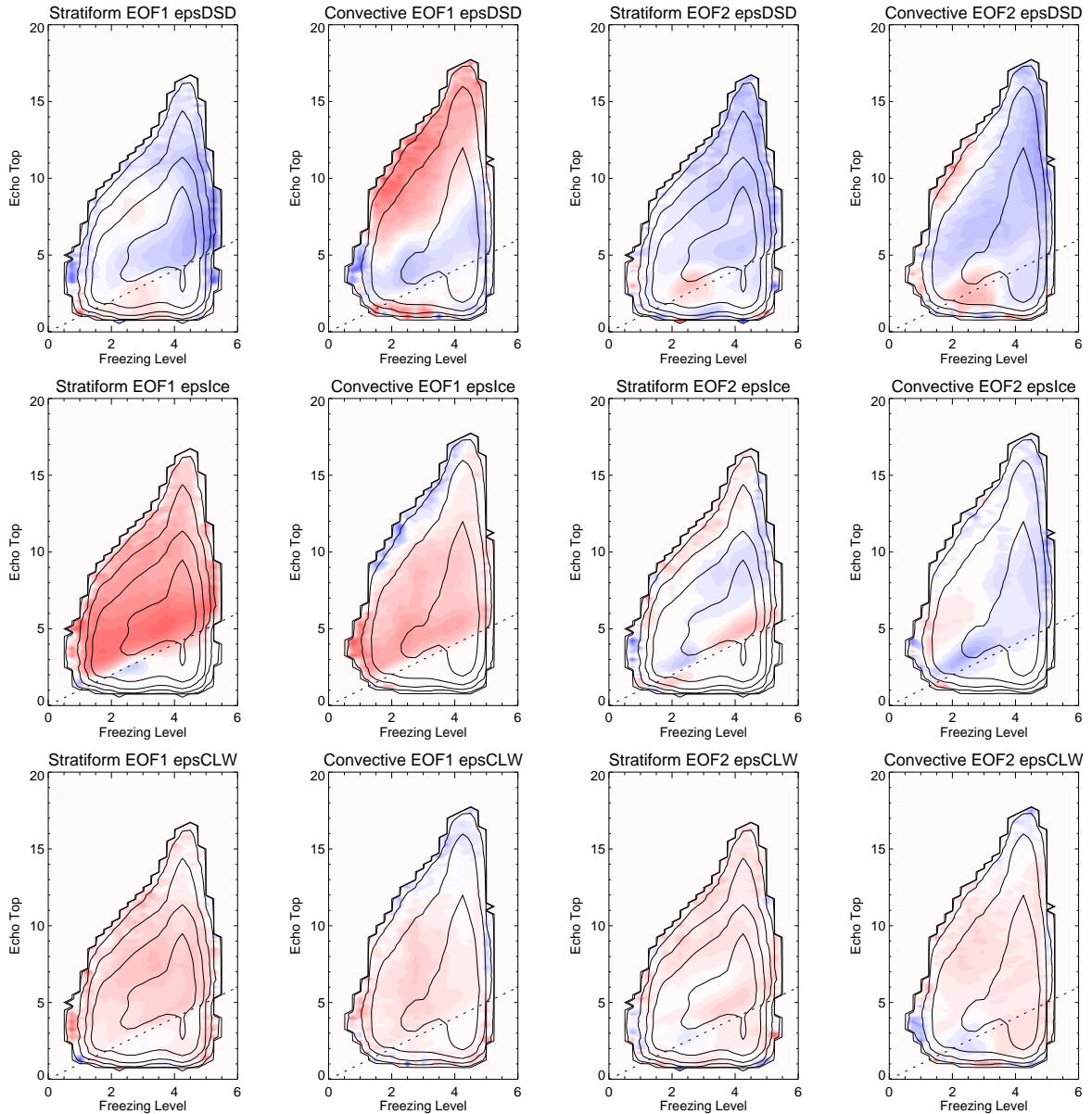


Figure 5.14: Correlation of ϵ_{DSD} , ϵ_{ICE} , and ϵ_{CLW} with reflectivity PC1 and PC2 for rain classified as stratiform or convective by the TRMM 2A23 algorithm. The color scale is the same as in Figure 5.11.

low freezing levels and less at high freezing levels. For storms with echo top well above the freezing level, negative correlations are generally observed which is consistent with the correlations with the first PC, since positive values for the second PC represent negative reflectivity anomalies at high levels in the profile.

The correlations with ϵ_{CLW} do not show any clear patterns with freezing height and echo top, but the fact that they are positive everywhere does indicate that higher-reflectivity profiles and bottom-heavy

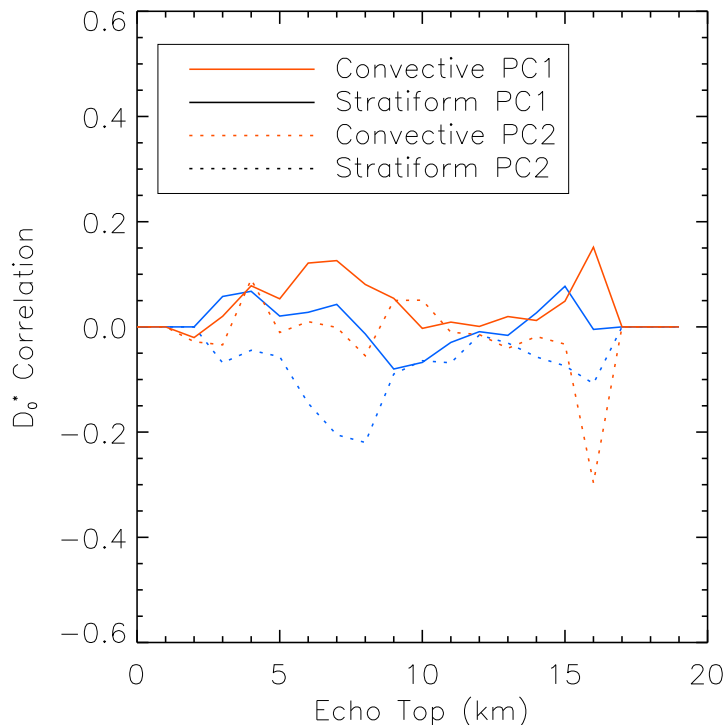


Figure 5.15: Correlation of reflectivity PCs with D_0^* as a function of echo top during the NAME field experiment.

profiles tend to have more cloud water than given by the default profiles. Thus, it appears that a weak positive relationship exists between rain intensity and cloud water fraction, not just amount.

The strong correlations, particularly of ϵ_{DSD} and ϵ_{ICE} , with EOFs related to the reflectivity structure suggest that at least some of the variability in these variables can be associated with the reflectivity profile. A potential application of this information is a Bayesian profile matching method to set the default value of these variables in situations where additional constraints (*e.g.*, SRT PIA or radiometer T_{bs}) are unavailable or unreliable, as is often the case over land. This is similar to the concept suggested by [L'Ecuyer et al. \(2004\)](#) and is explored further in Appendix [C](#).

5.5 Regional and Seasonal Distribution of DSD variability

In the preceding section the primary dynamical, environmental, and microphysical factors that are related to the rain DSD were identified. In this section, the global patterns of these variables are given

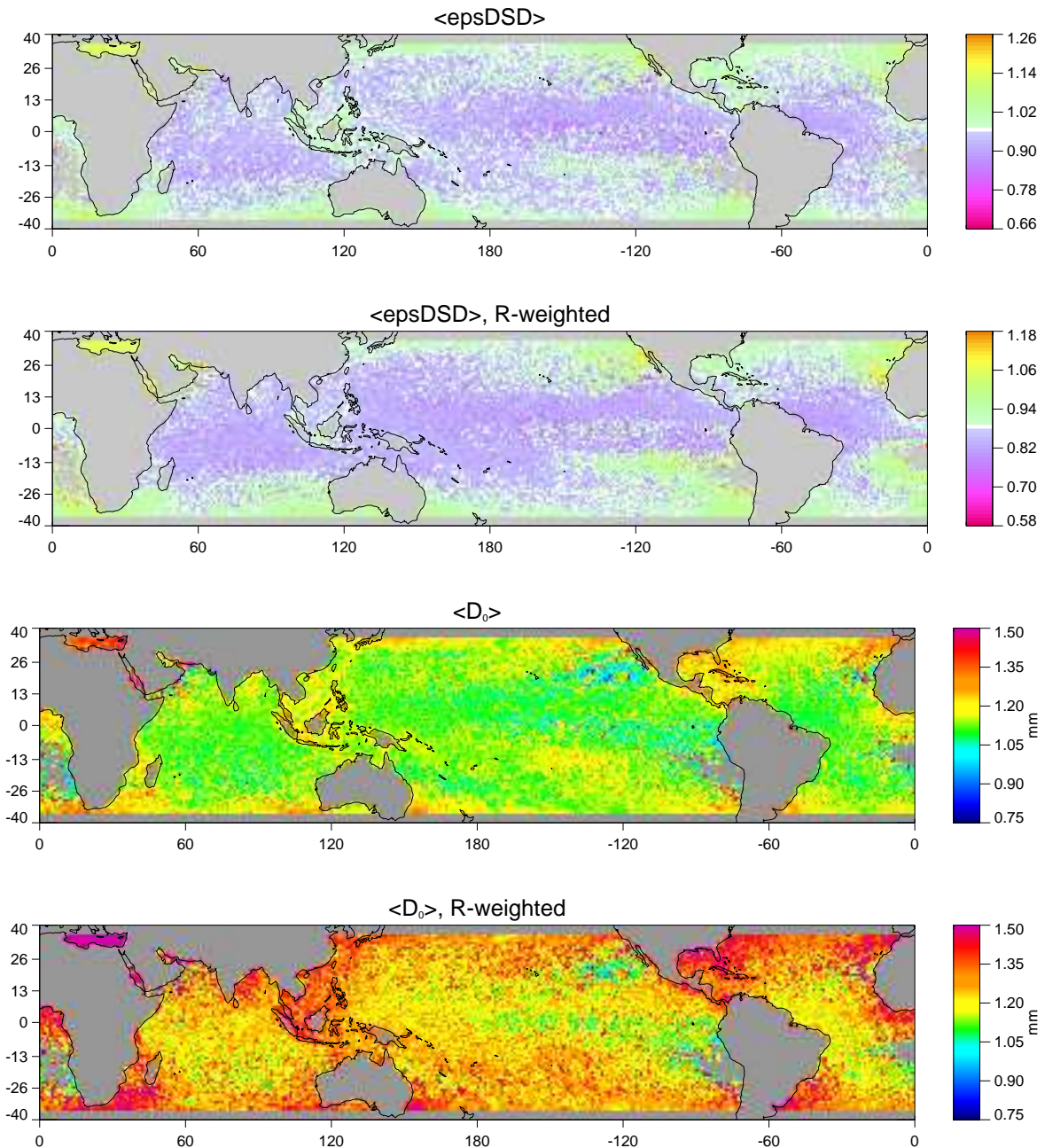


Figure 5.16: One-degree gridded means (unweighted and weighted by rain rate) of ϵ_{DSD} (top two panels) and D_0 (in mm; bottom two panels). Note that the color scale for ϵ_{DSD} is centered on the mean value instead of 1 in order to highlight regional differences.

and interpreted in context of the TRMM TMI/PR bias map of Berg et al. (2006) and the PR-derived DSD map of Kozi et al. (2009).

The main feature of the global distribution of ϵ_{DSD} (Figure 5.16) is the trend towards larger values

at high latitudes. This is most likely a combination of the prevalence of stratiform rain and the extra-tropical environment (Figure 5.18) that are present particularly in the winter season (Figure 5.17) at these latitudes. There is also some seasonality present off the west coast of Africa, with a tendency towards larger drops in northern hemisphere winter and spring. Another feature apparent in both maps is the tendency towards larger drops near the so-called “maritime continent” spanning between Australia and southeast Asia. The primary distinguishing feature in this region is the predominance of the cold micro-physical mode (PC3). The region surrounding Central America and the northern Indian Ocean also share this feature. In these regions/seasons, it has been suggested (Rosenfeld and Lensky, 1998) higher aerosol loading decreases the efficiency of warm rain processes, leaving more cloud water to form precipitation above the melting layer, consistent with the presence of larger raindrops at the surface.

Maps of the mean value of the reflectivity PCs (Figure 5.19) also shed some insight on the source of the DSD patterns and TMI/PR biases. The second convective PC displays the clearest regional patterns which are strikingly similar to the bias patterns between version 6 of the TMI and PR rainfall products. The positive mode of PC2, which represents bottom-heavy convection, is generally associated with regions where TMI-based algorithms estimate more rainfall than their PR counterparts (and vice-versa). The DSD in this mode is associated with more liquid water (and higher rain rates) for a given Z than the default PR; since only a small fraction of profiles have rain heavy enough to create a PIA signal strong enough to merit an adjustment from this default, PR rain rates may be biased low against the true rain rate in these regions. Additionally, for reasons discussed in section 5.1, TMI rainrates may also be biased high if an incorrect DSD is assumed in the conversion of liquid water content to rain rate, thus, the true rain rate may lie somewhere between the PR and TMI estimates.

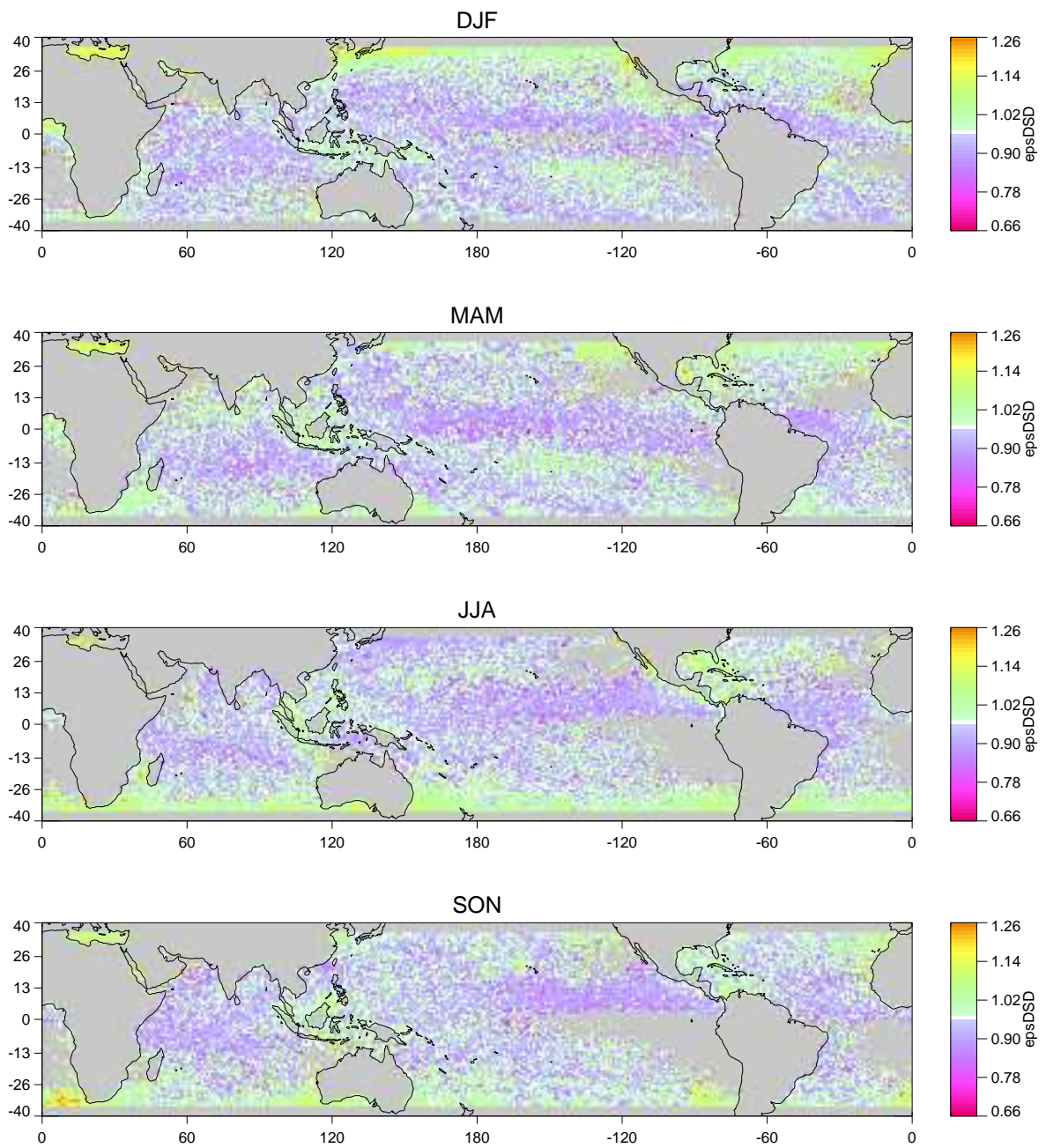


Figure 5.17: One-degree gridded means of ϵ_{DSD} by season.

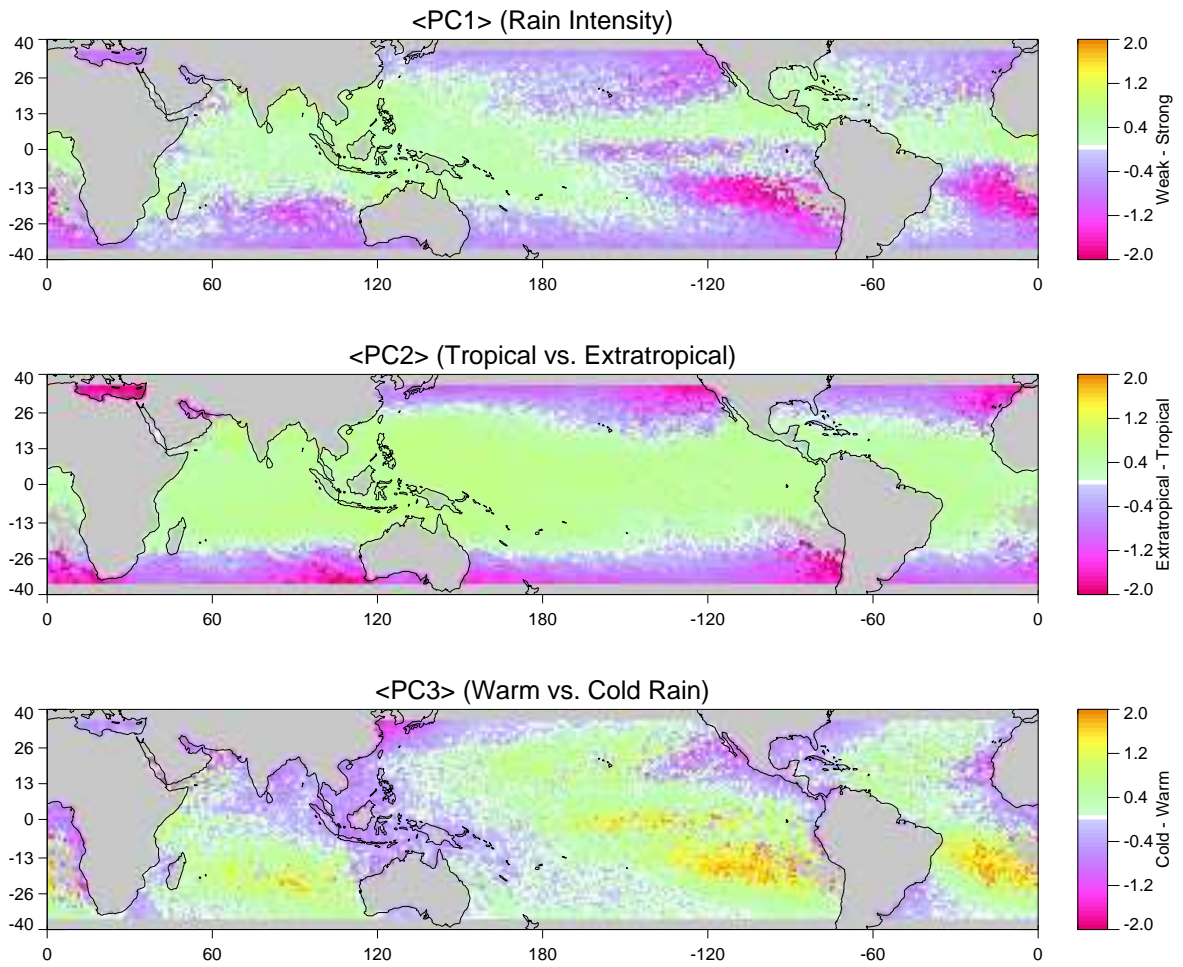


Figure 5.18: One-degree gridded maps of the mean values of the three leading PCs identified in section 5.3.

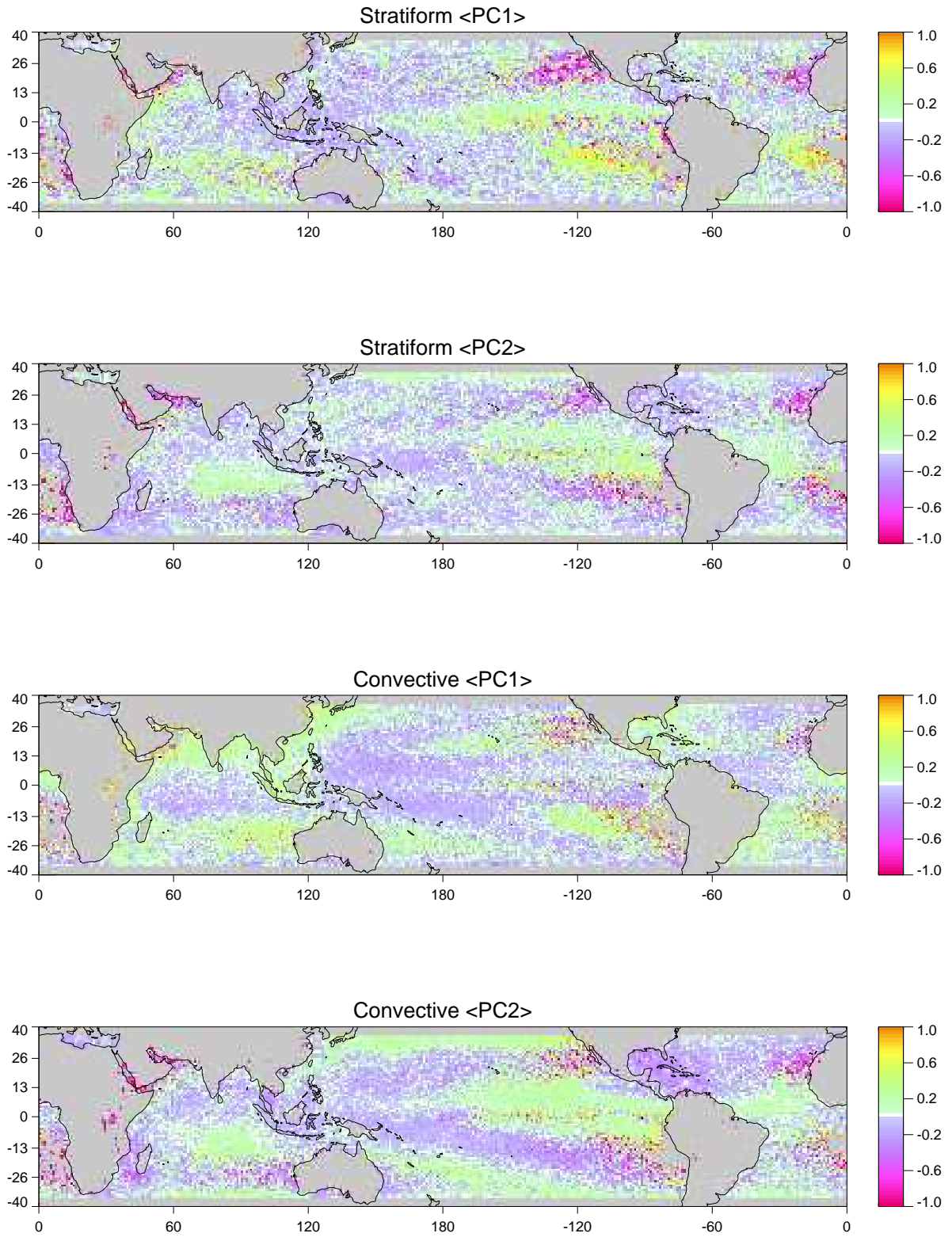


Figure 5.19: One-degree gridded means of the reflectivity PCs identified in section 5.4.

Chapter 6

CONSTRAINTS ON GLOBAL RAINFALL AND ENERGY BUDGETS

This chapter examines two issues related to the global mean rainfall and its role in the energy budget. Section 6.1 compares the mean rainfall rate over the tropics with other algorithms, including uncertainty assessments. These values are inserted into a simple global energy budget to check for consistency with the other terms. Section 6.2 investigates the issue of rainfall trends from a remote sensing perspective. The properties of rainfall derived from the combined algorithm in chapter 5 are used in a heuristic experiment to determine if they might mask or exaggerate trends in rainfall that come about to increases in global mean water vapor.

6.1 The Global Oceanic Tropical Rainfall Rate and Uncertainty

The global annual area-weighted mean precipitation rate from the Global Precipitation Climatology Project (GPCP) version 2.1 (Adler et al., 2003), containing data from 1979 to 2008, is 2.67 mm/day. Of this, 63% falls between 35°N and 35°S, the region seen by the central swath of the TRMM PR. In this region, the mean rainfall rate from GPCP is 2.93 mm/day. Within these latitude bounds, approximately 70% of the surface is ocean and there, the mean rainfall rate is a nearly identical 2.94/day. Therefore tropical oceanic rainfall comprises 44% of the global total according to GPCP, which is largely based upon passive microwave retrievals over the ocean. In order to facilitate more direct comparisons with the combined algorithm, zonal means of GPCP data that cover the oceans within the latitude bounds of TRMM during the months analyzed for the combined algorithm are compared in Figure 6.1. For this space and time subset, the GPCP mean is 2.87 mm/day. This compares with a mean values of 3.06 mm/day from the combined algorithm, 2.66 mm/day from 2A25, 2.51 mm/day from the radar-only OE

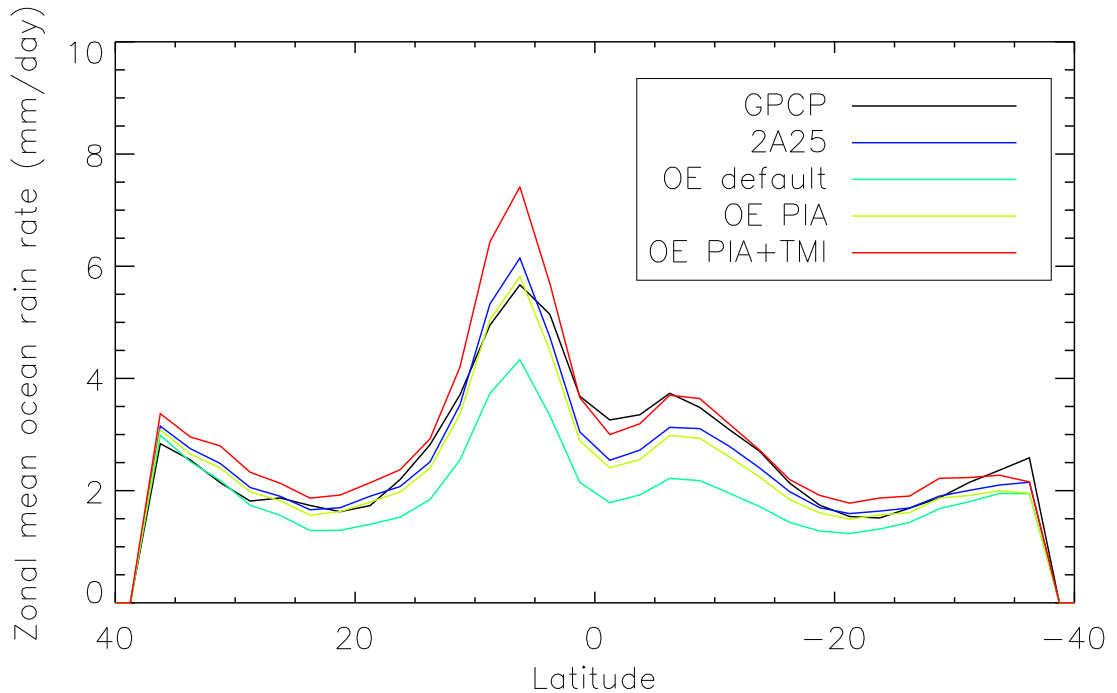


Figure 6.1: Mean zonal rain rates from GPCP and various TRMM PR-based algorithms.

algorithm, and 2.02 mm/day from the radar algorithm without SRT PIA adjustment from the default DSD. All algorithms give similar zonal means poleward of about 20° , but large differences are present in the tropics. In the northern hemisphere, the combined algorithm is higher than the PR-based and GPCP estimates by about 15%. In the southern hemisphere, the combined algorithm agrees with GPCP but is higher than the PR-based algorithms by a similar amount.

There are a number of ways to derive an uncertainty value for these means. Perhaps the most robust way is to modify the assumptions in each algorithm within a reasonable range of values. This was done for the radar algorithm in section 3.2 and for the combined algorithm in section 4.2. The default DSD and sensitivity to PIA represent the two main sources of uncertainty in the radar algorithm. Adjusting the latter changes the mean rainfall rate by about 5-10% (Figure 3.3). Meanwhile, since 55% of rainfall is not adjusted by the PIA (Figure 5.2), the choice of default Z-R relationship has a significant impact on the global mean. Replacing the convective $Z - R$ relationship with the stratiform one reduces retrieved rainfall by about 7% globally, even though many convective pixels are unchanged since they are constrained by the PIA. Combining these error sources, an uncertainty of 10-20% might be considered

reasonable for radar products such as 2A25, and might be even higher when non-uniform beam filling effects are taken into account (Iguchi et al., 2009) and detection issues are considered (Berg et al., 2006).

Uncertainties in the combined algorithm are largely tied to the cloud water/rain water partitioning, discussed in chapter 4. By using GV to constrain this partitioning, the uncertainty is reduced although additional GV sites might provide a more robust estimate of this uncertainty. Because most pixels are adjusted by the radiometer, this algorithm is less sensitive to the default DSD than a radar-only algorithm, as changing the convective $Z - R$ relationship to the stratiform one only reduces the retrieved mean rain rate by about 3%. Considering these error sources, a rough uncertainty estimate in the combined algorithm is on the order of 10-15%.

Adler et al. (2009) suggest that differences between algorithms might be representative of the uncertainty in the global rainfall rate. Although they only took the standard deviation of TRMM TMI (2A12), PR (2A25), and combined (2B31) products, a similar calculation can be done with the algorithms considered in Figure 6.1. The default radar retrieval is excluded because it is not constrained by any other observations. For the remaining algorithms, the mean tropical oceanic rainfall rate is 2.75 mm/day with a standard deviation of 0.23 mm/day, or 8.4%.

Turning toward the role of rainfall in the global energy budget, it is first useful to examine the other terms to determine if these suggest a similar value for the global mean rainfall rate that more direct estimates provide. The most recent energy budget analysis by Trenberth et al. (2009) provides a good review of each component and its uncertainty. The atmospheric components, of which latent heat (rainfall) is part, are listed in Table 6.1. Uncertainties not explicitly given by Trenberth et al. (2009) are the standard deviation of estimates listed in tables therein or those from which they were derived. Latent heating is calculated as a residual and its uncertainty is derived assuming a Gaussian distribution of the other components. The mean value of 80.7 W m^{-1} corresponds to a global mean rainfall rate of 2.79 mm/day^1 , which is slightly higher than the GPCP value but reasonable if the adjustments made to tropical rainfall by the combined algorithm are correct and light rainfall not well detected by PR or TMI, but observed by CloudSat (Haynes and Stephens, 2007) is added. The uncertainty from the energy budget analysis is about 17%, about twice the standard deviation from physical retrieval algorithms over

¹ assuming a rainfall-weighted mean temperature of 15°C and 10% of precipitation falling as snow

Table 6.1: Components of the atmospheric energy budget and uncertainties from [Trenberth et al. \(2009\)](#)

Component	Global Mean (W m^{-1})	Uncertainty (W m^{-1})
Absorbed Solar	+78.2	5.9
Sensible Heat	+17	2.0
Absorbed Longwave	+356	2.5
Emitted Longwave (to space)	-199	8.1
Emitted Longwave (to surface)	-333	9.1
Latent Heat	-80.7	14

tropical oceans².

6.2 Detection of Trends in Global Mean Rainfall

Increased concentrations of greenhouse gases are thought to have a direct effect on the global water cycle by altering many of the terms in Table 6.1 ([Allen and Ingram, 2002](#)). One response that is seen in both models ([Held and Soden, 2006](#)) and observations ([Trenberth et al., 2005](#)) is an increase in total precipitable water vapor (TPW) that scales with temperature according to the Clausius-Clapeyron relation such that relative humidity remains constant as surface temperatures increase. Because there is a strong relationship between TPW and PR/TMI algorithm biases ([Berg et al., 2006](#)) and some of these may be related to relationships between water vapor and the rain DSD (chapter 5), it is worthwhile to examine whether these biases could affect detection of rainfall trends from radar and radiometer algorithms.

The distribution of TPW and rain properties in the database described in chapter 5 is shown in Figure 6.2. These properties are selected since passive and active retrievals are highly sensitive to them and most algorithms assume some relationship between them and the rain rate. In this simple sensitivity test, a $Z - R$ power law relationship, meant to represent a simple radar algorithm, and LWP- R power law relationship, meant to represent a simple radiometer algorithm, are derived at each TPW bin. The coefficients of these power laws are plotted in Figure 6.3.

To examine the bias that might occur with increasing TPW, the TPW pdf is shifted towards higher

² Neither the uncertainty in rainfall from various algorithms or energy budget components can be considered truly robust estimates, since neither algorithms ([Kummerow et al., 2010](#)) nor energy budget individual component estimates are totally independent

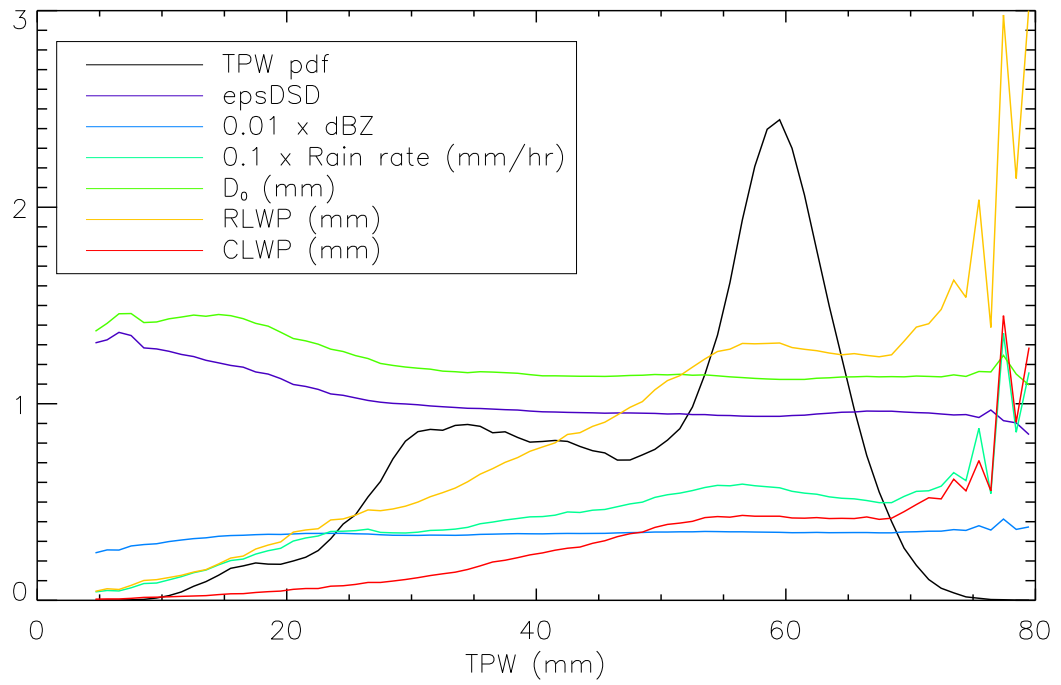


Figure 6.2: Various rain quantities relevant to remote sensing as a function of TPW. Scaling coefficients are given in the legend.

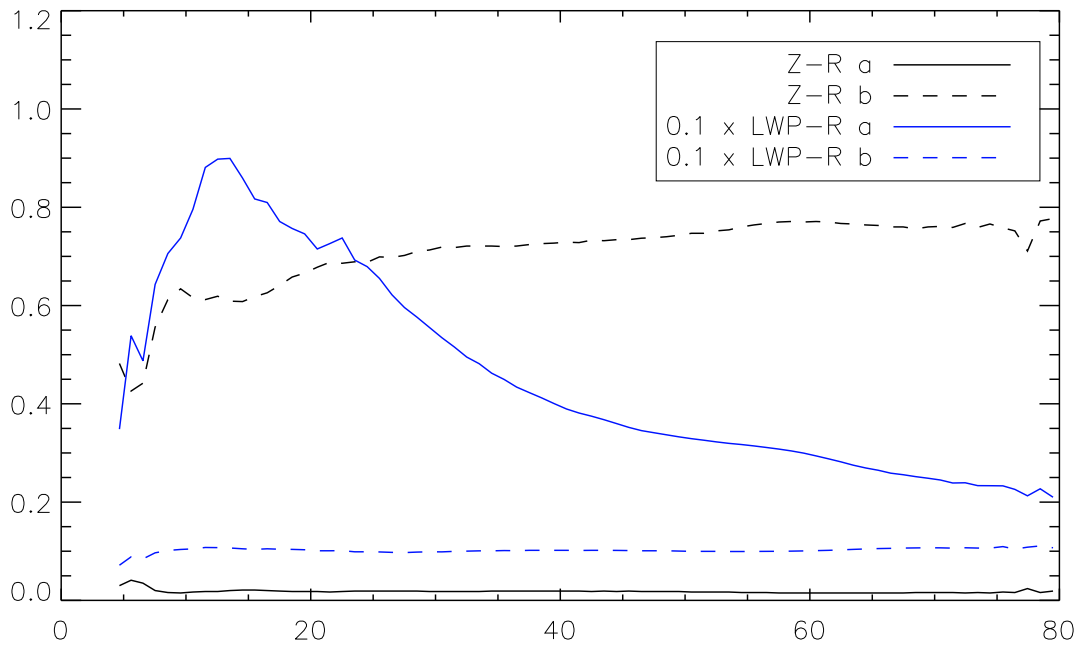


Figure 6.3: Parameters a and b in $R = aZ^b$ and $R = aLWP^b$ as a function of TPW.

values to mimic a 7% increase, roughly in line with 1°C of surface warming. Rain amounts are also shifted, but do not change so this experiment represents the null result, *i.e.*, no change in rainfall. The mean reflectivity and LWP in each bin is then re-calculated using the previously derived, non-shifted power laws on the shifted rain rates. The resulting changes in Z or LWP averaged across all TPW bins can then be used to infer the potential bias in an algorithm that does not assume any relationships of rain properties with TPW.

Using this method, the mean reflectivity decreases by 0.07 dBZ and the mean LWP increases by 0.07 kg m^{-2} even though the mean rain rate has not changed. Essentially, these changes reflect the properties of rain in high-TPW regimes: lower reflectivity for a given R due to smaller D_0 and increased LWP for a given R due to increased cloud water fraction and freezing level (Figure 6.2). Without accounting for these changes, the rain rate from the average $Z - R$ relationship decreases by 1.1% and the rain rate from the average LWP- R relationship increases by 4.6%. These represent the magnitude of biases that might be expected with TPW trends in radar and radiometer algorithms that do not account for the differing properties of rain in different TPW regimes. Interestingly, subtracting the 4.6% radiometer bias from the 7% figure reported by [Wentz et al. \(2007\)](#) gives an amount that is in line with the 1-3% expected by [Allen and Ingram \(2002\)](#) and [Stephens and Ellis \(2008\)](#).

[Lau and Wu \(2006\)](#) report another type of trend in rainfall that is associated with a changing in the distribution of rain by intensity. They found an increase in light and heavy rainfall at the expense of moderate rain rates in GPCP and gauge-only datasets over land. To evaluate the possible impact of this trend on remote sensing algorithms, the biases of 2A25 and both the CRM- and PR-based GPROF algorithms (GPROF2004 and GPROF2008, respectively) relative to the combined algorithm rainfall are shown in Figure 6.4. GPROF2008 is biased very high compared to the combined algorithm at light rain rates, and so increases in rainfall here would disproportionately increase the overall rainfall. However, some of this might be offset by negative biases in heavy rainfall, depending on the exact magnitude of the trends at each intensity. A similar but less pronounced error pattern is seen in 2A25, whereas the CRM-based GPROF2004 best matches the combined algorithm at most rain intensities and thus its overall bias compared to the combined algorithm would not change with a change in the rain pdf.

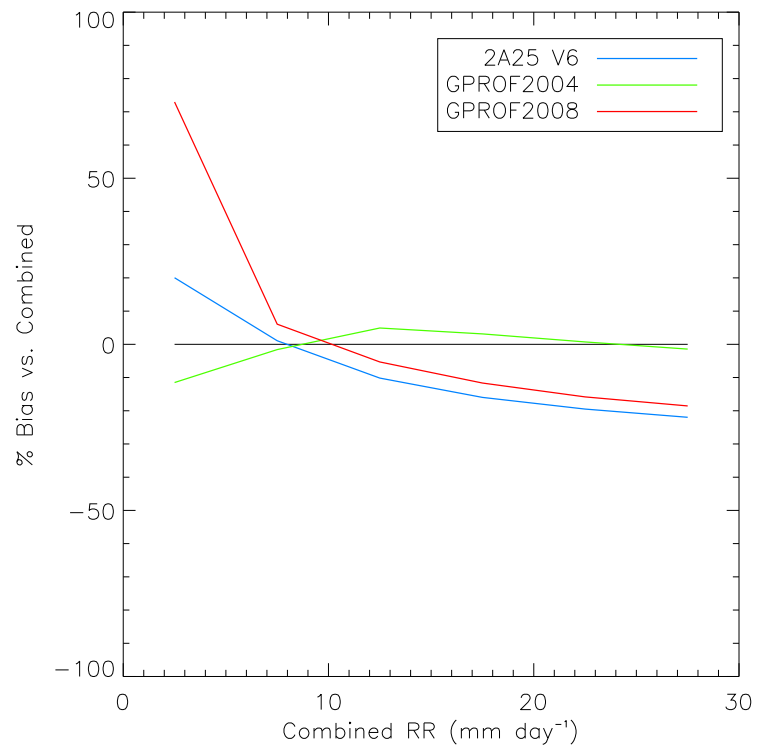


Figure 6.4: Algorithm biases relative to the combined algorithm as a function of mean rain rate in a 1-degree grid square.

Chapter 7

CONCLUSIONS

This dissertation has described several aspects of rainfall remote sensing from the design of a combined radar-radiometer algorithm for the TRMM satellite to the findings and applications of the data produced by this algorithm. The main findings, in context of the questions posed in chapter 1 are summarized in section 7.1. Additionally, some avenues for future work are outlined in section 7.2. Finally, concluding remarks are given in section 7.3.

7.1 Main Findings

Although radar- and radiometer-based satellite measurements of rainfall have been available over the global tropics for over a decade, key uncertainties remain in some regions. Instrumental strengths and shortcomings as well as algorithm assumptions are thought to play a role in creating the regional biases evident in long-term radar and radiometer based products from the TRMM satellite. In an effort to explain these biases as well as prepare for GPM, where combined radar-radiometer profiles will be used as the Bayesian database for constellation radiometers, a new method has been devised to use radiometer measurements to retrieve hydrometeor profiles from radar reflectivity profiles.

Here, each of the questions posed in chapter 1 is revisited. Although some of these questions were answered more definitively than others, all were addressed in this dissertation.

What techniques are required to combine radar reflectivity profiles and multi-resolution, overlapping passive microwave radiometric measurements in an internally consistent geophysical product? The key component of the combined algorithm, and the primary difference from existing methods, is a radar profiling algorithm with three variable parameters representing the ice PSD, rain

DSD, and cloud LWP in each radar pixel. A variational optimal estimation inversion is used to adjust the profiling algorithm parameters to best match the observed microwave radiances and SRT PIA over a scene containing hundreds to thousands of PR pixels. The overall framework is modular, allowing for easy inclusion of different microwave scattering tables and radiative transfer models as well as any ancillary data regarding non-retrieved background parameters.

Can a combined algorithm compare favorably to single-instrument algorithms, in terms of bias, compared to well-calibrated ground-validation (GV) products? Validation of the algorithm was presented in three parts. First, the retrieval of cloud LWP outside the rain was demonstrated to show an improved correlation with VIRS-based retrievals relative to methods that consider each TMI FOV independently. This is an important verification of the whole-scene retrieval as a solution to one of the greatest problems faced when combining radar and radiometer measurements, the mismatched FOVs and how to deal with the corresponding partial beam-filling effects.

TRMM PR and ground-based radar datasets were used to set the uncertainty in the *a priori* DSD and cloud water assumptions. These uncertainties were fit to best match 2A25 and polarimetric radar rainfall retrievals at Kwajalein respectively. These same values were then used in retrievals over Melbourne, FL, where rainfall totals were within 2% of the GV value, well within the range of uncertainty expected given sampling error and a significant improvement from the default DSD assumption in the winter and early spring months. That the combined algorithm bias relative to GV was within 2% at both Kwajalein and Melbourne is not a guarantee that this accuracy exists elsewhere, but does represent an improve from the stand-alone PR and TMI products that have biases exceeding 5% at one or both of these sites.

Can the combined algorithm reliably measure two independent parameters of the raindrop size distribution (DSD)? If so, are these parameters related to properties of the clouds and/or the environment? The addition of independent information in the form of the SRT PIA and microwave T_{bs} to the reflectivity profile allows the retrieval of an independent parameter ϵ_{DSD} , which is the reflectivity-normalized median drop size D_0 . The ability to retrieve this parameter accurately was confirmed by comparing disdrometer-observed differences in the DSD between Melbourne and Kwajalein and finding that they were consistent with the differences retrieved by the combined algorithm.

Several reasons for these DSD differences have been hypothesized, with many studies (summarized by (Rosenfeld and Ulbrich, 2003)) pointing to cloud dynamics (convective vs. stratiform) and microphysics (continental vs. maritime) as primary sources of variability. These and other factors were analyzed extensively in chapter 5 where it was found that:

- More intense rainfall is associated with larger drops in an absolute sense, but smaller relative to reflectivity. These properties are also associated with weaker bright bands and horizontal inhomogeneity of the rain field which are characteristics of the stronger updrafts associated with convection.
- Extratropical environments tend to have larger drops than tropical environments, all other factors being equal. The effect of evaporation and time for drop breakup processes to occur are thought to be the leading influence in this context.
- Microphysically maritime clouds have smaller drops than their continental counterparts, as expected.
- The exponent of the $Z - D_0$ power law tends to increase with echo top height in convection, indicating the increasing contribution of cold rain formation.
- The exponent of the $Z - D_0$ power law tends to decrease with increasing bottom-heaviness of the reflectivity profile, indicating the increasing contribution of warm rain processes. This is consistent with dual-pol radar DSD retrievals from the NAME field campaign.

Together, these environment and cloud properties explain nearly half of the variability in median drop size D_0 at a given reflectivity. The remaining variability might be related to factors unobservable by the TRMM instruments, such as updraft strength and horizontal displacement due to wind shear, inadequate resolution of the low-frequency microwave footprints used to adjust the DSD, or temporal variability within a given set of environmental, microphysical, and dynamical factors.

Relationships between the rain DSD and the two dominant modes of variability in the vertical profiles of reflectivity observed by PR have also been identified. The first mode, which represents the unidirectional increase/decrease of reflectivity throughout the profile, suggests that the exponent in the

$D_0 - Z$ power law is biased high in stratiform rain, particularly in the tropics, and that this exponent increases with echo top in convective rain. Meanwhile, positive values of the second mode, which represents profiles with weaker echoes above the melting layer and stronger echoes below it, are correlated with smaller drops at a given reflectivity for both rain types, which is consistent with the stronger influence of warm rain processes in profiles that exhibit this characteristic.

What causes the observed regional bias patterns between the TRMM radar and radiometer algorithms (and GV)? Could these biases potentially mask or exaggerate long-term trends in global precipitation? The regional patterns of the rain DSD for all rain types are generally similar to those presented by [Kozu et al. \(2009\)](#) for convective rain, although absolute values of the $Z - R$ coefficients differ due to the inclusion of stratiform rain in this study. These regional patterns of DSD can be largely explained by patterns in the dynamical, environmental, and microphysical factors that shape DSD. Much of the bias between PR and TMI rain estimates appears to be related to these DSD assumptions via two pathways:

- Insufficient adjustments to the default DSD by the PR 2A25 algorithm, especially in light and moderate rain where surface reference estimates of the path-integrated attenuation do not exceed the noise level, and
- Incorrect assumption of DSD and/or vertical distribution of rain water in the database of profiles used by the GPROF algorithm for TMI, which affects the liquid water content-rain rate conversion.

Globally, the area-weighted mean rain rate from the combined rainfall product exceeds version 6 of the 2A25 products by 15% for the two years analyzed (Figure 6.1). Note, however, that the patterns of rainfall adjustment are nearly identical in going from the default DSD to 2A25 and 2A25 to the combined algorithm. The increase of rainfall in the combined algorithm therefore results from two sources:

- The combined algorithm, unlike the PIA-based 2A25, is not limited to pixels with heavy rain, and
- The majority of rainfall occurs in the regions where DSD adjustments increase rainfall.

A simple sensitivity test was conducted to determine whether trends in TPW, generally considered a robust reponse of the hydrological cycle to greenhouse gas forcing (Held and Soden, 2006), might result in retrieval biases. Without any change in actual rainfall, mean global reflectivity decreases and mean total LWP increases assuming that mean rain properties at a given value of TPW remain constant. This could result in an underestimate by radar algorithms and an overestimate by radiometer algorithms of rainfall trends associated with the increase in TPW.

What is the mean rainfall rate over the tropics and its uncertainty? Is this consistent with estimates derived from the measurements of the other components of the energy budget? The mean tropical oceanic rainfall rate from the combined algorithm was found to be 3.06 mm/day with an uncertainty of about 8%. This value slightly exceeds the GPCP estimate but is not inconsistent with estimates of the global mean value obtained from the residual of other components of the energy budget when their respective uncertainties are considered. Based on energy budget considerations and validation of the combined algorithm, it seems likely that 2A25 estimates are biased low against the actual mean rainfall rate. However, the tropical oceans receive only about half of the global total rainfall, and the other half, which occurs over land and at high latitudes, is not as well constrained by current remote sensing techniques as the values over the tropical ocean. Thus, the uncertainty in the global total from measurements is not much less than the uncertainty that comes from knowledge of other terms in the energy budget.

7.2 Future Work

Potential areas of algorithm refinement include sensitivity analyses to different radiative transfer models and hydrometeor scattering properties, including non-spherical raindrops and more complex representations of ice. More accurate estimates of the global mean rainfall will require additional tuning of the cloud water adjustment and/or DSD assumptions using polarimetric radar data from a variety of rainfall climate regimes. To continue preparation for GPM, a dual-frequency profiling algorithm will need to be developed as well as an extension of the retrieval method over land and ice surfaces.

Much work remains to be done to verify the relationships between DSD the parameters analyzed in chapter 5, and in particular to identify biases in the combined radar-radiometer algorithm that may create

spurious relationships between the DSD adjustment and unrelated factors. Nevertheless, the relationships we have found are consistent with what is known about the processes that shape the rain DSD and may be used to create time-varying Z-R relationships for ground-based radars or to enhance over-land TRMM PR retrievals, where radiometer-enhanced retrievals are complicated by the unknown factors related to surface emissivity and radar-only retrievals must rely on the surface reference estimate of attenuation, which is noisier over land than water. However, it should be emphasized that caution must be used in extending these relationships over land, as some regimes (*e.g.*, orographic precipitation) may be unsampled over the ocean. When the GPM core satellite is launched in 2013, it will carry a dual-frequency radar, reducing much of the ambiguity in DSD retrievals over land and ocean. At that time it will be worthwhile to revisit the relationships noted in this work.

7.3 Concluding Remarks

This dissertation represents the culmination of four years of work distilled into a single document. Not included are the numerous dead ends and otherwise unfruitful avenues that were pursued. Likewise, the constraints of time did not allow a thorough examination of every topic that appeared to be inviting along the way. Fortunately or unfortunately, depending on the perspective of the researcher, the nature of science is such that more questions are raised than answered in almost every study that has been undertaken. It is hoped that this dissertation has answered at least a few such questions, and prompted at least as many to be answered in the future by whomever is willing.

BIBLIOGRAPHY

- Adler, R. F., J.-J. Wang, G. Gu, and G. Huffman, 2009: A ten-year tropical rainfall climatology based on a composite of TRMM products. *J. Met. Soc. Japan*, **87A**, 281–293.
- Adler, R. F., et al., 2003: The version-2 global precipitation climatology project (GPCP) monthly precipitation analysis (1979-present). *J. Hydrometeorology*, **4**, 1147–1167.
- Aguttes, J., J. Schrive, C. Goldstein, M. Rouze, and G. Raju, 2000: Megha-tropiques, a satellite for studying the water cycle and energy exchanges in the tropics. *Geoscience and Remote Sensing Symposium, 2000. Proceedings. IGARSS 2000. IEEE 2000 International*, Vol. 7, 3042–3044 vol.7, doi:10.1109/IGARSS.2000.860329.
- Akihiro, M., T. Nobuhiro, K. Hiroshi, and T. Toyoyuki, 2004: Calibration of the TRMM Precipitation Radar using the Active Radar Calibrator (ARC). *J. Rem. Sens. Soc. Japan*, **24**, 367–377.
- Allen, M. R. and W. J. Ingram, 2002: Constraints on future changes in climate and the hydrologic cycle. *Nature*, **419**, 224–232.
- Allison, L. J., E. B. Rodgers, T. T. Wilheit, and R. W. Fett, 1974: Tropical cyclone rainfall as measured by the nimbus electrically scanning microwave radiometer. *Bull. Amer. Meteor. Soc.*, **55** (9), 1074–1089, doi:10.1175/1520-0477(1974)055<1074:TCRAMB>2.0.CO;2, URL <http://journals.ametsoc.org/doi/abs/10.1175/1520-0477%281974%29055%3C1074%3A>
- Atlas, D. and A. C. Chmela, 1957: Physical-synoptic variations of drop-size parameters. *Proc. 6th Weather Radar Conf.*, Boston, MA, Amer. Meteor. Soc., 21–29.
- Atlas, D. and C. W. Ulbrich, 1977: Path- and area-integrated rainfall measurement by microwave attenuation in the 1.3 cm band. *J. Appl. Meteor.*, **16** (12), 1322–1331, doi:10.1175/1520-0450(1977)016<1322:PAAIRM>2.0.CO;2, URL <http://journals.ametsoc.org/doi/abs/10.1175/1520-0450%281977%29016%3C1322%3A>
- Atlas, D. and C. W. Ulbrich, 2000: An observationally based conceptual model of warm oceanic convective rain in the tropics. *J. Appl. Meteor.*, **39**, 2165–2181.
- Barret, E. C., 1970: The estimation of monthly rainfall from satellite data. *Monthly Weather Review*, **98** (4), 322–327, doi:10.1175/1520-0493(1970)098<0322:TEOMRF>2.3.CO;2, URL <http://journals.ametsoc.org/doi/abs/10.1175/1520-0493%281970%29098%3C0322%3A>
- Battan, L. J., 1973: *Radar Observation of the Atmosphere*. University of Chicago Press, Chicago, 324 pp.
- Beard, K. V., 1976: Terminal velocity and shape of cloud and precipitation drops aloft. *J. Atmos. Sci.*, **33**, 851–864.

- Beard, K. V. and C. Chuang, 1987: A new model for the equilibrium shape of raindrops. *J. Atmos. Sci.*, **44** (11), 1509–1524, doi:10.1175/1520-0469(1987)044<1509:ANMFTE>2.0.CO;2, URL <http://journals.ametsoc.org/doi/abs/10.1175/1520-0469%281987%29044%3C1509%3AA>
- Bennartz, R. and G. W. Petty, 2001: The sensitivity of microwave remote sensing observations of precipitation to ice particle size distributions. *J. Appl. Meteor.*, **40**, 345–364.
- Berg, W., T. L'Ecuyer, and J. M. Haynes, 2010: The distribution of rainfall over oceans from spaceborne radars. *J. Appl. Meteor. and Climatol.*, **49** (3), 535–543, doi:10.1175/2009JAMC2330.1, URL <http://journals.ametsoc.org/doi/abs/10.1175/2009JAMC2330.1>.
- Berg, W., T. L'Ecuyer, and C. Kummerow, 2006: Rainfall climate regimes: the relationship of regional TRMM rainfall biases to the environment. *J. Appl. Meteor. and Climatol.*, **45**, 434–454.
- Black, R. A., 1990: Radar reflectivity-ice water content relationships for use above the melting level in hurricanes. *J. Appl. Meteor.*, **29**, 955–961.
- Bowman, K. P., 2005: Comparison of trmm precipitation retrievals with rain gauge data from ocean buoys. *J. Climate*, **18** (1), 178–190, doi:10.1175/JCLI3259.1, URL <http://journals.ametsoc.org/doi/abs/10.1175/JCLI3259.1>.
- Brandes, E. A., G. Zhang, and J. Sun, 2006: On the influence of assumed drop size distribution form on radar-retrieved thunderstorm microphysics. *J. Appl. Meteor. and Climatol.*, **45** (2), 259–268, doi:10.1175/JAM2335.1, URL <http://journals.ametsoc.org/doi/abs/10.1175/JAM2335.1>.
- Bringi, V. N. and V. Chandrasekhar, 2001: *Polarimetric Doppler Weather Radar*. Cambridge University Press, Cambridge, UK, 636 pp.
- Bringi, V. N., V. Chandrasekhar, J. Hubbert, E. Gorgucci, W. L. Randeu, and M. Schoenhuber, 2003: Raindrop size distribution in different climatic regimes from disdrometer and dual-polarized radar analysis. *J. Atmos. Sci.*, **60**, 354–365.
- Bringi, V. N., T. Tang, and V. Chandrasekar, 2004: Evaluation of a new polarimetrically based Z-R relation. *J. Atmos. Oceanic Technol.*, **21**, 612–623.
- Brown, P. S., 1989: Coalescence and breakup-induced oscillations in the evolution of the raindrop size distribution. *J. Atmos. Sci.*, **46**, 1186–1192.
- Carey, L. D., R. Cifelli, W. A. Petersen, S. A. Rutledge, and M. A. F. S. Dias, 2001: Characteristics of Amazonian rain measured during TRMM-LBA. *30th Conf. on Radar Meteorology*, Munich, Germany, Amer. Meteor. Soc.
- Center for International Earth Science Information Network (CIESIN), Columbia University; and Centro Internacional de Agricultura Tropical (CIAT), 2005: Gridded Population of the World Version 3 (GPWv3): Population Density Grids. Palisades, NY: Socioeconomic Data and Applications Center (SEDAC), Columbia University., URL <http://sedac.ciesin.columbia.edu/gpw>, URL <http://sedac.ciesin.columbia.edu/gpw>.
- Chang, A. T. C., L. S. Chiu, C. Kummerow, J. Meng, and T. T. Wilheit, 1999: First results of the TRMM Microwave Imager (TMI) monthly oceanic rain rate: Comparison with SSM/I. *Geophys. Res. Lett.*, **26** (15), 2379–2382.
- Chen, Y., A. D. D. Genio, and J. Chen, 2007: The tropical atmospheric El Niño signal in satellite precipitation data and a global climate model. *J. Climate*, **20**, 3580–3601.

- Cho, H.-K., K. P. Bowman, and G. R. North, 2004: Equatorial waves including the Madden-Julian oscillation in TRMM rainfall and OLR data. *J. Climate*, **17**, 4387–4406.
- Eccles, P. J. and E. A. Mueller, 1971: X-band attenuation and liquid water content estimation by a dual-wavelength radar. *J. Appl. Meteor.*, **10** (6), 1252–1259, doi:10.1175/1520-0450(1971)010<1252:XBAALW>2.0.CO;2, URL <http://journals.ametsoc.org/doi/abs/10.1175/1520-0450%281971%29010%3C1252%3AXI>
- Elsaesser, G. and C. Kummerow, 2008: Towards a fully parametric retrieval of the non-raining parameters over the global oceans. *J. Appl. Meteor.*, **47**, in press.
- Endter-Wada, J., T. Selfa, and L. W. Welsh, 2009: Hydrologic interdependencies and human cooperation: The process of adapting to droughts. *Weather, Climate, and Society*, **1** (1), 54–70, doi:10.1175/2009WCAS1009.1, URL <http://journals.ametsoc.org/doi/abs/10.1175/2009WCAS1009.1>.
- Fabry, F. and I. Zawadzki, 1995: Long-term radar observations of the melting layer of precipitation and their interpretation. *J. Atmos. Sci.*, **52**, 838–851.
- Fujiwara, M. and T. Yanase, 1968: Raindrop z-r relationships in different altitudes. *Preprints 13th Conf. on Radar Meteorology*, Boston, MA, Amer. Meteor. Soc., 380–383.
- Gentemann, C. L., F. Wentz, C. Mears, and D. Smith., 2004: In-situ validation of TRMM microwave sea surface temperatures. *J. Geophys. Res.*, **109**, C04021.
- Givati, A. and D. Rosenfeld, 2005: Separation between cloud-seeding and air-pollution effects. *J. Appl. Meteor.*, **44**, 1298–1314.
- Gloersen, P. and L. Hardis, 1978: *Scanning multichannel microwave radiometer (SMMR) experiment*. In: Madris, C.R. (ed.) *Nimbus 7 User's Guide*. NASA/GSFC, Greenbelt, MD, 213–245 pp.
- Greco, M. and E. N. Anagnostou, 2002: Use of passive microwave observations in a radar rainfall-profiling algorithm. *J. Appl. Meteor.*, **41**, 702–715.
- Greco, M., W. S. Olson, and E. N. Anagnostou, 2004: Retrieval of precipitation profiles from multiresolution, multifrequency active and passive microwave observations. *J. Appl. Meteor.*, **43**, 562–575.
- Haddad, Z. S., S. L. Durden, and E. Im, 1996: Parameterizing the raindrop size distribution. *J. Appl. Meteor.*, **35**, 3–13.
- Haddad, Z. S., E. A. Smith, and coauthors, 1997: The TRMM ‘Day-1’ radar/radiometer combined rain-profiling algorithm. *J. Meteor. Soc. Japan*, **75**, 799–809.
- Haynes, J. M., T. S. L’Ecuyer, G. L. Stephens, S. D. Miller, C. Mitrescu, N. B. Wood, and S. Tanelli, 2009: Rainfall retrieval over the ocean with spaceborne W-band radar. *J. Geophys. Res.*, **114**, D00A22, doi:10.1029/2008JD009973.
- Haynes, J. M. and G. L. Stephens, 2007: Tropical oceanic cloudiness and the incidence of precipitation: Early results from cloudsat. *Geophys. Res. Lett.*, **34**, L09811.
- Held, I. M. and B. J. Soden, 2006: Robust responses of the hydrological cycle to global warming. *J. Climate*, **19**, 5686–5699.
- Heymsfield, A. J., A. Bansemmer, C. Schmitt, C. Twomey, and M. R. Poellot, 2004: Effective ice particle densities derived from aircraft data. *J. Atmos. Sci.*, **61**, 982–1003.

- Hinton, B. B., W. S. Olson, D. W. Martin, and B. Auvine, 1992: A passive microwave algorithm for tropical oceanic rainfall. *J. Appl. Meteor.*, **31** (12), 1379–1395, doi:10.1175/1520-0450(1992)031<1379:APMAFT>2.0.CO;2, URL <http://journals.ametsoc.org/doi/abs/10.1175/1520-0450%281992%29031%3C1379%3AA>
- Hitschfield, W. and J. Bordan, 1954: Errors inherent in the radar measurement of rainfall at attenuating wavelengths. *J. Meteor.*, **11**, 58–67.
- Hollinger, J. P., J. L. Peirce, and G. A. Poe, 1990: SSM/I instrument evaluation. *IEEE Trans. Geosci. Remote Sensing*, **28**, 781–790.
- Hou, A. Y., et al., 2010: The global precipitation measurement (gpm) mission: An international satellite mission to unify and advance global precipitation measurements for research and applications. *Bull. Amer. Met. Soc.*, **submitted**.
- Houze, R. A., P. V. Hobbs, P. H. Herzegh, and D. B. Parsons, 1979: Size distributions of precipitation particles in frontal clouds. *J. Atmos. Sci.*, **36**, 156–162.
- Hu, Z. and R. Srivastava, 1995: Evolution of the raindrop size distribution by coalescence, breakup, and evaporation: Theory and observations. *J. Atmos. Sci.*, **52**, 1761–1783.
- Huang, R. and K.-N. Liou, 1983: Polarized microwave radiation transfer in precipitating cloudy atmospheres: Applications to window frequencies. *J. Geophys. Res.*, **88** (C6), 3885–3893.
- Huffman, G. J., et al., 1997: The global precipitation climatology project (gpcp) combined precipitation dataset. *Bull. Amer. Meteor. Soc.*, **78** (1), 5–20, doi:10.1175/1520-0477(1997)078<0005:TGPCPG>2.0.CO;2, URL <http://journals.ametsoc.org/doi/abs/10.1175/1520-0477%281997%29078%3C0005%3AT>
- Iguchi, T., T. Kozu, J. Kwiatkowski, R. Meneghini, J. Awaka, and K. Okamoto, 2009: Uncertainties in the rain profiling algorithm for the TRMM precipitation radar. *J. Met. Soc. Japan*, **87A**, 1–30.
- Iguchi, T., T. Kozu, R. Meneghini, J. Awaka, and K. Okamoto, 2000: Rain-profiling algorithm for the TRMM precipitation radar. *J. Appl. Meteor.*, **39**, 2038–2052.
- Jameson, A. R., A. B. Kostinski, and A. Kruger, 1999: Fluctuation properties of precipitation. part iv: Finescale clustering of drops in variable rain. *J. Atmos. Sci.*, **56** (1), 82–91, doi:10.1175/1520-0469(1999)056<0082:FPOPPI>2.0.CO;2, URL <http://journals.ametsoc.org/doi/abs/10.1175/1520-0469%281999%29056%3C0082%3AF>
- Kawanishi, T., et al., 2003: The advanced microwave scanning radiometer for the earth observing system (amsr-e), nasda's contribution to the eos for global energy and water cycle studies. *Geoscience and Remote Sensing, IEEE Transactions on*, **41** (2), 184 – 194, doi:10.1109/TGRS.2002.808331.
- Keeler, R. J., B. W. Lewis, and G. R. Gray, 1989: Description of NCAR/FOF CP-2 meteorological Doppler radar. *Proc. 24th Conf. on Radar Meteorology*, Tallahassee, FL, Amer. Meteor. Soc., 589–592.
- Kozu, T., T. Iguchi, T. Kubota, N. Yoshida, S. Seto, J. Kwiatkowski, and Y. N. Takayabu, 2009: Feasibility of raindrop size distribution parameter estimation with TRMM precipitation radar. *J. Met. Soc. Japan*, **87A**, 53–66.
- Kubar, T. L., D. L. Hartmann, and R. Wood, 2009: Understanding the importance of microphysics and macrophysics for warm rain in marine low clouds - Part I. Satellite observations. *J. Atmos. Sci.*, **66**, 2953–2972.

- Kummerow, C., 1993: On the accuracy of the eddington approximation for radiative transfer in the microwave frequencies. *J. Geophys. Res.*, **98**, 2757–2765.
- Kummerow, C., W. Barnes, T. Kozu, J. Shiue, and J. Simpson, 1998: The Tropical Rainfall Measuring Mission (TRMM) Sensor Package. *J. Atmos. Oceanic Technol.*, **15**, 809–817.
- Kummerow, C., W. Berg, J. Thomas-Stahle, and H. Masunaga, 2006: Quantifying global uncertainties in a simple microwave rainfall algorithm. *J. Atmos. Oceanic Technol.*, **23** (1), 23–37, doi:10.1175/JTECH1827.1, URL <http://journals.ametsoc.org/doi/abs/10.1175/JTECH1827.1>.
- Kummerow, C. and L. Giglio, 1994: A passive microwave technique for estimating rainfall and vertical structure information from space. Part I: Algorithm description. *J. Appl. Meteor.*, **33**, 3–18.
- Kummerow, C., W. Olson, and L. Giglio, 1996: A simplified scheme for obtaining precipitation and vertical hydrometeor profiles from passive microwave sensors. *IEEE Trans. Geosci. Remote Sens.*, **34** (5), 1213–1232, doi:10.1109/36.536538.
- Kummerow, C. and J. A. Weinman, 1988: Determining microwave brightness temperatures from precipitating horizontally finite and vertically structured clouds. *J. Geophys. Res.*, **93** (D4), 3720–3728.
- Kummerow, C., et al., 2001: The evaluation of the Goddard Profiling Algorithm (GPROF) for rainfall estimation from passive microwave sensors. *J. Appl. Meteor.*, **40**, 1801–1820.
- Kummerow, C. D., S. Ringerud, J. Crook, D. Randel, and W. Berg, 2010: An observationally generated a-priori database for microwave rainfall retrievals. *J. Atmos. Oceanic Technol.*, in review.
- Lang, T. J., S. A. Rutledge, and R. Cifelli, 2010: Polarimetric radar observations of convection in northwestern Mexico during the North American Monsoon Experiment. *J. Hydrometeor.*, accepted.
- Lau, K.-M. and H.-T. Wu, 2006: Detecting trends in tropical rainfall characteristics, 1979–2003. *International J. of Climatol.*, **27**, 979–988.
- L'Ecuyer, T., H. Masunaga, and C. Kummerow, 2006: Variability in the characteristics of precipitation systems in the tropical Pacific. Part II: implications for atmospheric heating. *J. Climate*, **19**, 1388–1406.
- L'Ecuyer, T. S., C. Kummerow, and W. Berg, 2004: Toward a global map of raindrop size distributions. part i: Rain-type classification and its implications for validating global rainfall products. *Journal of Hydrometeorology*, **5** (5), 831–849, doi:10.1175/1525-7541(2004)005<0831:TAGMOR>2.0.CO;2, URL <http://journals.ametsoc.org/doi/abs/10.1175/1525-7541%282004%29005%3C0831%3A>
- L'Ecuyer, T. S. and G. L. Stephens, 2002a: An estimation-based precipitation retrieval algorithm for attenuating radars. *J. Appl. Meteor.*, **41** (3), 272–285, doi:10.1175/1520-0450(2002)041<0272:AEBPRA>2.0.CO;2, URL <http://journals.ametsoc.org/doi/abs/10.1175/1520-0450%282002%29041%3C0272%3A>
- L'Ecuyer, T. S. and G. L. Stephens, 2002b: An uncertainty model for Bayesian Monte Carlo retrieval algorithms: Application to the TRMM observing system. *Quarterly Journal of the Royal Meteorological Society*, **128**, 1713–1737, doi:10.1002/qj.200212858316.
- L'Ecuyer, T. S. and G. L. Stephens, 2007: The tropical atmospheric energy budget from the TRMM perspective. Part II: Evaluating GCM representations of the sensitivity of regional energy and water cycles to the 1998–99 ENSO cycle. *J. Climate*, **20**, 4548–4571.

- Lee, C. K., G. W. Lee, I. Zawadzki, and K.-E. Kim, 2009: A preliminary analysis of spatial variability of raindrop size distributions during stratiform rain events. *J. Appl. Meteor. and Climatol.*, **48** (2), 270–283, doi:10.1175/2008JAMC1877.1, URL <http://journals.ametsoc.org/doi/abs/10.1175/2008JAMC1877.1>.
- Li, Y., E. J. Zipser, S. K. Krueger, and M. A. Zulauf, 2008: Cloud-resolving modeling of deep convection during kwajex. part i: Comparison to trmm satellite and ground-based radar observations. *Monthly Weather Review*, **136** (7), 2699–2712, doi:10.1175/2007MWR2258.1.
- List, R., T. B. Low, N. Donaldson, E. Freire, and J. R. Gillespie, 1987: Temporal evolution of drop spectra to collisional equilibrium in steady and pulsating rain. *J. Atmos. Sci.*, **44**, 362–372.
- Liu, Y. and P. H. Daum, 2004: Parameterization of the autoconversion process. Part I: Analytical formulation of Kessler-type parameterizations. *J. Atmos. Sci.*, **61**, 1539–1548.
- Marks, D. A., D. B. Wolff, D. S. Silberstein, A. Tokay, J. L. Pippitt, and J. Wang, 2009: Availability of high-quality TRMM ground validation data from Kwajalein, RMI: A practical application of the relative calibration adjustment technique. *J. Atmos. Oceanic Technol.*, **26**, 413–429.
- Marshall, J. and W. M. Palmer, 1948: The distribution of raindrops with size. *J. Meteor.*, **5**, 165–166.
- Marshall, J. S., R. C. Langille, and W. M. K. Palmer, 1947: Measurement of rainfall by radar. *J. Meteor.*, **4** (6), 186–192, doi:10.1175/1520-0469(1947)004<0186:MORBR>2.0.CO;2, URL <http://journals.ametsoc.org/doi/abs/10.1175/1520-0469%281947%29004%3C0186%3AM>
- Masunaga, H. and C. Kummerow, 2005: Combined radar and radiometer analysis of precipitation profiles for a parametric retrieval algorithm. *J. Atmos. Oceanic Technol.*, **22**, 909–929.
- Masunaga, H., T. S. L'Ecuyer, and C. D. Kummerow, 2006: The Madden-Julian Oscillation recorded in early observations from the Tropical Rainfall Measuring Mission (TRMM). *J. Atmos. Sci.*, **63**, 2777–2794.
- Matrosov, S. Y., K. Clark, B. Martner, and A. Tokay, 2002: X-Band polarimetric radar measurements of rainfall. *J. Appl. Meteor.*, **41**, 941–952.
- May, P. T., J. H. Mather, G. Vaughan, K. N. Bower, C. Jakob, G. M. McFarquhar, and G. G. Mace, 2008: The tropical warm pool international cloud experiment. *Bull. Amer. Meteor. Soc.*, **89** (5), 629–645, doi:10.1175/BAMS-89-5-629, URL <http://journals.ametsoc.org/doi/abs/10.1175/BAMS-89-5-629>.
- McKague, D., K. F. Evans, and S. Avery, 1998: Assessment of the effects of drop size distribution variations retrieved from uhf radar on passive microwave remote sensing of precipitation. *J. Appl. Meteor.*, **37** (2), 155–165, doi:10.1175/1520-0450(1998)037<0155:AOTEOD>2.0.CO;2, URL <http://journals.ametsoc.org/doi/abs/10.1175/1520-0450%281998%29037%3C0155%3AA>
- Meneghini, R., J. Eckerman, and D. Atlas, 1983: Determination of rain rate from a spaceborne radar using measurements of total attenuation. *Geoscience and Remote Sensing, IEEE Transactions on*, **GE-21** (1), 34–43, doi:10.1109/TGRS.1983.350528.
- Meneghini, R., T. Iguchi, T. Kozu, L. Liao, K. Okamoto, J. A. Jones, and J. Kwiatkowski, 2000: Use of the surface reference technique for path attenuation estimates from the TRMM radar. *J. Appl. Meteor.*, **39**, 2053–2070.
- Mie, G., 1908: Beitrage zur optik truber medien, speziell kolloidaler metallosungen. *Ann. Physik*, **25**, 377–445.

- Mitrescu, C. and G. L. Stephens, 2002: A new method for determining cloud transmittance and optical depth using the ARM micropulsed lidar. *J. Atmos. Oceanic Technol.*, **19** (7), 1073–1081, doi:10.1175/1520-0426(2002)019<1073:ANMFDC>2.0.CO;2, URL <http://journals.ametsoc.org/doi/abs/10.1175/1520-0426%282002%29019%3C1073%3AA>
- Morita, J., Y. N. Takayabu, S. Shige, and Y. Kodama, 2006: Analysis of rainfall characteristics of the Madden-Julian oscillation using TRMM satellite data. *Dyn. Atmos. Oceans*, **42**, 107–126.
- Mugnai, A., E. A. Smith, and G. J. Tripoli, 1993: Foundation of physical-statistical precipitation retrieval from passive microwave satellite measurements. Part II: Emission source and generalized weighting function properties of a time-dependent cloud-radiation model. *J. Appl. Meteor.*, **32**, 17–39.
- Munchak, S. J. and C. D. Kummerow, 2010: A modular optimal estimation method for combined radar-radiometer precipitation profiling. *J. Appl. Meteor. Climatol.*, submitted.
- Munchak, S. J., C. D. Kummerow, and T. Lang, 2010: Relationships between the raindrop size distribution and properties of the environment and clouds inferred from trmm observations. *J. Climate*, submitted.
- Munchak, S. J. and A. Tokay, 2008: Retrieval of raindrop size distribution from simulated dual-frequency radar measurements. *J. Appl. Meteor. Climatol.*, **47**, 223–239.
- Nakajima, T. and M. D. King, 1990: Determination of the optical thickness and effective particle radius of clouds from reflected solar radiation measurements. Part I: Theory. *J. Atmos. Sci.*, **47**, 1878–1893.
- Olson, W. S., P. Bauer, N. F. Viltard, D. E. Johnson, W.-K. Tao, R. Meneghini, and L. Liao, 2001: A melting-layer model for passive/active microwave remote sensing applications. Part I: Model formulation and comparison with observations. *J. Appl. Meteor.*, **40**, 1145–1163.
- Petty, G. W., 2001: Physical and microwave radiative properties of precipitating clouds. part i: Principal component analysis of observed multichannel microwave radiances in tropical stratiform rainfall. *J. Appl. Meteor.*, **40** (12), 2105–2114, doi:10.1175/1520-0450(2001)040<2105:PAMRPO>2.0.CO;2, URL <http://journals.ametsoc.org/doi/abs/10.1175/1520-0450%282001%29040%3C2105%3AP>
- Petty, G. W. and W. Huang, 2010: Microwave backscatter and extinction by soft ice spheres and complex snow aggregates. *J. Atmos. Sci.*, **67** (3), 769–787, doi:10.1175/2009JAS3146.1.
- Prabhakara, C., D. A. Short, W. Wiscombe, R. S. Fraser, and B. E. Vollmer, 1986: Rainfall over oceans inferred from nimbus 7 smmr: Application to 1982?83 el nio. *J. Climate and Applied Meteorology*, **25** (10), 1464–1474, doi:10.1175/1520-0450(1986)025<1464:ROOIFN>2.0.CO;2, URL <http://journals.ametsoc.org/doi/abs/10.1175/1520-0450%281986%29025%3C1464%3AR>
- Prat, O. P. and A. P. Barros, 2007: A robust numerical solution of the stochastic collection?breakup equation for warm rain. *J. Appl. Meteor. and Climatol.*, **46** (9), 1480–1497, doi:10.1175/JAM2544.1, URL <http://journals.ametsoc.org/doi/abs/10.1175/JAM2544.1>.
- Pruppacher, H. R. and J. D. Klett, 1997: *Microphysics of Clouds and Precipitation*. Kluwer Academic Publishers, 954 pp.
- Rapp, A. D., M. Lebsock, and C. Kummerow, 2009: On the consequences of resampling microwave radiometer observations for use in retrieval algorithms. *J. Appl. Meteor. Climatol.*, **48**, 1981–1993.
- Reynolds, R. W. and T. Smith, 1994: Improved global sea surface temperature analyses using optimum interpolation. *J. Climate*, **7**, 929–948.

- Rodgers, C. D., 2000: *Inverse Methods for Atmospheric Sounding: Theory and Practice*. World Scientific Publishing Co., Singapore, 238 pp.
- Rosenfeld, D., 2000: Suppression of rain and snow by urban and industrial air pollution. *Science*, **287**, 1793–1796.
- Rosenfeld, D. and I. M. Lensky, 1998: Satellite-based insights into precipitation formation processes in continental and maritime convective clouds. *Bull. Amer. Meteor. Soc.*, **79**, 2457–2476.
- Rosenfeld, D. and C. W. Ulbrich, 2003: Cloud microphysical properties, processes and rainfall estimation opportunities. *Radar and Atmospheric Science: A Collection of Essays in Honor of David Atlas, Meteor. Monogr. No. 52*, Amer. Meteor. Soc., 237–258.
- Schafer, R., S. Avery, P. May, D. Rajopadhyaya, and C. Williams, 2002: Estimation of rainfall drop size distributions from dual-frequency wind profiler spectra using deconvolution and a nonlinear least squares fitting technique. *J. Atmos. Oceanic Technol.*, **19**, 864–874.
- Seo, E.-K., B.-J. Sohn, and G. Liu, 2007: How TRMM precipitation radar and microwave imager retrieved rain rates differ. *Geophys. Res. Lett.*, **67**, 1226–1232.
- Shimizu, S., R. Oki, T. Tagawa, T. Iguchi, and M. Hirose, 2009: Effects of the orbit boost of the TRMM satellite on PR rain estimates. *J. Met. Soc. Japan*, **87A**, 83–92.
- Silberstein, D. S., D. B. Wolff, D. A. Marks, D. Atlas, and J. L. Pippitt, 2008: Ground clutter as a monitor of radar stability at Kwajalein, RMI. *J. Atmos. Oceanic Technol.*, **25**, 2037–2045.
- Simpson, J., R. F. Adler, and G. R. North, 1988: A proposed tropical rainfall measuring mission (trmm) satellite. *Bull. Amer. Meteor. Soc.*, **69** (3), 278–295, doi:10.1175/1520-0477(1988)069<0278:APTRMM>2.0.CO;2, URL <http://journals.ametsoc.org/doi/abs/10.1175/1520-0477%281988%29069%3C0278%3AAB>
- Smith, E. A., X. Xiang, A. Mugnai, R. E. Hood, and R. W. Spencer, 1994: Behavior of an inversion-based precipitation retrieval algorithm with high-resolution ampr measurements including a low-frequency 10.7-ghz channel. *J. Atmos. Oceanic Technol.*, **11** (4), 858–873, doi:10.1175/1520-0426(1994)011<0858:BOAIBP>2.0.CO;2, URL <http://journals.ametsoc.org/doi/abs/10.1175/1520-0426%281994%29011%3C0858%3ABO>
- Spencer, R. W., 1986: A satellite passive 37-ghz scattering-based method for measuring oceanic rain rates. *J. Climate and Applied Meteorology*, **25** (6), 754–766, doi:10.1175/1520-0450(1986)025<0754:ASPGSB>2.0.CO;2, URL <http://journals.ametsoc.org/doi/abs/10.1175/1520-0450%281986%29025%3C0754%3AAS>
- Stephens, G. L. and T. D. Ellis, 2008: Controls of global-mean precipitation increases in global warming gcm experiments. *J. Climate*, **21** (23), 6141–6155, doi:10.1175/2008JCLI2144.1, URL <http://journals.ametsoc.org/doi/abs/10.1175/2008JCLI2144.1>.
- Stephens, G. L., D. G. Vane, and coauthors, 2002: The Cloudsat mission and the A-train. *Bull. Amer. Meteor. Soc.*, **83**, 1771–1790.
- Stith, J. L., J. E. Dye, A. Bansemer, A. J. Heymsfield, C. A. Grainger, W. A. Petersen, and R. Cifelli, 2002: Microphysical observations of tropical clouds. *J. Appl. Meteor.*, **41**, 97–117.
- Takemura, T., H. Okamoto, Y. Maruyama, A. Numaguti, A. Higurashi, and T. Nakajima, 2000: Global three-dimensional simulation of aerosol optical thickness distribution of various origins. *J. Geophys. Res.*, **105**, 17 853–17 873.

- Tapiador, F. J., R. Checa, and M. de Castro, 2010: An experiment to measure the spatial variability of rain drop size distribution using sixteen laser disdrometers. *Geophys. Res. Lett.*, **37**, in press, doi:doi:10.1029/2010GL044120.
- Testud, J., S. Oury, R. Black, P. Amayenc, and X. Dou, 2001: The concept of "normalized" distribution to describe raindrop spectra: A tool for cloud physics and remote sensing. *J. Appl. Meteor.*, **40**, 1118–1140.
- Tokay, A. and P. G. Bashor, 2010: An experimental study of small-scale variability of raindrop size distribution. *J. Appl. Meteor. and Climatol.*, **49**, in press, doi:10.1175/2010JAMC2269.1, URL <http://journals.ametsoc.org/doi/abs/10.1175/2010JAMC2269.1>.
- Tokay, A. and D. A. Short, 1996: Evidence from tropical raindrop spectra of the origin of rain from stratiform versus convective clouds. *J. Appl. Meteor.*, **35**, 1671–1687.
- Tokay, A., D. B. Wolff, K. R. Wolff, and P. Bashor, 2003: Rain gauge and disdrometer measurements during the Keys Area Microphysics Project (KAMP). *J. Atmos. Oceanic Technol.*, **20**, 1460–1477.
- Trenberth, K. E., J. T. Fasullo, and J. Kiehl, 2009: Earth's global energy budget. *Bull. Amer. Meteor. Soc.*, **90** (3), 311–323, doi:10.1175/2008BAMS2634.1, URL <http://journals.ametsoc.org/doi/abs/10.1175/2008BAMS2634.1>.
- Trenberth, K. E., J. T. Fasullo, and L. Smith, 2005: Trends and variability in column-integrated atmospheric water vapor. *Clim. Dynamics*, **24** (7-8), 741–758, doi:10.1007/s00382-005-0017-4.
- Ulbrich, C. W., 1983: Natural variations in the analytical form of the drop size distribution. *J. Climate Appl. Meteor.*, **22**, 1764–1775.
- van den Heever, S. C., G. G. Carri, W. R. Cotton, P. J. Demott, and A. J. Prenni, 2006: Impacts of nucleating aerosol on florida storms. Part I: Mesoscale simulations. *J. Atmos. Sci.*, **63**, 1752–1775.
- Waldvogel, A., 1974: The n_0 jump of raindrop spectra. *J. Atmos. Sci.*, **31**, 1067–1078.
- Weiss, B., 1982: The decline of Late Bronze Age civilization as a possible response to climatic change. *Climatic Change*, **4**, 173–198.
- Wentz, F. J., L. Ricciardulli, K. Hilburn, and C. Mears, 2007: How much more rain will global warming bring? *Science*, **317**, 233–235.
- Wilheit, T. T., 1986: Some comments on passive microwave measurement of rain. *Bull. Amer. Meteor. Soc.*, **67**, 1226–1232.
- Wilheit, T. T., V. Chandrasekhar, and W. Li, 2007: Impact of uncertainty in the drop size distribution on oceanic rainfall retrievals from passive microwave observations. *IEEE Trans. Geosci. Remote Sensing*, **45**, 3160–3164.
- Wilheit, T. T., A. T. C. Chang, and L. S. Chiu, 1991: Retrieval of monthly rainfall indices from microwave radiometric measurements using probability distribution functions. *J. Atmos. Oceanic Technol.*, **8** (1), 118–136, doi:10.1175/1520-0426(1991)008<0118:ROMRIF>2.0.CO;2, URL <http://journals.ametsoc.org/doi/abs/10.1175/1520-0426%281991%29008%3C0118%3AR>
- Wilheit, T. T., A. T. C. Chang, M. S. V. Rao, E. B. Rodgers, and J. S. Theon, 1977: A satellite technique for quantitatively mapping rainfall rates over the oceans. *J. Appl. Meteor.*, **16** (5), 551–560, doi:10.1175/1520-0450(1977)016<0551:ASTFQM>2.0.CO;2, URL <http://journals.ametsoc.org/doi/abs/10.1175/1520-0450%281977%29016%3C0551%3AA>

- Williams, C. R., 2008: Profiler DSD estimates and uncertainties retrieved using ensemble statistics and optimal estimation theory. *3rd International TRMM conference*, Las Vegas, NV, available online at http://trmm.gsfc.nasa.gov/3rd_trmm_conf/program_v1b.html.
- Williams, C. R., W. L. Ecklund, and K. S. Gage, 1995: Classification of precipitating clouds in the tropics using 915-MHz wind profilers. *J. Atmos. Oceanic Technol.*, **12**, 996–1012.
- Williams, C. R. and K. S. Gage, 2009: Raindrop size distribution variability estimated using ensemble statistics. *Ann. Geophys.*, **27**, 555–567.
- Wolff, D. B. and B. L. Fisher, 2008: Comparisons of instantaneous TRMM ground validation and satellite rain-rate estimates at different spatial scales. *J. Appl. Meteor. Climatol.*, **47**, 2215–2237.
- Wolff, D. B., D. A. Marks, and coauthors, 2005: Ground validation for the Tropical Rainfall Measuring Mission (TRMM). *J. Atmos. Oceanic Technol.*, **22**, 365–380.
- Wu, R. and J. A. Weinman, 1984: Microwave radiances from precipitating clouds containing aspherical ice, combined phase, and liquid hydrometeors. *J. Geophys. Res.*, **89 (D5)**, 7170–7178.
- Yang, D., B. E. Goodison, J. R. Metcalfe, V. S. Golubev, R. Bates, T. Pangburn, and C. L. Hanson, 1998: Accuracy of nws 8standard nonrecording precipitation gauge: Results and application of wmo intercomparison. *J. Atmos. Oceanic Technol.*, **15 (1)**, 54–68, doi:10.1175/1520-0426(1998)015<0054:AONSNP>2.0.CO;2, URL <http://journals.ametsoc.org/doi/abs/10.1175/1520-0426%281998%29015%3C0054%3AA>
- Zawadzki, I., W. Szyrmer, C. Bell, and F. Fabry, 2005: Modeling of the melting layer. Part III: The density effect. *J. Atmos. Sci.*, **62**, 3705–3722.

Appendix A

COVARIANCE STRUCTURE OF THE RAIN DSD

An important element of the optimal estimation inversion is the *a priori* covariance matrix \mathbf{S}_a . When retrieving the parameter ϵ_{DSD} in multiple pixels within a scene as described in chapter 3, knowledge of the covariance structure of this parameter provides an additional useful constraint. Although DSD parameters similar to ϵ_{DSD} have been defined in previous algorithms (*e.g.*, [Iguchi et al. \(2000\)](#), [Greco et al. \(2004\)](#)), studies of the spatial covariance of the DSD tend to focus on first-order parameters such as rain rate and reflectivity (*e.g.*, [Lee et al. \(2009\)](#), [Tokay and Bashor \(2010\)](#), [Tapiador et al. \(2010\)](#)) instead of reflectivity-normalized quantities such as ϵ_{DSD} . Thus, an important element of algorithm development was determining these covariances using observational data. The datasets and analysis method are described in sections [A.1](#) and [A.2](#)

A.1 Datasets

In order to satisfy the requirements for the covariance structure, simultaneous DSD measurements or estimates over a region at least as large as a 10 GHz TMI FOV (approximately 40×60 km) were desirable. Although no direct DSD measurements from disdrometers are currently available over such a large region (an experiment of this scale is planned as part of GPM ground validation), polarimetric radar retrievals are able to provide reasonably accurate estimates of Z and D_0 , which are required to calculate ϵ_{DSD} . The dataset developed by [Matrosov et al. \(2002\)](#) contains retrievals of rain rate, liquid water content and D_0 (Figure [A.1](#)) from dual-polarized X-band radar located on Wallops Island, VA. The higher frequency of this radar allows for a better determination of drop sizes in light rainfall than S-band radars. Ten rainfall cases were available for study and are listed in Table [A.1](#)

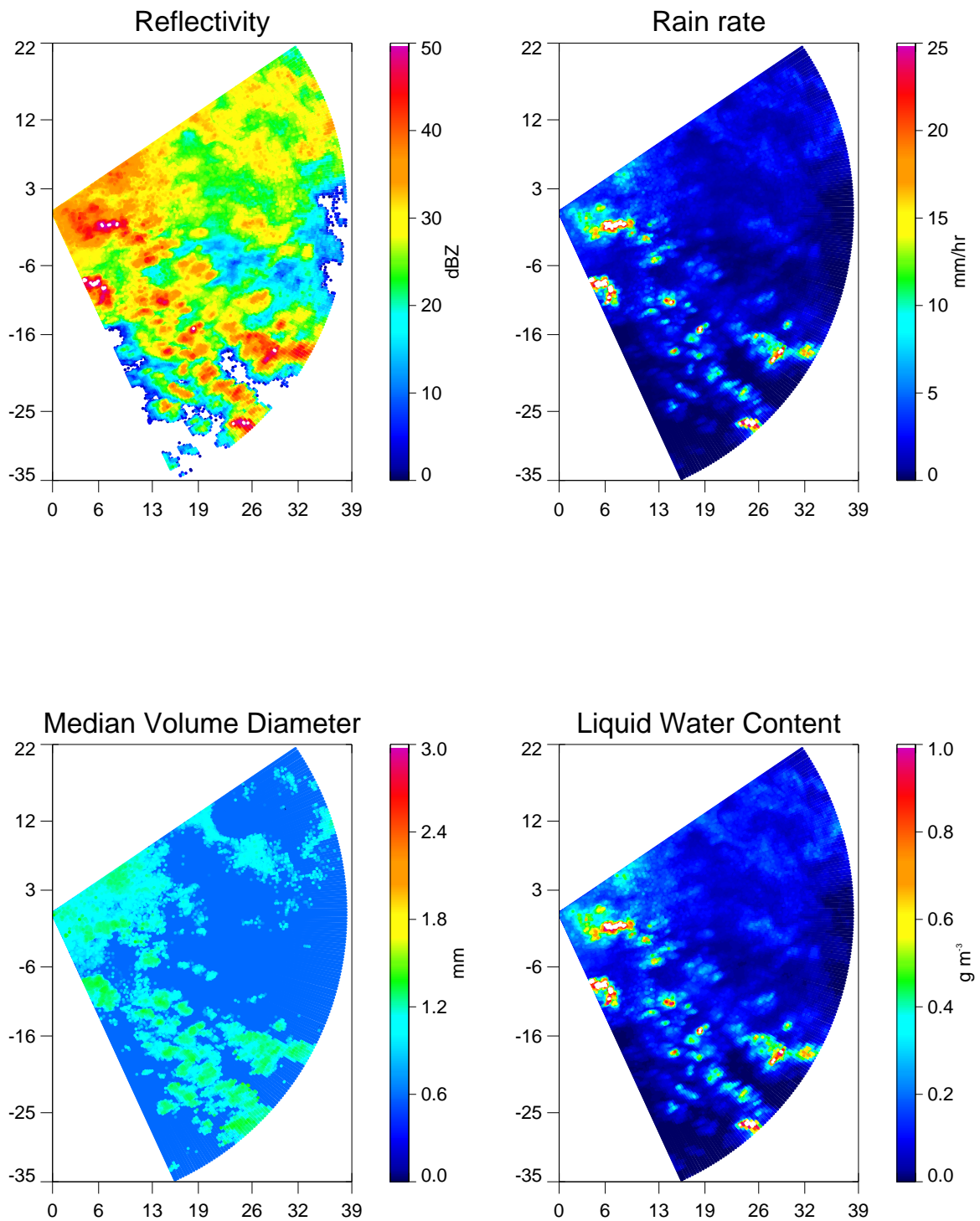


Figure A.1: Reflectivity, rain rate, D_0 , and W for the 11 April 2001 event at Wallops Island.

Table A.1: Rainfall events in Z-band polarimetric dataset from Wallops Island, VA (Matrosov et al., 2002). For each event linear regression was used to derive a $Z - D_0$ power law. Mean conditional rain rate is also given.

Starting Date	Time (UTC)	a (mm) in $D_0 = aZ^b$	b in $D_0 = aZ^b$	$\langle R \rangle$ (mm hr ⁻¹)
25 Feb 2001	1720-2017	0.39	0.136	1.17
4 Mar 2001	2316-0140	0.37	0.115	0.75
13 Mar 2001	0409-2036	0.27	0.146	1.10
15 Mar 2001	1900-2138	0.29	0.168	1.64
21 Mar 2001	1217-1445	0.32	0.156	0.62
30 Mar 2001	0908-1135	0.30	0.155	0.34
1 Apr 2001	2100-2331	0.50	0.076	2.83
11 Apr 2001	0400-1645	0.28	0.177	1.35
16 Apr 2001	0010-0135	0.28	0.183	0.93
17 Apr 2001	0730-0910	0.62	0.042	0.80

In addition to the dual-polarimetric retrievals, a dataset of DSD profiles from the Tropical Warm Pool International Cloud Experiment (TWP-ICE; May et al. (2008)) were also available for analysis. The profiler retrieval method converts 920 MHz Doppler spectra of fall speeds to the DSD with a correction for clear-air turbulence provided by an additional measurement at a different frequency (Schafer et al., 2002). Thus, no *a priori* assumption about the DSD shape is required and full spectra can be theoretically retrieved. Williams and Gage (2009) used a methodology that determined the best-fit gamma DSD to the data, and from this were able to calculate rain rate and D_0 (Figure A.2). These data, although limited to a few rain events (Table A.2), represent some of the most robust measurements of the vertical profile of DSD in deep tropical rain and can therefore be used to test *a priori* assumptions about the vertical structure of ϵ_{DSD} .

Table A.2: Rainfall events analyzed by a 920-MHz profiler in Darwin, Australia during TWP-ICE.. For each event linear regression was used to derive a $Z - D_0$ power law. Mean conditional rain rate is also given.

Starting Date	Time (UTC)	a (mm) in $D_0 = aZ^b$	b in $D_0 = aZ^b$	$\langle R \rangle$ (mm hr ⁻¹)
19 Jan 2006	2300-0600	0.70	0.098	8.81
22 Jan 2006	1000-1700	0.93	0.074	1.54
23 Jan 2006	1000-2359	0.85	0.075	6.55

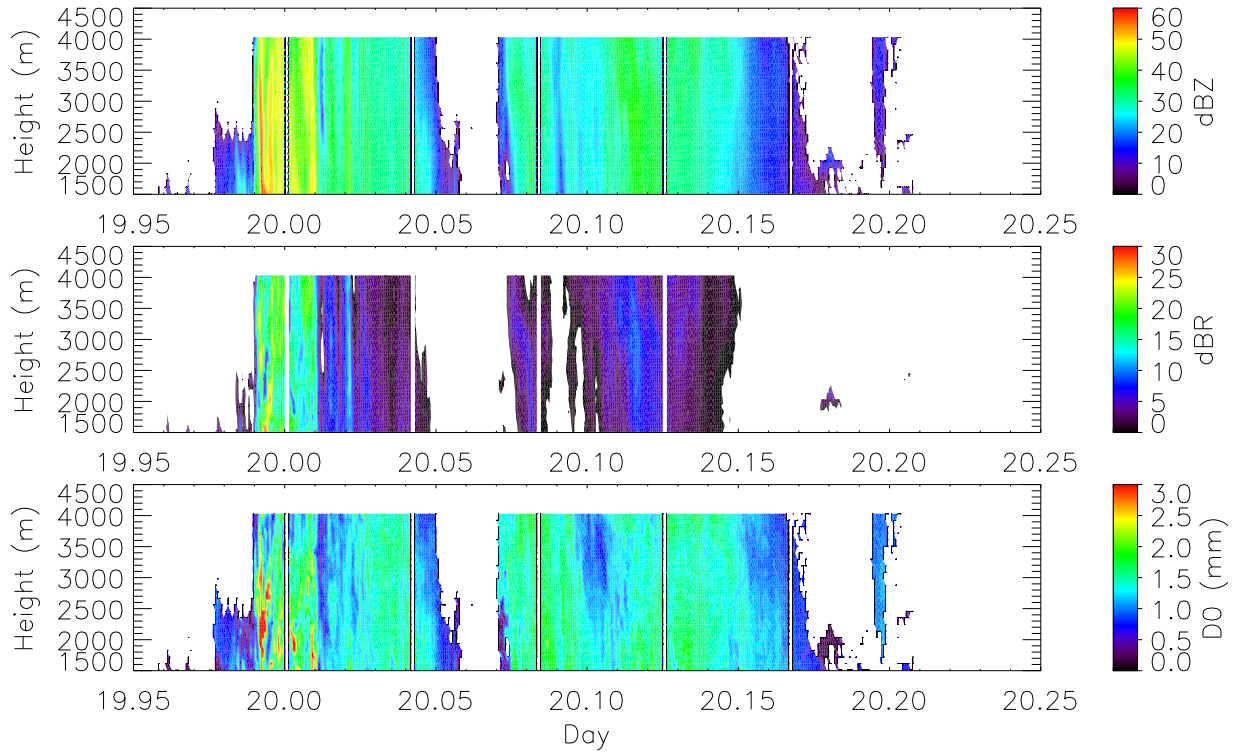


Figure A.2: Reflectivity, rain rate, and D_0 for the 19 January 2006 event at Darwin.

A.2 Analysis

The X-band polarimetric data were first averaged to a 1 km grid to reduce noise and speed computations. For each day, linear regression was used to calculate the $Z - D_0$ power law coefficients. Next, D_0^* (equivalent to ϵ_{DSD}) was calculated at each grid cell by dividing the retrieved D_0 value by the value predicted by the power law and Z . The resulting grid of D_0^* was then analyzed for covariances using the following procedure: First, pairs of grid cells within a radar scan were grouped by distance and reflectivity difference. These variables were first considered separately, then together. The covariance of D_0^* of all pairs in each group was then calculated. Next, an average covariance at each distance and/or reflectivity difference is calculated for each day, weighted by the number of pairs that went into each covariance. These weighted mean covariances were observed to follow an inverse exponential decrease with distance and/or reflectivity difference:

$$C(\Delta s) = C_{0s} e^{-\Delta s/L_0}, \quad (\text{A.1})$$

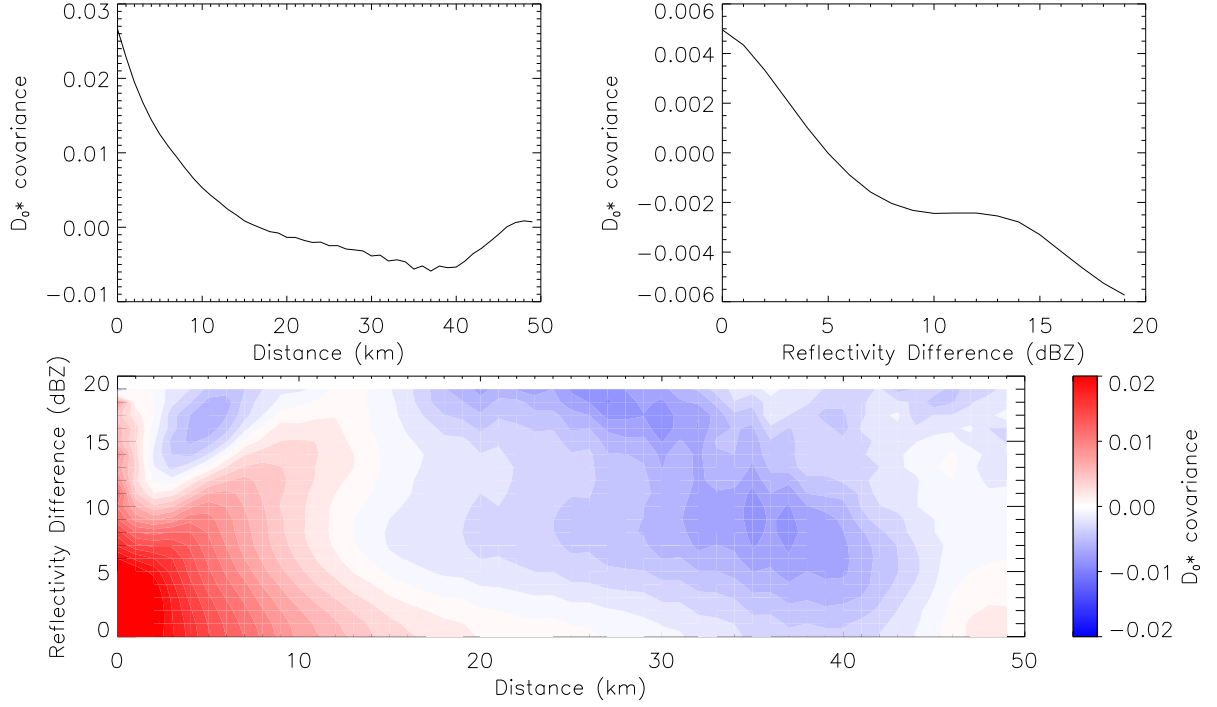


Figure A.3: Covariance structure of D_0^* as a function of distance and reflectivity difference.

$$C(\Delta Z) = C_{0z} e^{-\Delta Z/Z_0}, \quad (\text{A.2})$$

and

$$C(\Delta s, \Delta Z) = C_{0sz} e^{-\Delta Z/Z_1 - \Delta s/L_1}, \quad (\text{A.3})$$

When all events are averaged together, these patterns become quite clear (Figure A.3). The best-fit length and reflectivity scales for the individual variables are 12.6 km and 2.6 dBZ. For the combined function (Eq. A.3), these scales are 12.4 km and 8.7 dBZ.

The profiler data lend themselves to a similar analysis with one important difference: they represent precipitation propagating over a stationary point. Since this precipitation may evolve in time, any time scales derived from this dataset may represent temporal covariances as well. Presumably, these effects would average out over many cases but with such a small sample size, results should be treated with suspicion. Nevertheless, a similar analysis was performed on the 920 MHz profiler DSDs retrieved from Darwin during TWP-ICE. The vertical profiles offer the opportunity to perform an additional analysis to determine the mean vertical profile of D_0^* and its vertical covariance structure (Figure A.4).

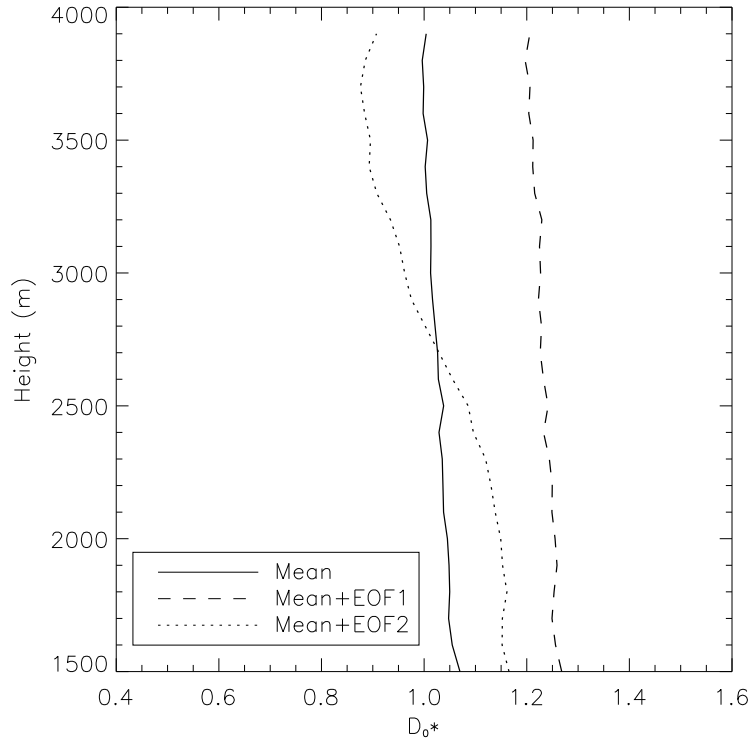


Figure A.4: Mean and two leading EOFs of D_0^* from the Darwin profiler data.

Since the vertical variations in Z , D_0 , and D_0^* are small compared to their horizontal variations, an average of each profile was taken and used to compute the time scale for each event. The average value among all events was an e-folding time of 15 minutes, corresponding to 7.2 km assuming a propagation speed of 8 m s^{-1} .

Appendix B

RESIDUAL ERRORS

This appendix contains a quantitative description and maps of the residual brightness temperatures errors, expressed as the difference between the observed T_b and simulated T_b . The data come from the 2 years of TRMM retrievals described in chapter 5. The purpose of this appendix is to highlight the patterns in these residual errors in order to identify areas where the combined algorithm could be improved. Some summary statistics are provided in section B.1 and maps of biases are presented in section B.2

B.1 Summary Statistics

The mean residual T_b root-mean-square error and bias for the vertically polarized channels are plotted in Figure B.1. The emission channels all generally have negative errors which increase in magnitude as rain rate and rain fraction within the FOV increase, although saturation effects reduce these errors at higher rain rates/fractions in the 19 and especially 37 GHz channels. Most of the RMS error is a result of the bias, as opposed to random error, because the magnitude of the rms error is only slightly greater than that of the bias. Meanwhile, the 85 GHz rms error increases with rain rate and rain fraction, but the bias decreases with rain fraction suggesting that errors are more random. The non-zero biases at low rain fractions in all channels suggests an inability of the non-raining retrieval to match all T_b s simultaneously; [Elsaesser and Kummerow \(2008\)](#) provided evidence that this may be an indication of calibration error in addition to forward model bias.

Several researchers (*e.g.*, [Petty \(2001\)](#), [Greco and Anagnostou \(2002\)](#)) have noted that the 9 TMI brightness temperatures are not independent and can be reduced to, at most, 5 principle components

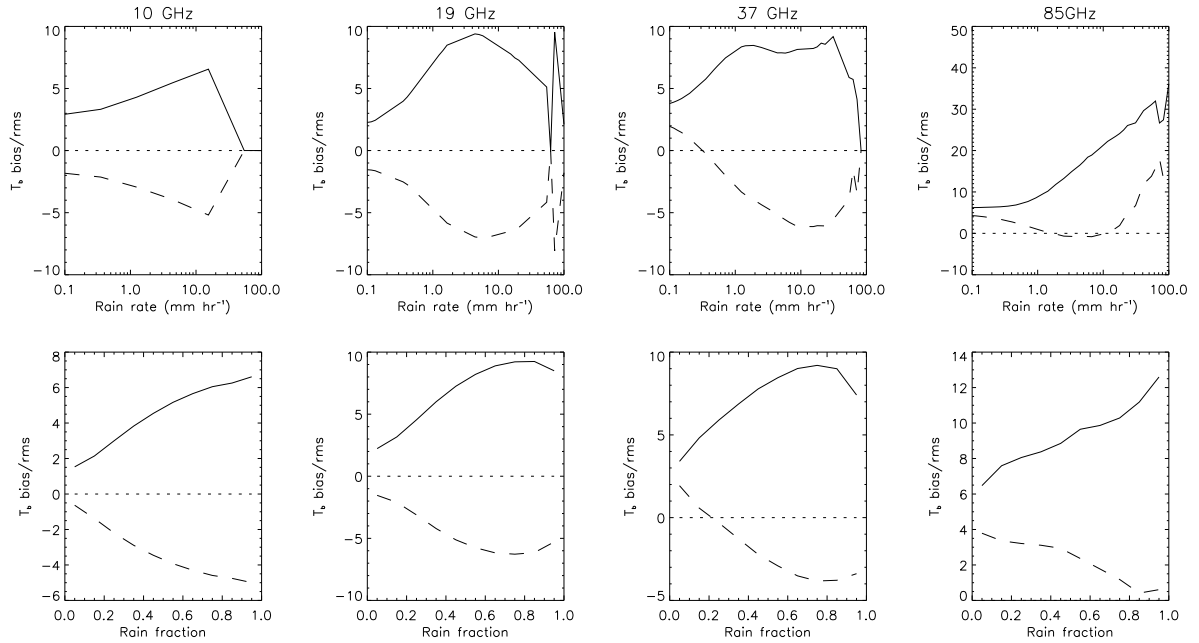


Figure B.1: Brightness temperature RMS (solid) and bias (dashed) as a function of rain rate and rain fraction in the TMI FOV for the vertically-polarized channels.

(PCs) in raining systems. An EOF analysis of the residual errors (Figure B.2) shows that the first two PCs explain 89% of the variability in the eight channels used in this retrieval. The first mode of variability is associated with a bias of the same sign in all channels, with the greatest magnitude in the 37 GHz channels. The second mode is associated with biases of opposite signs in the emission and scattering channels.

B.2 Residual Error Maps

The two leading EOFs of T_b error show that the bias in all channels can be simplified to the bias in the emission channels and the bias in the scattering channels. Thus, a quadrant analysis can be performed examining the percentage of time when these two sets of channels have warm or cold biases. These quadrants are shown in Figure B.3. The combination of emission and scattering channels biased warm is the most common pattern, particularly in the subsidence regions which lack deep convection. That these occur most frequently in the light rain regimes and are consistent with the low-rain rate and rain fraction errors in Figure B.1 suggests that errors in radiative transfer related to non-rain parameters or calibration error are the cause of this particular error pattern.

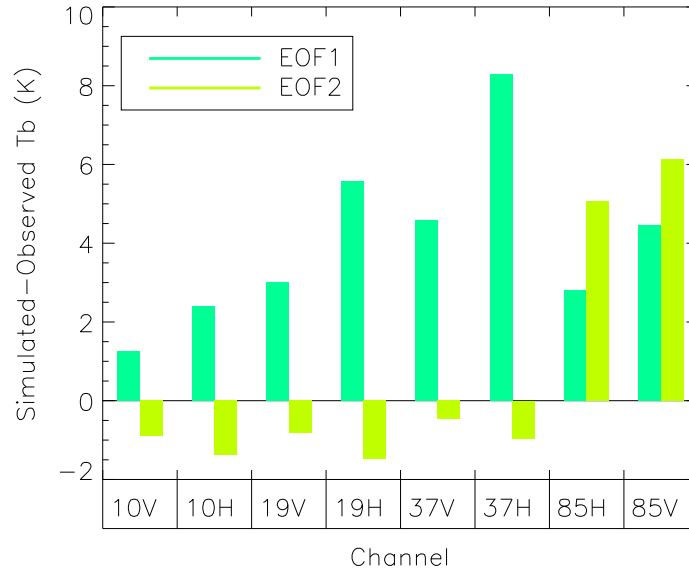


Figure B.2: The first two EOFs of residual T_b error.

The convergence zones have the highest occurrence of the cold bias in the emission channels with a warm bias in the scattering channels. This suggests that insufficient adjustments to the rain DSD and/or cloud water have been made here, even though rainfall increases have been made in these regions. Simultaneous cold bias in all channels occur most frequently in the extratropical regions, potentially indicating incorrect temperature profiles, a distinct possibility with the stronger temperature gradients in these regions. The combination of a warm bias in the emission channels with a cold bias in the scattering channels occurs rarely everywhere but slightly more frequently in the subsidence regions.

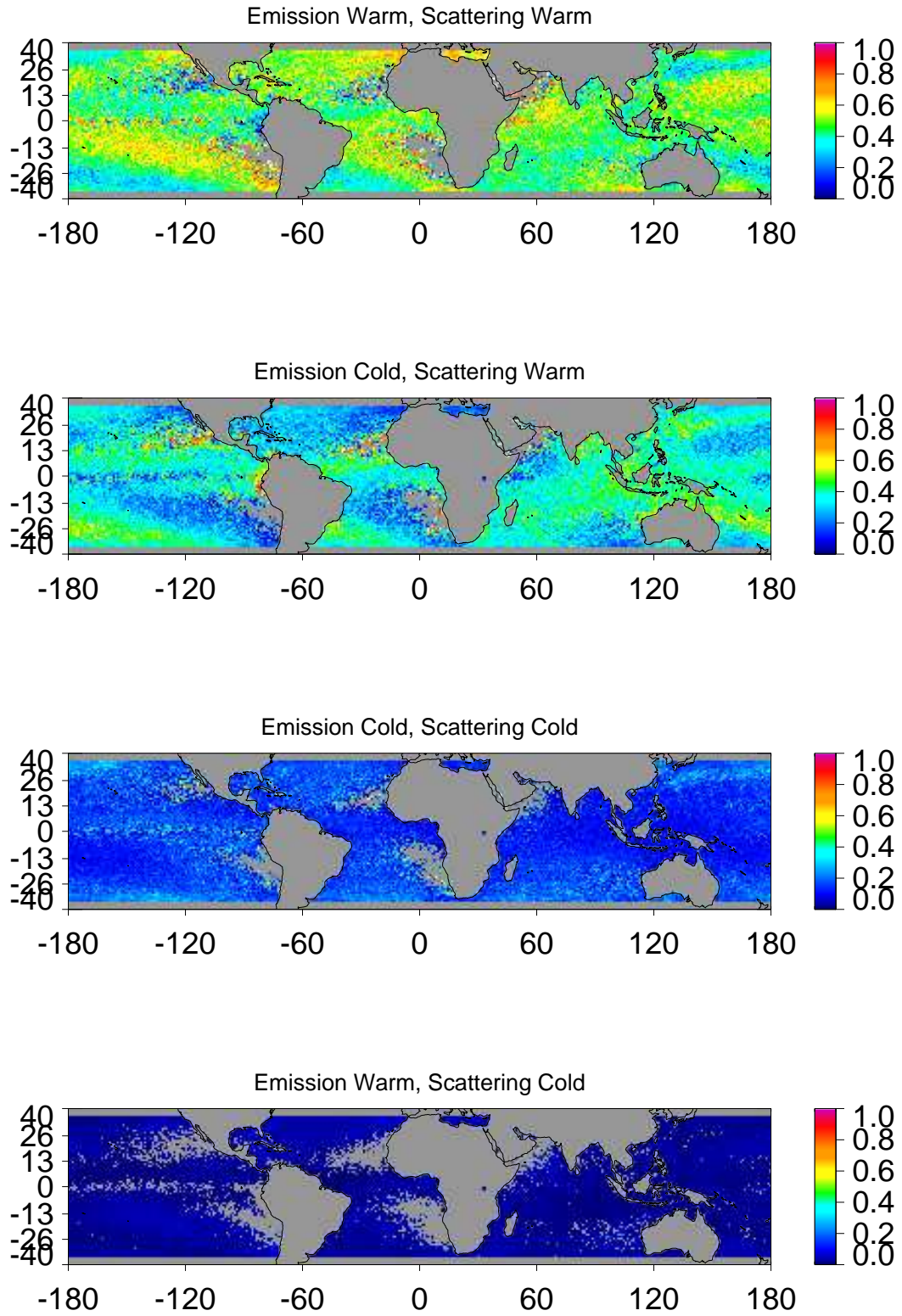


Figure B.3: Fractional distribution of T_b error by quadrant.

Appendix C

A BAYESIAN RADAR PROFILING ALGORITHM

A potential application of the correlations between reflectivity structure and the values of ϵ_{DSD} , ϵ_{ICE} , and ϵ_{CLW} noted in section 5.4 is a Bayesian profile-matching algorithm. This method has several advantages over the combined retrieval in that it is computationally faster and can be used over land. The disadvantage, of course, is that no radiometer or PIA information is explicitly included, and if the correlations of the retrieved parameters with reflectivity structure is weak, then little information has been added over the default DSD, ice, and cloud water assumptions. Additionally, since some types of precipitation, such as orographic events, will be undersampled or entirely missing from the ocean database, inaccurate values might be assigned in these precipitation types. This appendix will briefly describe a hybrid Bayesian method that uses the database of combined retrievals to set *a priori* values for ϵ_{DSD} , ϵ_{ICE} , and ϵ_{CLW} but still uses the SRT PIA to adjust the final value of ϵ_{DSD} if necessary. The algorithm formulation including a description of the database is given in section C.1. An analysis of one month of results, including comparisons to the full combined retrieval over ocean and comparisons with 2A25 over land, is given in section C.2.

C.1 Algorithm

This method utilizes a database of measured (1C21) reflectivity profiles and their associated values of ϵ_{DSD} , ϵ_{ICE} , and ϵ_{CLW} retrieved from the combined algorithm for the two years retrieved for the analysis in chapter 5 (1999-2000 and 2006). This database is broken down by echo top and freezing level in 250m bins for three reasons. First, the strength of the bright band is strongly related to the DSD as shown in chapter 5 and should be interpreted correctly. Second, echo top is also correlated with the

Table C.1: Effect of sample size on retrieved values of ϵ_{DSD} and rain rate for a sample orbit. Root-mean-square (RMS) and maximum differences along with overall bias relative to the full database are given.

Number of Profiles	100	1000	10000
RMS(ϵ_{DSD})	0.77	0.36	0.15
Max(ϵ_{DSD})	0.85	0.66	0.66
RMS(RR) [mm hr ⁻¹]	3.87	2.41	2.27
RR Bias	1.01	1.00	1.00

DSD and by only comparing profiles with the same echo top, the RMS error between the observed and database profiles can be calculated more directly without assigning some arbitrary penalty for missing echos in one profile. Finally, these subsets form smaller databases which improves computation time.

To obtain the *a priori* values for ϵ_{DSD} , ϵ_{ICE} , and ϵ_{CLW} for a sample profile from this database, each profile in the database is given a weight based upon the following formula:

$$W_i = \sum_{k=1}^N e^{-(Z_m(i,k)-Z_m(k))^2/(\sigma_Z^2)}, \quad (\text{C.1})$$

where N is the number of PR range gates with an echo, ($Z_m(i, k)$) represents the measured reflectivity in the k^{th} height level for the i^{th} database profile, $Z_m(k)$ is the measured reflectivity at the k^{th} height level for the sample profile, and σ_Z is set to 1 dBZ following [Masunaga and Kummerow \(2005\)](#). The weighted mean is then given by:

$$\epsilon = \frac{\sum_{n=1}^M W_i \epsilon_i}{\sum_{n=1}^M W_i}, \quad (\text{C.2})$$

where M is the number of profiles in the database.

For a given orbit, computation time scales with the number of profiles in the orbit times the number of profiles in the database. Even after subdividing by echo top and freezing height, there are several hundred thousand profiles in some of these bins and computation time becomes much slower than the full combined retrieval. In order to speed up the database matching component, reduction of the database size via random sampling is necessary. The effect of different sample sizes on the *a priori* values of ϵ_{DSD} , ϵ_{ICE} , and ϵ_{CLW} for a test orbit is given in [Table C.1](#). A database size of 1000 profiles was chosen as a compromise to maximize speed and minimize differences from the full database.

C.2 Results

One month not in the database (January 2001) was selected to compare results of the Bayesian-PR hybrid algorithm and the combined algorithm. Gridded mean values of ϵ_{DSD} , ϵ_{ICE} , and ϵ_{CLW} and their differences from the full combined algorithm for the central 25 PR rays over ocean are shown in Figure C.1. Squared correlation coefficients of these parameters with their counterparts from the combined algorithm are 0.19, 0.31, and 0.02, respectively. Therefore, a small but not insignificant amount of the DSD is directly related to the reflectivity profile. A greater amount of variation in the ice scattering properties is apparently contained in the reflectivity profile shape, which may be a result of preferred crystal morphologies in different reflectivity structures. The spatial patterns illustrate that biases relative to the combined algorithm are generally random¹ for ϵ_{DSD} and ϵ_{ICE} , but exhibit a strong positive bias in the subsidence regions for ϵ_{CLW} . This tendency is a direct consequence of the low correlation between the combined and Bayesian retrieval for this parameter. Lacking any information from the reflectivity profiles, the mean value is essentially applied which is biased high in these regions.

Finally, gridded rain rates from the hybrid retrieval are compared to the default DSD with no adjustment, the PIA-only retrieval without Bayesian modification of the *a priori* DSD, and 2A25 for the full PR swath over land and ocean in Figure C.2. As with the combined algorithm, the hybrid method increases rain rates over the tropical oceans and decreases them in the winter hemisphere mid-latitudes relative to 2A25. Over land, both positive and negative differences can be found without any clear preference. The next panel largely confirms the mostly random nature of the ϵ_{DSD} adjustments relative to the combined algorithm as these are present in the rain differences as well. Further comparisons to radar-only algorithms without any adjustment and without the Bayesian matching show generally similar trends indicating, as in the combined retrieval, that the inclusion of information from TMI (in this case implicitly from the radar profile database) makes adjustments in the same direction as the PIA but extending to those pixels without a reliable SRT PIA estimate.

¹ Some of this randomness may be related to database sampling issues.

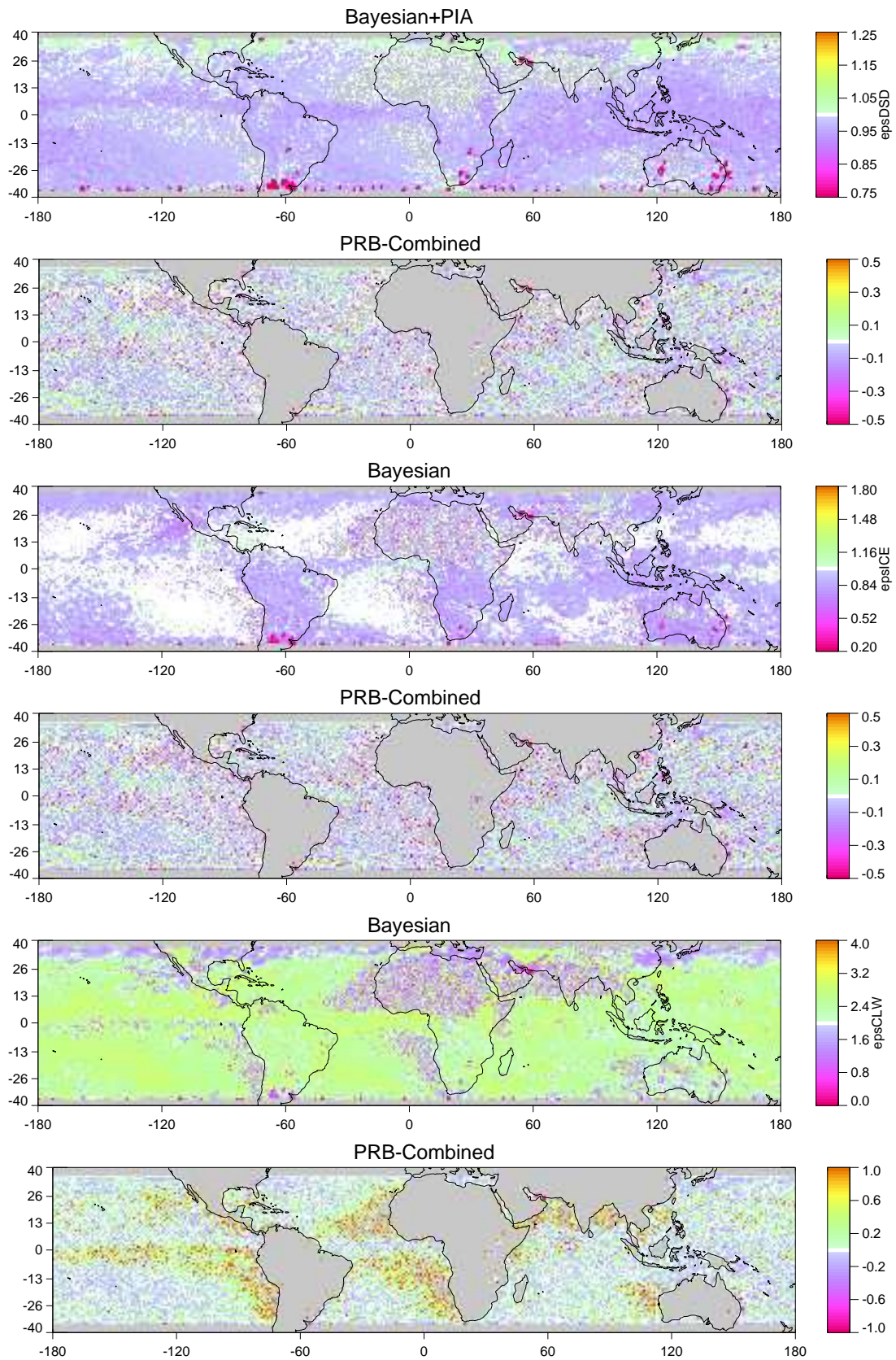


Figure C.1: Gridded mean values of ϵ_{DSD} , ϵ_{ICE} , and ϵ_{CLW} from the hybrid Bayesian+PIA (PRB) retrieval. Differences from the combined algorithm are also shown.

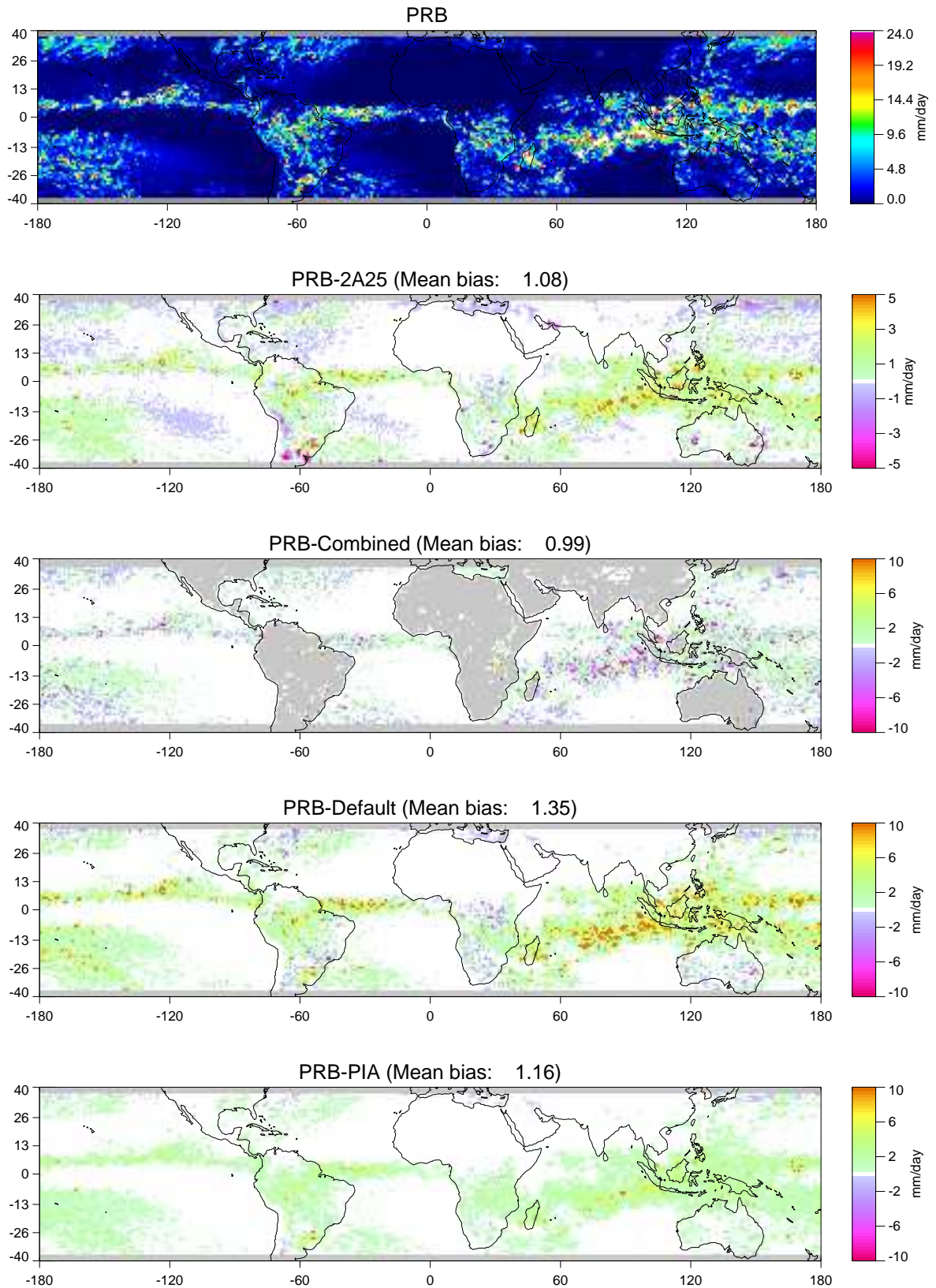


Figure C.2: Gridded mean rainrates from the hybrid Bayesian+PIA retrieval. Differences from other algorithms are also shown.